Stony Brook University

Reconstruction of Atmospheric [CO] and Stable CO Isotopes $\delta^{13}C$ and $\delta^{18}O$ Over the Last 250 Years

A Dissertation Presented

by

Alicia Mullaley

to

The Graduate School

in Partial Fulfillment of the

Requirements

for the Degree of

Doctor of Philosophy

in

Marine and Atmospheric Sciences

Stony Brook University

December 2016

Stony Brook University

The Graduate School

Alicia Mullaley

We, the dissertation committee for the above candidate for the

Doctor of Philosophy degree, hereby recommend

acceptance of this dissertation.

Dr. Daniel Knopf - Dissertation Advisor
Associate Professor, School of Marine and Atmospheric Science/
Institute for Terrestrial and Planetary Atmospheres

Dr. Sultan Hameed - Chairperson of Defense
Professor, School of Marine and Atmospheric Science/
Institute for Terrestrial and Planetary Atmospheres

Dr. David Black
Associate Professor, School of Marine and Atmospheric Science

Dr. Minghua Zhang
Professor, School of Marine and Atmospheric Science/
Institute for Terrestrial and Planetary Atmospheres

Dr. Xavier Faïn
Research Scientist
Laboratory of Glaciology and Environmental Geophysics Grenoble, France

This dissertation is accepted by the Graduate School

Charles Taber

Dean of the Graduate School

Abstract of the Dissertation

Reconstruction of Atmospheric [CO] and Stable CO Isotopes $\delta^{13}C$ and $\delta^{18}O$ Over the Last 250 Years

by

Alicia Mullaley

Doctor of Philosophy

in

Marine and Atmospheric Sciences

Stony Brook University

2016

Carbon monoxide (CO) is a trace gas that influences atmospheric chemical reactions. CO is relatively short-lived (weeks to months) in the atmosphere and therefore spatially variable with a modern concentration range from 35 parts per billion (ppb) to 150 ppb (Globalview-CO, 2009). Because of its lifetime, atmospheric carbon monoxide is a good tracer for hemispheric processes; it is long enough to be transported over hemispheric distances but is short enough where there can be large seasonal and interannual variations. Therefore, measuring the variations in CO from bubbles trapped in Antarctic ice can reveal processes that occur in the Southern Hemisphere (SH).

CO is the principal sink for the hydroxyl radical (OH) which is the most important oxidant in the atmosphere. The abundance of atmospheric OH can impact the lifetime of various atmospheric constituents such as the greenhouse gas methane (CH_4), hydrofluorocarbons (HCFCs), non-methane hydrocarbons (NMHCs) and tropospheric ozone. In particular, because CO is the main loss mechanism for OH, increased concentrations of CO can cause a build-up of methane therefore affecting the global radiative budget and thus Earth's climate. Once CO concentration is determined, the isotopes of CO provide valuable information on the source of CO. These new data will better constrain the sources and sinks of CO and thus its global cycle, helping to resolve uncertainties in climate models by providing additional constraints.

Here I present a detailed investigation to determine atmospheric [CO] and stable CO isotopes ^{13}CO and $C^{18}O$ from 1950 -1700 AD as recorded in bubbles trapped in ice cores from West Antarctic Ice Sheet Divide (WAIS D), Antarctica. This study better constrains the sources of atmospheric CO in the Southern

Hemisphere during the late Holocene, including the contribution from biomass burning. The relationship between CO and CH_4 over this time period is constructed based on these new observations and previously published CH_4 paleo data. Overall, the results obtained from this study improve our understanding of the temporally varying sources of CO and the overall stability of tropospheric chemistry with respect to the CH_4-CO-OH cycle.

Dedication Page

For my parents, who always taught me the value of believing in yourself.

Contents

List of Figures

List of Tables

Acknowledgments

I would just like to thank my advisor and friend Daniel Knopf. Your passion and strong work ethic are inspirational. Your dedication to education and research have been instrumental in preparing me for my future. Under your guidance I was able to develop the skills necessary to succeed in my chosen profession and I will forever be grateful.

I am grateful for my collaborator and committee member Xavier Faïn. Thank you for welcoming me to your lab in Grenoble, France. It was especially nice when you would visit Stony Brook and we could troubleshoot the line, I always learned something new during our time together.

I also wish to thank the other members of my committee including David Black, Sultan Hameed and Minghua Zhang for their encouragement, support and helpful comments along the way.

I want to especially thank the members of the Mak and Knopf groups including Luping Su, Alex Scida, Tracey Evans, Kim Gromov, Peter Alpert, Seanna Forrester and Nate Slade. I have really enjoyed working in your company over the years.

Most importantly I would like to thank my family. Without their support and love this work would not have been possible. To my daughter Harper, between writing this dissertation, starting a new faculty position and growing a tiny human, I have been an absentee mother but thank you for being patient with me. Luckily you have an incredible father who filled in for me while I was preoccupied. Lastly, to my husband, thank you for not only supporting all of this but encouraging me to pursue whatever it is that makes me happy in all capacities of life. You are an incredible man, someone I admire, and I am so happy I get to share my life with you. Now let's go for a *walk in the woods.*

Chapter 1

Reconstruction of Atmospheric [CO] and Stable CO Isotopes $\delta^{13}C$ and $\delta^{18}O$ Over the Last 250 Years

August 27, 2016

1 Introduction

Carbon monoxide (CO) is a trace gas that influences chemical reactions in the atmosphere. CO is relatively short-lived (weeks to months) in the atmosphere and therefore spatially variable with a modern concentration range from 35 parts per billion (ppbv) to 150 ppbv (Globalview-CO, 2009). Because of its lifetime, atmospheric carbon monoxide is a good tracer for hemispheric processes; it is long enough to be transported over hemispheric distances but is short enough where there can be large seasonal and interannual variations. Therefore, measuring the variations in CO from bubbles trapped in Antarctic ice can reveal processes that occur in the Southern Hemisphere (SH) since Antarctic ice is a past archive of the composition of the atmosphere.

CO is the principal sink for the hydroxyl radical (OH) which is the most important oxidant in the atmosphere. The abundance of atmospheric OH can impact the lifetime of various atmospheric constituents such as the greenhouse gas methane (CH_4), hydrofluorocarbons (HCFCs), non-methane hydrocarbons (NMHCs) and

tropospheric ozone. In particular, because CO is the main loss mechanism for OH, increased concentrations of CO can cause a build-up of methane therefore affecting the global radiative budget and thus Earth's climate. Once CO concentration is determined, the isotopes of CO provide valuable information on the source of CO. Currently the CO isotope and concentration record only extends back 650 years and there is a gap in the record from 1900-1950. Extending the CO record back through the late Holocene will better constrain the sources and sinks of CO and thus its global cycle, helping to resolve uncertainties in climate models by providing additional constraints.

There are many sources of CO including methane oxidation, biomass burning, fossil fuel and biofuel burning, oxidation of non-methane hydrocarbons (NMHC) and direct emission from the ocean. Variations in CO sources as well as atmospheric chemical processes can have an impact on the CO budget and evaluating these variations are useful in characterizing and quantifying chemistry-climate interactions. More specifically, reconstructing variations in biomass burning (a major source of CO) is of interest because biomass burning plays a key role within the earth-atmosphere system. Climate impacts the biomass burning pattern since biomass burning is a function of fuel load, precipitation and humidity, and temperature (e.g., Westerling et al., 2006; Kitzberger et al., 2007;Swetnam, 1993). The correlation between burning and climatic variations such as temperature and precipitation has been reported (Kitzberger et al., 2001 & Power et al., 2008).

Likewise, biomass burning can impact climate, notably through emission of gaseous species to the atmosphere and can impact the oxidation state of the atmosphere. Furthermore, these processes can have net direct radiative forcing effects (e.g. emissions of CO_2 and black carbon from biomass burning) or impact chemistry-climate interactions by the emission of large amounts of reactive gas such as CO. Increased emission of reactive gas will impact the oxidation state of the atmosphere and thus impact the lifetimes of other gases such as methane (Andreae and Merlet, 2001).

Here I present a detailed investigation to determine atmospheric [CO] and stable CO isotopes ^{13}CO and $C^{18}O$ from 1700 to 1950 AD as recorded in bubbles trapped in ice cores from the West Antarctic Ice Sheet Divide (WAIS D), in Antarctic. This study better constrains the sources of atmospheric CO in the Southern Hemisphere during the late Holocene, including the contribution from biomass burning. The relationship between CO and CH_4 over this time period is constructed based on these new observations and previously published CH_4 paleo data. Overall, the results obtained from this study improve our understanding of the temporally varying sources of CO and the overall stability of tropospheric chemistry with respect to the CH_4-CO-OH cycle.

1.1 Modern carbon monoxide measurements

Carbon monoxide is a reactive trace gas with a modern concentration of ~50 ppbv in the remote Southern Hemisphere but the seasonality is ~35-65 ppbv. At present, a large gradient of ~100 ppbv exists from the Northern Hemisphere (NH) to SH because of the high rate of anthropogenic emissions in the NH (figure1.2). For example, currently, high CO emissions result from cars, factories and fires in the NH. Elevated levels of CO are known to adversely affect the natural cleansing ability of the atmosphere by reducing its ability to destroy other harmful pollutants because CO is the primary sink for OH. Generally speaking, the higher the concentration of CO, the lower the concentration of OH and the ability for OH to react with other gaseous species. Thus, accurate measurements of CO are needed. Monitoring CO emissions in modern times is carried out by a few methods including remote sensing via satellites and by ground based measurements through the National Oceanic and Atmospheric Administration (NOAA) Earth System Research Laboratory / Global Monitoring Division (ESRL/GMD) which monitors trace gases from 49 sites globally.

1.1.1 Ground based measurements

The most extensive modern record of CO comes from the ground based NOAA's Earth System Research Laboratory / Global Monitoring Division (ESRL/GMD) which monitors trace gases from 49 sites globally (figures 1.1, 1.4 & 1.6). The first

direct measurements by ESRL/GMD of CO in the SH were made in 1988 (e.g., at the American Samoa Observatory, SMO, located in the middle of the South Pacific, about midway between Hawaii and New Zealand at 14.2° S latitude). In the Northern Hemisphere flaks measurements started in December 1988 at the Niwot Ridge, Colorado station (figure 1.1). Figure 1.1 is the CO concentration in 10^{-9} mol CO per mol of dry air (nmol mol^{-1}) from surface flasks from Niwot Ridge, Colorado. Circles (blue) are regionally representative of a remote, well-mixed troposphere. + symbols are not indicative of background conditions, and represent poorly mixed air masses influenced by local or regional anthropogenic sources or strong local biospheric sources or sinks. The grey line represents a smooth curve and long-term trend. Data shown in orange are preliminary and have not yet been subjected to rigorous quality assurance procedures as per NOAA standards and includes critical evaluation procedures to ensure the standard reference gases used in making the measurements in Boulder and in the field are well characterized (i.e., calibrated before and after their use); samples compromised during collection or analysis are identified, and valid samples not representative of typical background conditions are identified. Continuous recording at the South Pole (SPO) commenced a year later in 1989 and at Mauna Loa Observatory (MLO) in 1992 (Novelli et al., 1998; Novelli et al., 1994). There is however data from flask measurements by the Oregon Graduate Institute (OGI) that extends back to 1979 but it is sparse (Khalil and Rasmussen, 1984; Khalil and Rasmussen, 1988; Khalil

and Rasmussen, 1994). It should be noted that in 1950 - 1951 at the Jungfrau Joch Scientific Station in the Swiss Alpines CO concentration was reported for the first time by deriving the mixing ratio from ground-based infrared solar spectra (Rinsland and Levine, 1985).

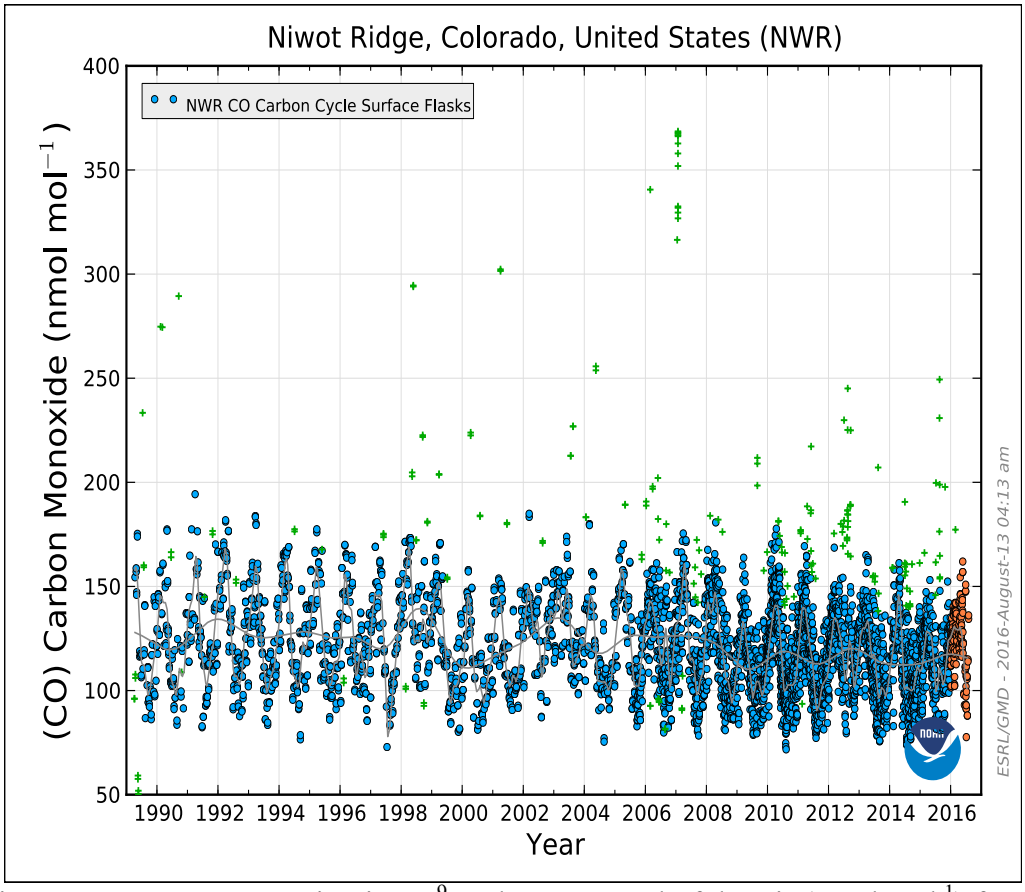

Figure 1.1: CO concentration in 10^{-9} mol CO per mol of dry air (nmol mol^{-1}) from surface flasks from Niwot Ridge, Colorado. Circles (blue) are regionally representative of a remote, well-mixed troposphere. Data from NOAA ESRL/GMD, uncertainty ± 1ppbv.

1.1.2. Remoting sensing measurements

In addition to ground-based measurements of CO, there are several remote sensing measurements as well. The first satellite measurements of CO came in the early 1980's by Measurement of Air Pollution from Satellites (MAPS). The MAPS instrument measured CO in the lower atmosphere from 3-10 km above the surface latitude 57 degrees North to latitude 57 degrees South and measurements ceased in the late 1990's. A satellite currently making measurements of tropospheric CO is on board of NASA's Earth Observing System Terra spacecraft and is called Measurements Of Pollution In The Troposphere (MOPITT). MOPITT makes global measurements every three days with a spatial resolution of 22 km at nadir and it scans the Earth in bands that are 640 km wide. MOPITT is a helpful instrument to track the sources, sinks, transport and distribution of global CO. However, the dataset only extends back to 2000 AD (figure 1.2).

Another sensor making column measurements of CO is The Atmospheric Infrared Sounder (AIRS), which is an instrument launched in to orbit on board of NASA's Aqua satellite in 2002 whose mission is to support climate research and improving weather forecasting. AIRS provides a daily global view of the three-dimensional physical state of the atmosphere (clouds, water vapor, air temperature) and the distribution of certain trace gases (ozone, carbon monoxide, carbon dioxide and methane). AIRS provides daily global carbon monoxide maps over approximately 90% of the Earth with its 1600 km cross-track swath and cloud-

clearing retrieval capabilities. Since 2004, CO is also monitored remotely by the Tropospheric Emission Spectrometer (TES) which is on board of NASA's polar orbiting Aura satellite. In addition to CO, TES gives vertically resolved mixing ratios for ozone, methane and water vapor in the troposphere. The last satellite providing a CO data set is SCanning Imaging Absorption spectroMeter for **A**tmospheric CHartograph**y** (SCIAMACHY). SCIAMACHY was launched on board ENVISAT (Environmental Satellite) which was operational from March 2002 to April 2012 and whose primary objective was the global measurement of various trace gases in the troposphere and stratosphere. CO data from SCIAMACHY is available from 2003-2007 AD.

Data from MAPS, MOPITT, AIRS, TES and SCIAMACHY represent the complete collection of satellite data available for CO concentration measurements. It should be noted that while satellite data for CO can be useful it is not without limitations (Duncan et al., 2014 and Deeter et al., 2012). For example, satellites don't measure CO directly, but rather infers concentration based on measuring infrared wavelengths of light, among other methods (Duncan et al., 2014). Figure 1.2 shows a MOPITT composite of the globally averaged CO concentration for the first year (2000) of complete data and the globally averaged CO concentration for 2014. Although, satellites cannot measure ground-based CO, which is where most of CO is located, satellite data can be useful for tracking long-range transport of CO plumes from biomass burning events (Deeter et al., 2012). Overall, the in-situ

measurements from NOAA ESRL/GMD combined with satellite data give a good overview of current CO concentrations (figure 1.1 and figure 1.2). However, to derive CO from time periods before the modern instrumental era paleoclimatological data such as ice cores are better suited because ice can reveal a record thousands of years old.

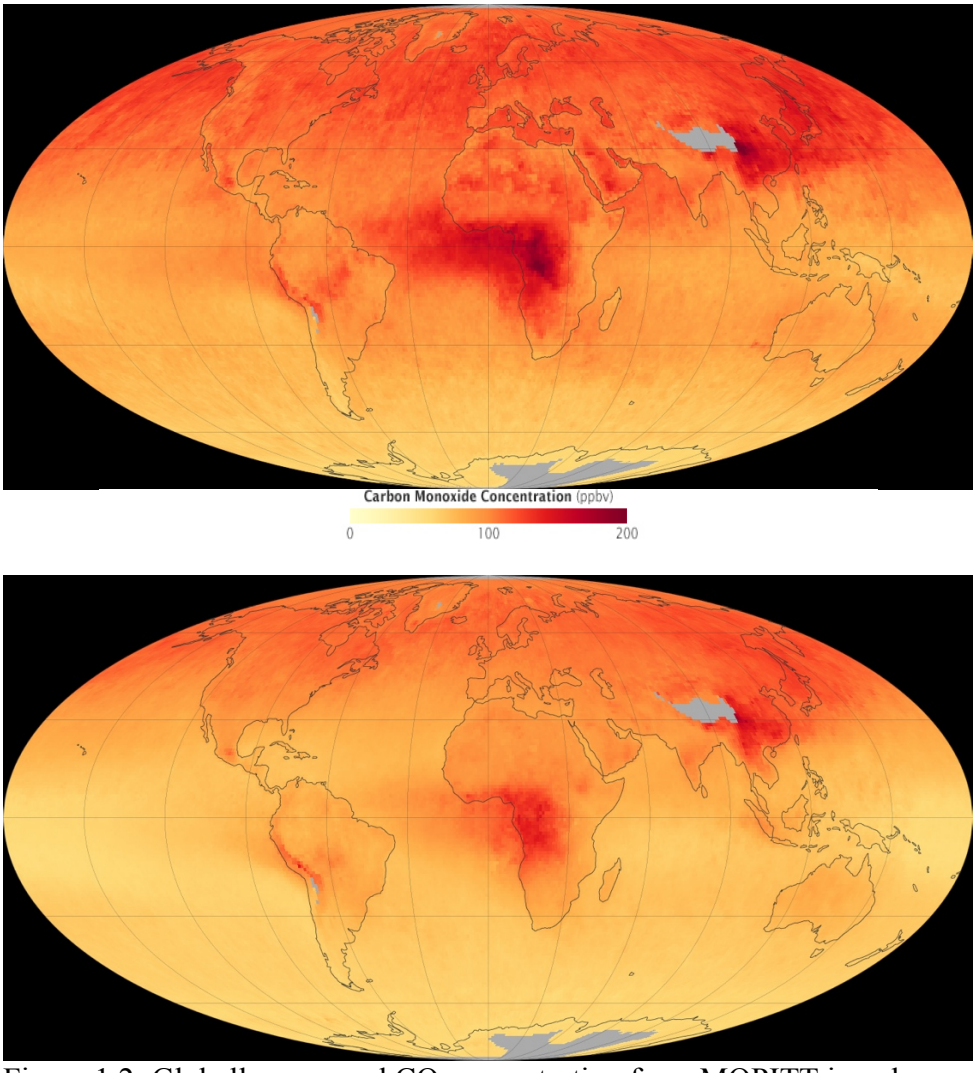

Figure 1.2: Globally averaged CO concentration from MOPITT in ppbv over the year from 2000 (top panel) and 2014 (bottom panel).

1.2 Trace gases in ice cores: proxies of earth's climate history

Air trapped in polar ice gives an archive of paleo environmental conditions by recording the variability of past atmospheric composition. Polar ice cores are an invaluable tool for understanding how earth's climate changed over time because they can represent a continuous record. For some cores, this record extends back hundreds of thousands of years and analyses of air trapped in ice has given a record of important past greenhouse gases such as CO_2, CH_4 and N_2O.

The first person to conceive the idea of using ice cores to study past climate was the Danish scientist, Willi Dansgaard in the 1950's. Ice cores from Greenland have been helpful in providing a high-resolution 123,000 year record of climate variability and an understanding of abrupt climate change (e.g. NGRIP Project Members 2004; Alley et al. 2009; Severinghaus and Brook 1999). On the other hand, cores from the persistently cold, isolated and remote Antarctic ice sheet give data from the past eight glacial cycles since the Mid-Pleistocene Climate Transition, ~800,000 years before present (EPICA Community Members 2004). A record of this length allows for the investigation of the range of natural variability of climate as well as provide insights into a variety of climate forcing mechanisms which can be helpful to test global and regional climate models. Reconstruction of CO_2 and CH_4 from the EPICA core revealed that their concentrations ranged from ~170 to 300 ppmv and ~350 to ~800 ppbv, respectively (Loulergue et al., 2008;

Luthi et al., 2008; Siegenthaler et al., 2005; Spahni et al., 2005).

One of the more recent ice coring projects in Antarctica is the West Antarctic Ice Sheet Divide ice core (WAIS Divide, 79.5 S, 112 W, 1,766 m above sea level), which is where the samples used in this study originate from. The WAIS Divide ice core was drilled to a length of 3,400 m in 2013 and provided the first Southern Hemisphere record of greenhouse gas and climate with comparable time resolution and duration to the Greenland ice cores. This is important because it enables detailed inter-hemispheric comparison of environmental conditions. Other Antarctic coring efforts include Vostok which revealed a 420,000 year record of CO_2 and CH_4 that correlates with the temperature record (Petit et al., 1999). Another study that aimed to provide high resolution records from Antarctica is Law Dome. The ice from Law Dome, Antarctica provides a high resolution (decadal changes) record of the important greenhouse gases CO_2, CH_4 and N_2O. It was observed that there was a major increase in CO_2, CH_4 and N_2O concentrations during the past 200 years which was preceded by a period of relative stability (MacFarling-Meure et al., 2007). During the industrial period, decadal variations reveal the stabilization of CO_2 and slowing of CH_4 and N_2O growth in the 1940s and 1950s. The variations in concentration throughout the preindustrial period for these species is ~10 ppm, 40 ppbv and 10 ppbv, respectively (MacFarling-Meure et al., 2007).

Besides greenhouse gases, Antarctic ice has provided a history of other

species including carbonyl sulfide (COS) and methyl chloride (CH_3Cl) for example. COS is the most abundant sulfur gas in the atmosphere, a precursor for stratospheric sulfate, and a promising tracer for gross primary productivity (Montzka et al., 2007). A recent record of COS from WAIS D spanning the last 54,300 years before present indicates that atmospheric COS was 250–300 parts per trillion (ppt) during the last glacial maximum (LGM) and declined by 80–100 ppt during the last glacial/interglacial transition to a minimum of 160–210 ppt at the beginning of the Holocene (Aydin et al., 2016). The authors conclude that this decline was likely caused by an increase in the gross primary productivity of terrestrial plants, with a possible contribution from a reduction in ocean sources. Atmospheric COS levels were above 300 ppt in the late Holocene and then rose to ~500 ppt in the late 20^{th} century, indicating that large changes in the COS biogeochemical cycle occurred during the Holocene (Aydin et al., 2008, Aydin et al., 2016). It should be noted that COS hydrolyzes in ice core air bubbles, and the recovery of an atmospheric record requires correcting for this loss (Aydin et al., 2008). Methyl chloride (CH_3Cl) is a naturally occurring ozone-depleting gas that is the largest natural source of chlorine to the stratosphere and the most abundant halocarbon in the troposphere, with a global average mixing ratio of 550 ± 30 ppt (Montzka et al., 2003). Measurements in air extracted from a 300 m ice core from South Pole, Antarctica, covering the time period from 160 BC to 1860 AD show that CH_3Cl levels were elevated from 900-1300 AD by about 50 ppt relative

to the previous 1000 years, which coincides with the Medieval Warm Period (MWP). Meanwhile, CH_3Cl levels decreased to a minimum during 1650 - 1800 AD correlating with the period of the Little Ice Age (LIA) (Williams et al., 2007). One can see how polar ice cores are excellent archives of past environmental conditions and provide us with glimpses into the Earth's climatic history over hundreds of thousands of years.

While there are many studies on trace gases in ice, most focus on greenhouse gases while little is known about CO. The reason for this is measuring CO in ice presents experimental challenges such as limitation of sample size (Wang and Mak, 2010) and contamination due to in situ production, especially in the Northern Hemisphere (Haan et al., 2001; Fain et al., 2014). The difficulty in measuring CO from Northern Hemisphere ice arises from in-situ production of organic matter (e.g. Euro core from Greenland). This study focuses on a Sothern Hemisphere Antarctic location as the opportunity for contamination from organics is low (Wang et al., 2010).

1.2.1 CO measurements in ice and firn

In order to investigate CO before modern time (i.e. before NOAA monitoring and satellite observation) you must either extract CO from ice cores or firn. Firn is the top layer of an ice sheet whose composition is compacted snow with interconnected

pore space (details in Chapter 2). Several ice core and firn studies on CO have been conducted in the Southern Hemisphere, specifically in Antarctica (Haan et al., 1996, Haan and Raynaud, 1998; Macfarling Meure, 2004; Ferretti et al., 2005; Assonov et al., 2007; Wang et al., 2010; figure 1.3). Wang et al. (2010) demonstrated the ability to use CO concentration coupled with isotope data to investigate the variability of the past sources of CO. In this study, it was discovered that CO concentrations decreased by ~25% (14 ppbv) from the mid-1300s to the 1600s (occurring during the Little Ice Age cooling period), then recovered completely by the late 1800s (figure 1.3). Meanwhile, $\delta^{13}C$ and $\delta^{18}O$ of CO decreased by about 2‰ and 4‰, respectively, from mid-1300s to the 1600s, then increase by about 2.5‰ and 4‰ by the late 1800s due to unexpected variations in biomass burning over the last 650 years. Haan et al. (1996) reconstructed CO concentration (8 samples) from the D47 ice core (Antarctica) for the time period from 1860–1920 AD. CO levels at this high latitude location exhibited little variation with an average of CO concentration of 57 ±2 ppbv. Haan and Raynaud (1998) report on 9 samples that were taken from the Vostok, Antarctica BH3 and BH5 ice cores and conclude that Southern Hemisphere CO increased slightly between 250 BC and 1900 AD from about 50 to 57 ppbv. In contrast, a study by Ferretti et al. (2005) showed that CO concentration from bubbles trapped an ice core from Law Dome, Antarctica decreased over a similar time period. Samples covering 0 to 1700 AD demonstrated that CO in the Southern Hemisphere

decreased from ~ 70 ppbv around 1400s to ~ 50 ppbv in ~ 1700 AD, with the analytical uncertainty being 13.2 ppbv. The authors concluded that a decrease of biomass burning associated with a decline in the population of Central and South America potentially due to contact with Europeans. This is consistent with the Wang et al. (2010) work.

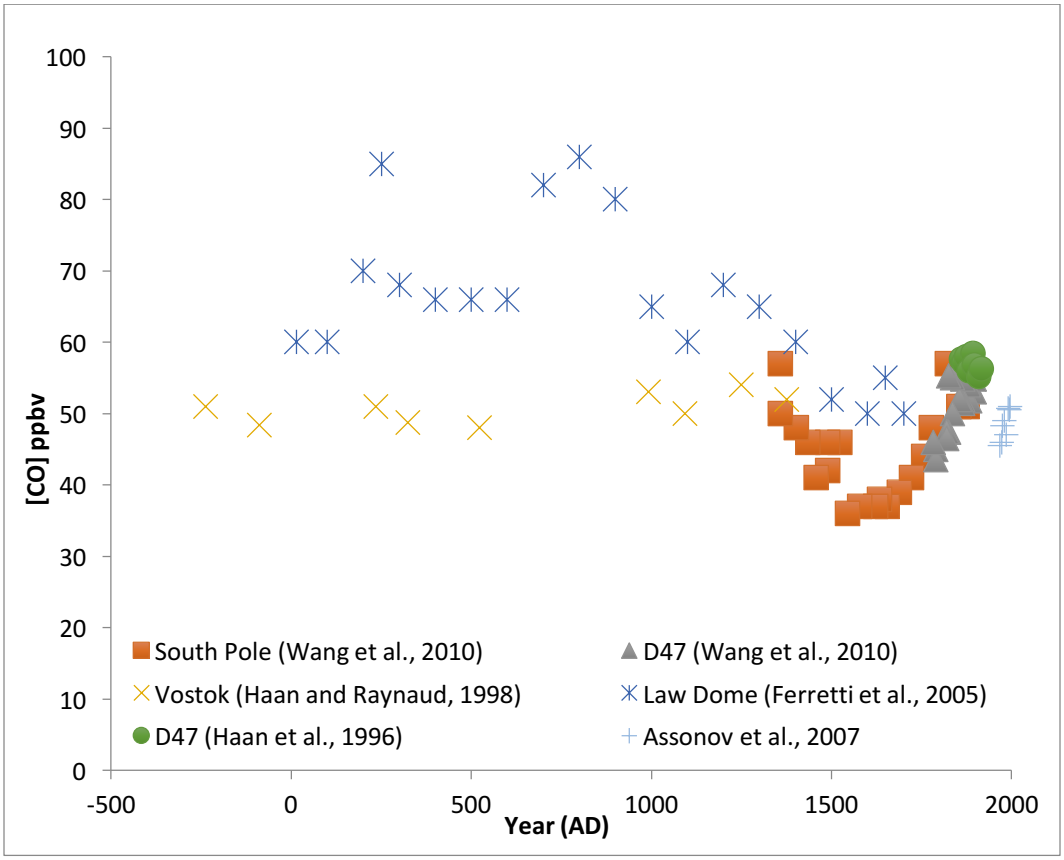

Figure 1.3: CO concentration as measured in Antarctic ice cores and firn.

Assonov et al. (2007) measured CO in firn from the three Antarctic sites Dronning Maud Land (DML), Dome Concordia (Dome C) and Berkner Island, but only the samples from Berkner Island gave usable results (figure 1.3). The authors speculate that the results from DML and Dome C (Assonov et al. 2007) exhibited contamination from CO production due to their high pressure compressor. More specifically, at DML, warming of the compressor was not controlled. At Dome C, due to low ambient pressure (elevation 3233 m) the authors had difficulties filling the cylinders near the close-off-depth. They also report allowing the compressor to warm up and run for a prolonged time which they report increases contamination. This explains the high CO measured at Dome C near the close off and thus only samples from Berkner Island are considered. The Berkner Island results (Assonov et al. 2007) suggest that CO increased by ~38 %, from 38 ±7 to 52.5 ±1.5 parts per billion by volume (ppbv) over a period of roughly 100 years (~1900-2000 AD). The $\delta^{13}C(CO)$ data obtained for Berkner Island suggest that CO was isotopically heavier in the past in agreement with a lower contribution of methane.

There have also been studies done on CO from firn and ice from the Northern Hemisphere. In particular, CO in firn was measured in the North Greenland Eemian drilling site (NEEM) as well as Summit, the North Greenland Ice Core Project (NGRIP) (Petrenko et al., 2013). The Greenland firn produced a 60 year record (from 1950 AD) of atmospheric CO and showed concentration was

highest during the late 1970's. CO isotopic analysis from NEEM revealed a maximum of ~155 ppbv was likely due to changing CO emissions from fossil fuel combustion (Wang et al., 2012). More specifically, $\delta^{13}C$ remained constant at -26.5‰ from 1950 to 1970, increased by ~1.2‰ from 1970 to the mid-1990s, and decreased by ~2‰ from the mid-1990s to present day. $\delta^{18}O$ was 9‰ in 1950, increased by 1‰ by 1980 and then decreased by 3‰ by present day. An isotope mass balance model was applied to quantify the temporal evolution of CO source partitioning. The mass balance model results show that a reduction in CO derived from fossil fuel combustion is the likeliest mechanism behind these trends. The mitigation policy for CO emission from vehicle exhaust such as application of catalytic converters and the growth of diesel engine vehicles market share is the likeliest reason for the CO source strength change from fossil fuel combustion (Wang et al., 2012). The only studies that extend the record farther back in time include the pioneering work by Haan et al. (1996) and Haan and Raynaud (1998) on the Eurocore and the more recent work of Fain et al. (2014) on NEEM extending the record to 1800 years before present (BP). The work by Haan et al. (1996) and Haan and Raynaud (1998) showed that CO increased from ~90 ppbv to ~110 ppbv from 1850 – 1950 AD while CO concentration from 1625 to 1850 AD shows little variation and is stable at ~90 ppbv. However, samples from the Eurocore that date back to ~1600 AD (depths >167 m) show increased variability and high CO levels (100-180 ppbv), presumably due to in situ CO production

(Haan et al., 1996 and Haan and Raynaud 1998). Fain et al. (2014) observed similar effects in samples form NEEM with regard to a highly variable mixing ratio (75 to 1327 ppbv) because of in situ CO production due to the presence of organic material.

Currently there is no CO concentration and isotope record in the Southern Hemisphere from 1900-1950 and no record from West Antarctic Ice Sheet Divide (WAIS Divide) exists. Filling in the CO record from 1900-1950 will better constrain the sources and sinks of CO and thus its global cycle helping to resolve uncertainties in climate models by providing additional constraints.

1.3 Modeled global CO budget

The relative contribution of CO from its sources has changed throughout time. For example, before the industrial revolution there was little to no contribution from fossil fuel burning. During the mid 1800s and moving forward, fossil fuel and biofuel burning became a dominant source of CO to the overall budget. The current estimate of CO loading to the atmosphere is 2600-3100 Tg CO yr^{-1} (Duncan et al., 2007; Park et al., 2015; IPPC 2001 and Bergamaschi et al., 2000) There is a range in CO loading because the estimates come from difference sources (e.g., satellite observation, flask measurements, model results) and different applied time scales or different time periods covered in the data sets. Estimates of the global tropospheric CO are given in Table 1.1. and are based on

inversion modeling. The inverse modeling technique estimates the source strength of atmospheric constituents by constraining a priori source inventories using observational data of chemical species and an atmospheric chemical transport model (TM). More specifically, data was obtained by the TM2 model (TM2 is a global 3-D model of the atmospheric transport of passive tracers). The model was constrained with data from NOAA's Global Monitoring Division (GMD) from 1993-1995. This time period was chosen because the CO mixing ratio trends and interannual variations are small relative to the years prior. CO mixing ratios were taken from 33 sites in the NOAA Climate Monitoring and Diagnostics Laboratory (CMDL) network (Novelli et al., 1988).

Table 1.1: Sources and Sinks of CO

Sources	
Fossil Fuel and Biofuel Burning	642
Anthropogenic HC* oxidation	166
Biomass Burning	722
Oxidation of Biogenic HCs	507
Ocean	23
CH_4 Oxidation	830
Sum	2890
Sinks	
OH Oxidation	2596
CO Deposition	294

Estimates of global sources of CO as derived from inversion analyses. Units in Tg CO/yr.*Hydrocarbon (HC); CO sources are from Bergamaschi et al. (2000).

The sources of CO are shown in Table 1.1 and include methane oxidation, biomass burning, fossil fuel and biofuel burning, oxidation of non-methane hydrocarbons (NMHC) and direct emission from the ocean. The main sink for CO is OH oxidation (~90%) and small amount of uptake by soils. NMHC can come from biogenic and anthropogenic sources. Common biogenic emissions include isoprene, monoterpenes, methanol and acetone (Bergamaschi et al. 2000). Various sources of CO dominate at different latitudes. For example, in the tropics the oxidation of methane and biogenic NMHC as well as biomass burning is the dominant source while at northern hemisphere mid-latitudes, fossil fuel combustion is the dominant source (e.g., Logan et al., 1981; Holloway et al., 2000).

While the major sources of CO are known, the global budget of CO cannot be easily derived (Bergamaschi et al., 2000; Duncan et al., 2007; Park et al., 2015). A large amount of uncertainty exists with the major sources because of their complex distribution as well temporal variations and short lifetimes associated with its chemical precursors (Brenninkmeijer et al., 1997, 1999). For example, most uncertainty comes from NMHC oxidation of isoprene and terpenes (Duncan et al., 2007). Another area of uncertainty in the CO budget is the direct emissions of CO from the ocean and plants. CO is mainly produced by the photochemical oxidation of dissolved organic matter as well as plants and degrading plant matter from the photodegradation or photooxidation of cellular

material (Tarr et al., 1995; Conrad et al., 1982 and Stubbins et al., 2006). These sources are small however (<10%) and are roughly balanced by loss via soil consumption (IPCC-SAR, 1996; Sanhueza et al., 1998). The major sink for CO is reaction with the hydroxyl radical. This reaction is responsible for ~90% of CO removal from the troposphere, as shown in Table 1.1 (Bergamaschi et al., 2000; Duncan et al., 2007; Park et al., 2015).

It is important to reconstruct an accurate record of CO that extends beyond the instrumentation period. For example, estimates of sources and sinks of CO are leading to emissions inventories that are being used in climate model simulations (e.g., in atmospheric chemistry models) for the IPCC 5th Assessment Report AR5 (Lamarque et al., 2010). It is therefore necessary to construct an accurate record of past CO concentration so models that require this information will be better constrained. Specifically, CO is used in climate models to help understand the fate of other reactive species and estimate the contribution of indirect forcing of CO. Most notably CO effects OH which can change the lifetime of methane, an important greenhouse gas. Also, CO can lead to the production of ozone, dependent on if NO_x is present (figure 1.4). CO's effect on ozone along with methane is difficult to quantify so a 3D chemical model is needed. Figure 1.4 demonstrates ozone formation as the result of carbon monoxide oxidation in the presence of nitrogen oxides (NO_x = NO and NO_2). The burning of biomass and fossil fuels release CO, NO_x and hydrocarbons into the troposphere. The

hydrocarbons can then be oxidized in the presence of high NO_x to form ozone (figure 1.4). The threshold for separating high NO_x from clean or low NO_x is ~100 parts per trillion by volume (pptv) at 990 mbar (Klonecki, 1999). It can be seen in the reaction series of figure 1.4 one molecule of ozone is produced as well as one CO molecule is converted to CO_2. NO (figure 1.4 green) and OH (figure 1.4 yellow) are crucial to these reactions, but neither species has a net destruction or production in this reaction sequence. The cycling allows the reactions to continue until one of these species is lost in a termination step. For example, during the day NO_2 is removed slowly from troposphere by the reaction NO_2 + OH + M → HNO_3. HNO_3 can photolyze back, however its *e*-folding lifetime against photolysis is 15- 80 days, so HNO_3 is serving as a sink for nitrogen oxides. Also, because HNO_3 is soluble, most dissolves in aerosol particles or cloud drops before it photolyzes back to NO_2. Overnight, once there is no sunlight, the concentration of ozone can decrease because NO can react with ozone to produce NO_2 and O_2. This reaction mechanism is much different in low NO_x environments like the remote marine environment. Here instead of ozone concentrations being high during the day like in the aforementioned scenario, ozone is destroyed during the day, leading to a diurnal cycle with a daytime minimum because HO_2 reacts directly to destroy ozone (HO_2 + O_3). In this case ozone destruction is balanced by transport from the free troposphere (e.g., Ayers et al., 1992). Hydrocarbons other than CO, like methane for example, can be

oxidized by similar chain reaction mechanisms (figure 1.5). For methane oxidation, the first step involves the abstraction of a hydrogen atom from methane by the hydroxyl radical producing the methyl radical and water. The rest of the sequence is similar to the photooxidation of CO (figure 1.4) except here, the methylperoxy radical (CH_3O_2) converts NO to NO_2, whereas in the CO sequence, the hydroperoxy radical (HO_2) does this step.

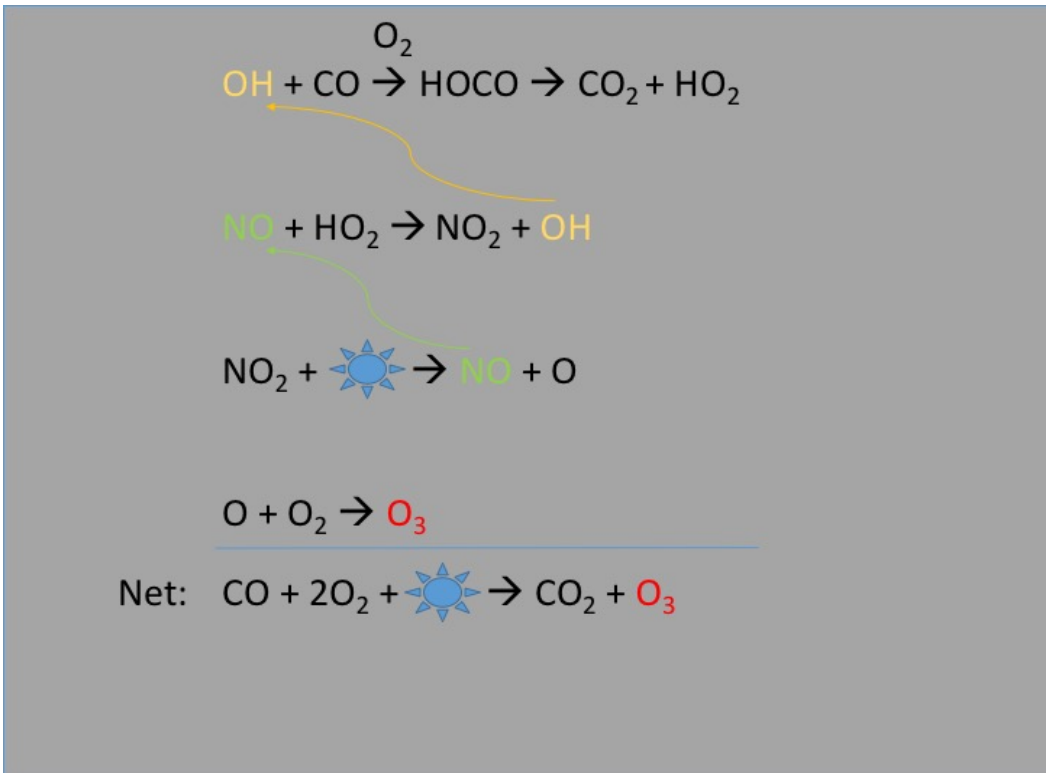

Figure 1.4: Ozone formation as the result of carbon monoxide (CO) oxidation in the presence of nitrogen oxides (NO and NO_2)

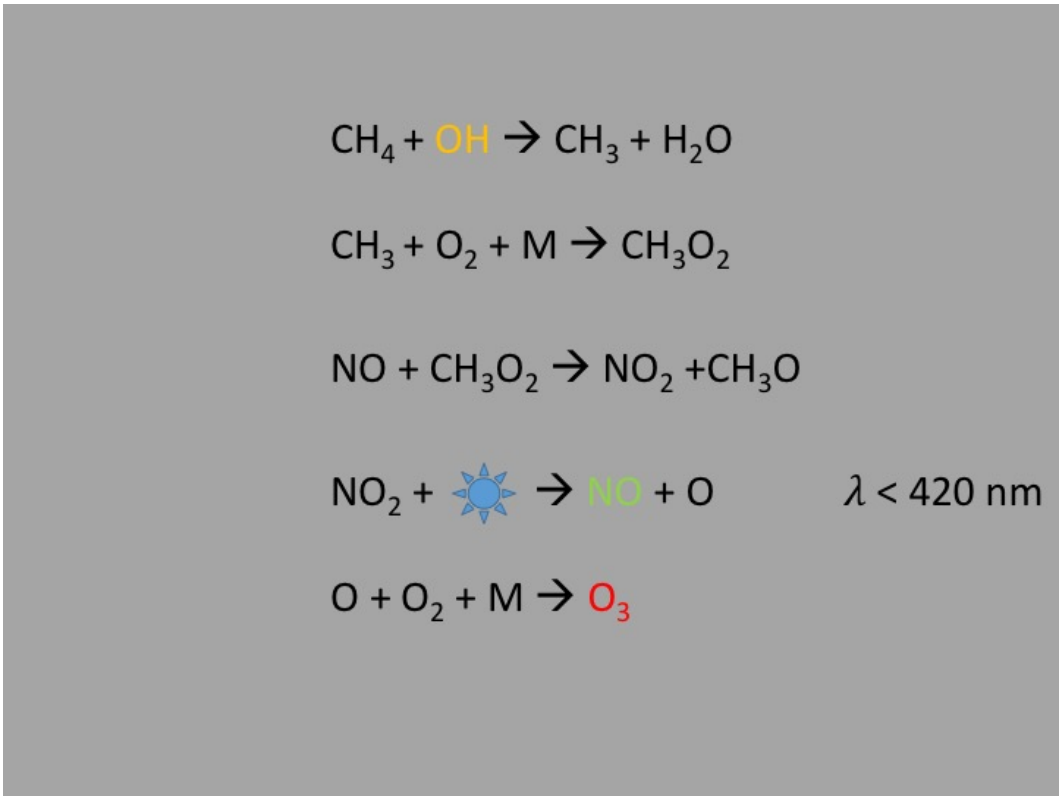

Figure 1.5: Photooxidation of methane in the presence of NO_x

When attempting to reconstruct past CO emissions, prior to the industrial revolution, fossil fuel-derived CO is nonexistent, thus the main sources of CO are methane oxidation, NMHC oxidation and biomass burning. Other sources of CO include direct biogenic emissions and direct emission by the breakdown of DOC from the ocean. However, their contribution is at most a few percent of the total (Wang et al., 2010, Park et al., 2015). Methane-derived CO is the largest source and is due to the abundance of CH_4 in the atmosphere, assuming steady state (valid for the ice core samples since the integrated time of a sample will be a few decades at the least). The steady state contribution of CO from methane is

calculated as the product of the ratio of the CO+OH and CH_4+OH rate constants and CH_4 concentration ($[CO]_{CH4,ss}=(k_{CH4+OH}/k_{CO+OH})*[CH_4]$). Methane concentration and isotopes have been measured directly from Antarctic ice (e.g., Mitchell et al., 2013; Sowers et al., 2010, Ferretti et al., 2005; Chappellaz et al., 1997; Mischler et al., 2009 and others) so its contribution can be measured directly. Direct emissions from the terrestrial and marine biosphere have been both measured and modeled, and are estimated to be very small (Park 2010; Park et al., 2015). Because the methane-derived CO is precisely calculated from observations of CH_4, we treat that source function as known. Since there is no fossil fuel-derived CO prior to the 18th century, the remaining unconstrained major source terms in the paleo CO budget are therefore NMHC oxidation by OH radical and biomass burning (Table 1.1). The sources of CO are explored in more detail in following chapter.

1.4 Seasonal variations of OH and CO

1.4.1 The hydroxyl radical

The average lifetime of CO is relatively short, ~2 months compared to interhemispheric mixing (~1 year). Therefore, local CO concentrations reflect local sources so if there are great interhemispheric differences those are mainly due to the variation of land and population between the two hemispheres. There is a strong latitudinal and seasonal dependence on CO concentration (figure 1.1 &

1.2). In winter, CO concentration is high relative to summer (~60 ppbv higher in NH and ~30 ppbv higher in SH) because removal rates for reaction with hydroxyl radical is low as hydroxyl radical exhibits its own seasonality and follows the annual solar radiation cycle producing less radicals when insolation is low.

The hydroxyl radical (OH) is the main way the troposphere rids itself of pollutants (e.g. CO, NMHC) and is the dominant sink for many greenhouse gases including methane. The abundance of OH varies spatially and temporally and is largely determined by the local distribution of CO, CH_4, NO_x and ozone, water vapor, higher order hydrocarbons as well as the amount of shortwave (<310 nm) UV radiation. One of the main sources of OH in the troposphere stems from the photodissociation of ozone by UV radiation and subsequent reaction with water to form 2 OH molecules as illustrated by the following reactions:

$$O_3 + h\nu \rightarrow O_2 + O(^1D) \quad (1)$$
$$O(^1D) + M \rightarrow O + M \quad (2)$$
$$O(^1D) + H_2O \rightarrow 2\ OH \quad (3)$$
$$O + O_2 + M \rightarrow O_3 + M \quad (4)$$

The M in reaction 2 and 4 denotes an inert reaction partner like nitrogen (N_2) and is needed to take away excess energy when two molecules or atoms collide to form a product. It should be noted that more than 97% of the O atoms that form in reaction 1 react back again to ozone (reaction 4). Only ~3 % further react and

form hydroxyl radical (reaction 3). There are other sources of OH including the photolysis of nitrous acid (HONO), hydrogen peroxide (H_2O_2) or peroxy-methane (CH_3OOH), the reaction of nitrogen monoxide (NO) with the hydroperoxy radical (HO_2) or the reaction of alkenes with ozone (e.g., Müller and Brasseur, 1999; Collins et al., 1999; Jaeglé et al., 2001; Tie et al., 2003; Singh et al., 2004). OH chemistry is fundamentally intertwined with the day-time reaction cycles of nitrogen oxides (NO_x). Globally averaged tropospheric OH radical concentrations are on the order of 10^6 molecule cm^{-3}, which corresponds to a tropospheric mixing ratio of only about 0.04×10^{-12} or 0.04 parts per trillion (ppt).

1.4.2 Seasonality of CO and its isotopes

Like OH, stable isotopic ratios ($\delta^{13}C$ and $\delta^{18}O$) as well as concentration of CO exhibit seasonal variation (Mak et al., 2003; Manning et al., 1997; Novelli et al., 1992; Röckmann et al., 1998) (figure 1.6-1.10). Stable isotopic ratios of CO are helpful to investigate the relative contribution of CO sources because different CO sources have a characteristic isotopic signature (discussed in detail Chapter 2) and thus help to better estimate the globally averaged CO budget.

At the end of the 20th century, during NH winter, it has been shown that $\delta^{18}O$ of CO is enriched, attributed to the decrease in OH. The enriched $\delta^{18}O$ of CO represents a build-up of fossil fuels, a main source of CO in the NH, and demonstrates how the sources outweigh the sinks (Röckmann et al., 1998). As the

annual solar radiation cycle progresses, during spring and summer, when length of daylight and solar altitude increase, the oxidative capacity of the atmosphere increases and with increasing OH, CO levels decline. Other work has reported seasonal variation of CO from Northern Hemisphere locations (Brenninkmeijer et al., 1998; Mak and Brenninkmeijer 1998 and Park et al., 2015). Brenninkmeijer et al. (1998) show results from Alert Canada located at 82º27'N 62º31'W in 1996-1997. Alert Canada data show a range of ~16‰ with values from -4‰ to ~12‰ for $\delta^{18}O$ of CO over the course of a year at this high latitude NH location. On the other hand, $\delta^{13}C$ of CO shows less variation with a range of ~5‰ with values from -29‰ to -24‰, which can be expected since $\delta^{13}C$ is not as sensitive to changes in fossil fuel burning. Mak and Brenninkmeijer (1998) observed seasonal variations throughout the year with regard to isotopic ratios and concentrations of CO in NH locations and also concluded that $\delta^{18}O$ of CO was enriched in both remote and urban areas resulting from fossil fuel combustion. This work reflects both the changing relative strengths of CO sources and the strength of the primary CO loss mechanism, reaction with OH (Mak and Brenninkmeijer 1998). In a more recent study by Park et al. (2015), air samples were collected to measure CO mixing ratios and stable isotopes $\delta^{13}C$ and $\delta^{18}O$ at a high northern latitude site (Westman Islands, Iceland) from January 2004 to March 2010. The results indicate a multiyear trend of the sources of atmospheric CO in the extratropical Northern Hemisphere (figure 1.6). More specifically, anthropogenic CO

emissions are mostly responsible for the observed variation in $\delta^{13}C$ and $\delta^{18}O$ of CO during 2004–2009. There was strong evidence that the $\delta^{18}O$ enriched sources such as fossil fuel and biofuel sources are controlling the variation.

The Southern Hemisphere, like the Northern hemisphere discussed above, also demonstrates seasonal variation in concentration and isotopes (figure 1.8 and 1.9). Manning et al. (1997) concluded that the variation exhibited in the extratropical SH was a reflection of the different patterns of burning (forest vs. savanna) throughout the season. More specifically, $\delta^{13}C$ of CO for C3 environments burned such as forests are depleted relative to C4 savanna environments burned. A seasonal cycle has also been observed for Scott Base, Antarctica, 77º51'S 166º46'E, for the years 1996-2004 (Park et al., 2015). CO concentrations ranged from about ~35 to ~70 ppbv while $\delta^{13}C$ of CO was at a minimum in April (~-32‰) and maximum in December (~-25‰ to -27‰). $\delta^{18}O$ of CO was at a minimum in December/January (-6‰ to -10‰) and a maximum in August-September (-1‰ to 2‰). From this data we can assume a modern SH CO concentration of 55.5 ppbv (±1ppbv) and $\delta^{13}C$ of CO = -29.4‰ (±.5‰) and $\delta^{18}O$ of CO = -3.6‰ (±.5‰).

The major sources of CO all seem to exhibit a seasonal pattern except for methane derived CO because of its long lifetime (~10 years). However, this is dependent upon latitudinal location. For example, in Antarctica, where there is no sunlight for several months the availability of OH is diminished and the methane

derived CO record does show a slight (4 ppbv) seasonal difference (Park et al, 2015) (discussed in detail in Chapter 4). For other sources, such as fossil fuel combustion, which is the dominant source in mid-latitude Northern Hemisphere, there is a seasonal trend and therefore a seasonal variation of fossil fuel-derived CO (Gros et al., 2001; Kato et al., 2000; Petron et al., 2004; Pfister et al., 2004; Röckmann and Brenninkmeijer, 1997; Park et al., 2015). Since fossil fuel combustion sources are concentrated in the extra-tropics around 30º-55ºN latitude they do not contribute to the SH CO budget (Khalil and Rasmussen,1990). On the other hand, biomass burning varies both spatially and temporally, and is typically strongest during the dry season, which is January-March for the NH and July-September for the SH (Crutzen and Andreae, 1990).

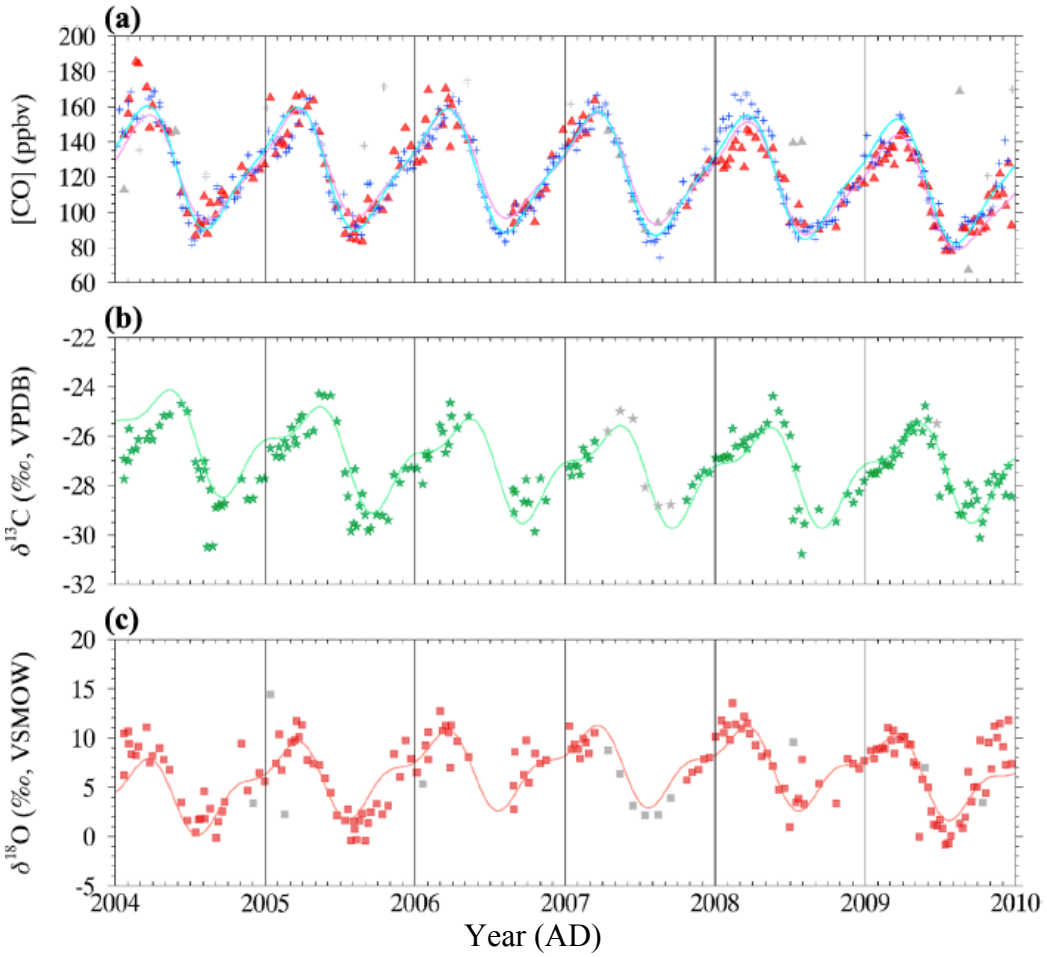

Figure 1.6: The observations of (a) [CO] (red triangles) from Park et al. (2015) and NOAA GMD [CO] (blue crosses); (b) $\delta^{13}C$ (green stars), and (c) $\delta^{18}O$ (brown squares) are from a high northern latitude station Iceland (63°N). The smooth fit curves using a low-pass Fourier Transform filtering method (Novelli et al., 1998; Thoning et al., 1989) are shown as the pink line ([CO]), the light green line ($\delta^{13}C$), and the light brown line ($\delta^{18}O$). The light blue line in (a) is a similar fit applied to the NOAA GMD [CO] data acquired at Iceland (Novelli and Masarie, 2010). To derive smooth fit curves, if there is no observation in one or two consecutive months, the least square quadratic interpolation is used to fill the missing months. For April through September in 2007, the missing months are filled with monthly mean of 2004–2009 observations. The gray data points indicate outliers or interpolated data. The results from the smooth fit curves are only used to compare the trend in annual averages and the seasonal cycle of the model results. In the other analyses, the measured results are monthly means of the observations and not derived from the fitted curve.

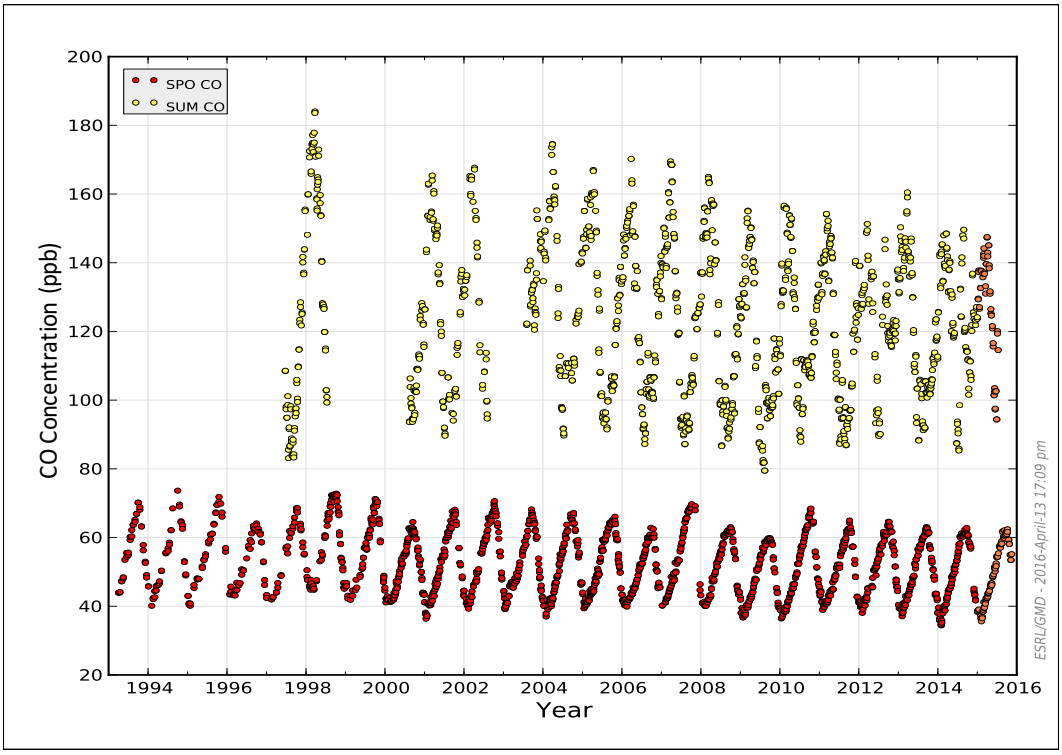

Figure 1.7: CO concentration in ppbv for a high NH location, Summit Greenland (SUM) 72.5800° N, 38.48° W (yellow) and CO concentration in ppbv for a high SH location, South Pole, Antarctica (SPO) 90.00° S, 59° E (red). Circles are average monthly values from sampling locations. Data from NOAA ESRL/GMD has an uncertainty of ±1 ppbv.

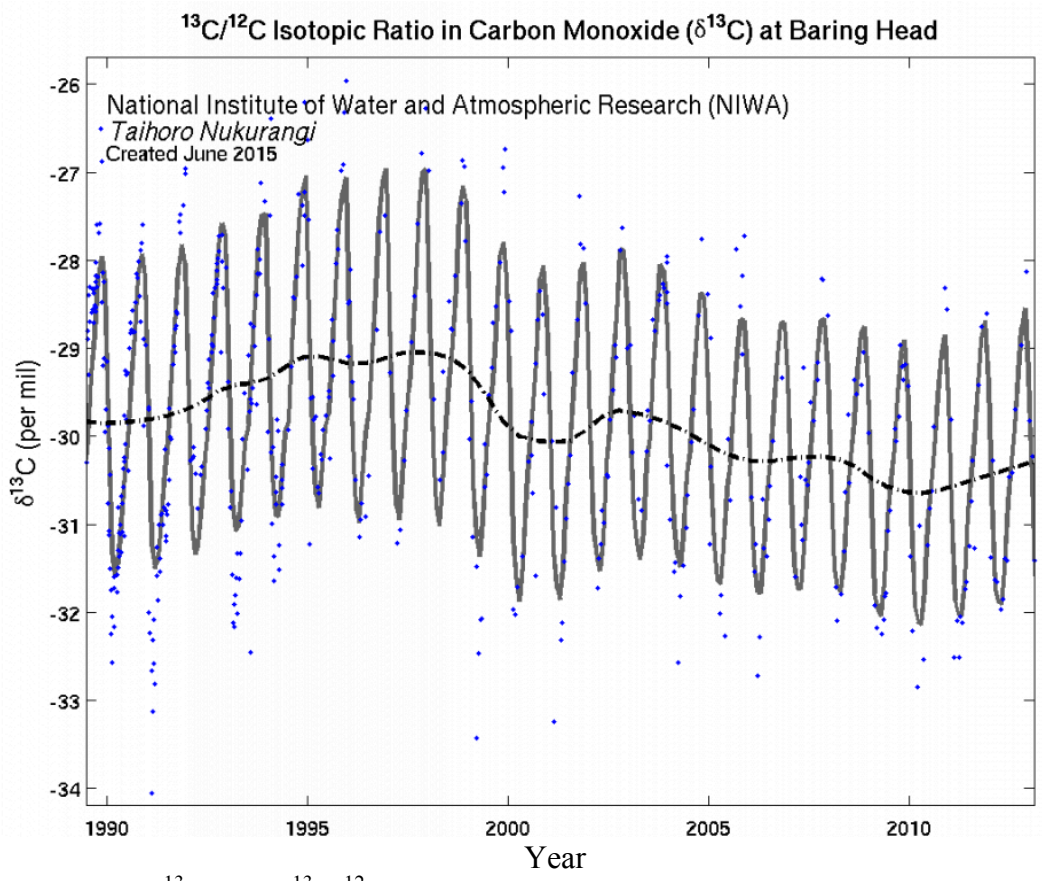

Figure 1.8: $\delta^{13}CO$ or $^{13}C/^{12}C$ isotope ratio in CO is shown as the relative difference from the Vienna Peedee Belemnite (VPDB) standard (Chapter 2) in per mil (‰). Individual flask measurements at Baring Head, New Zealand, 41.4° S, 174.9° E (blue diamonds) have been fitted with a smoothed curve (gray line) using Seasonal Decomposition of Time series by Loess (STL). The black line shows the smoothed curve with the seasonal cycle removed. Data from National Institute of Water and Atmospheric Research (NIWA) Tiahoro Nukurangi.

Figure 1.7, 1.9 and 1.10 show modern measurements of CO concentration. The data reveal (figure 1.9) a 21-year record of atmospheric CO from 1994 - 2015 from air in glass flasks collected at a high latitude SH location, South Pole, Antarctica (SPO) 90.00° S, 59° E as reported by NOAAESRL/GMD. Concentration stayed relatively constant during this time period and exhibited

only a slight decrease of ~4 ppbv over the 21 years. In contrast, for the Northern Hemisphere the record (figure 1.10) is more dynamic and we see a decreasing trend in CO concentration from Barrow, Alaska (figure 1.10). The decrease of ~25 ppbv that is observed is thought to be from a reduction in fossil fuel emissions that occurred in the 1990s in NH mid-latitude locations (Boden et al., 2009). The NOAA flask measurements of CO concentration are consistent with the decrease in CO observed from MOPITT satellite data for 2000-2014 (figure 1.2).

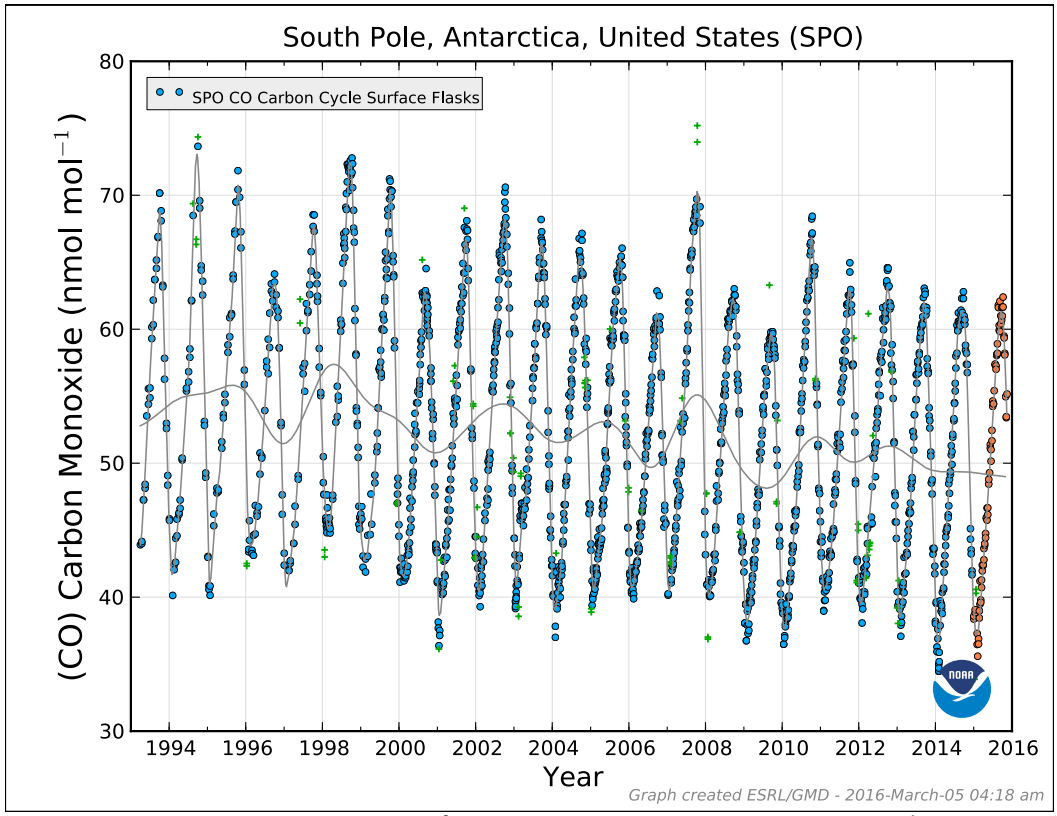

Figure 1.9: CO concentration in 10^{-9} mol CO per mol of dry air (nmol mol^{-1}) for a high latitude SH location, South Pole, Antarctica (SPO) 90.00° S, 59° E. Circles (blue) are regionally representative of a remote, well-mixed troposphere. The grey line

represents a smooth curve and long-term trend. Data shown in orange are preliminary. Data from NOAA ESRL/GMD possess an uncertainty of ±1 ppbv.

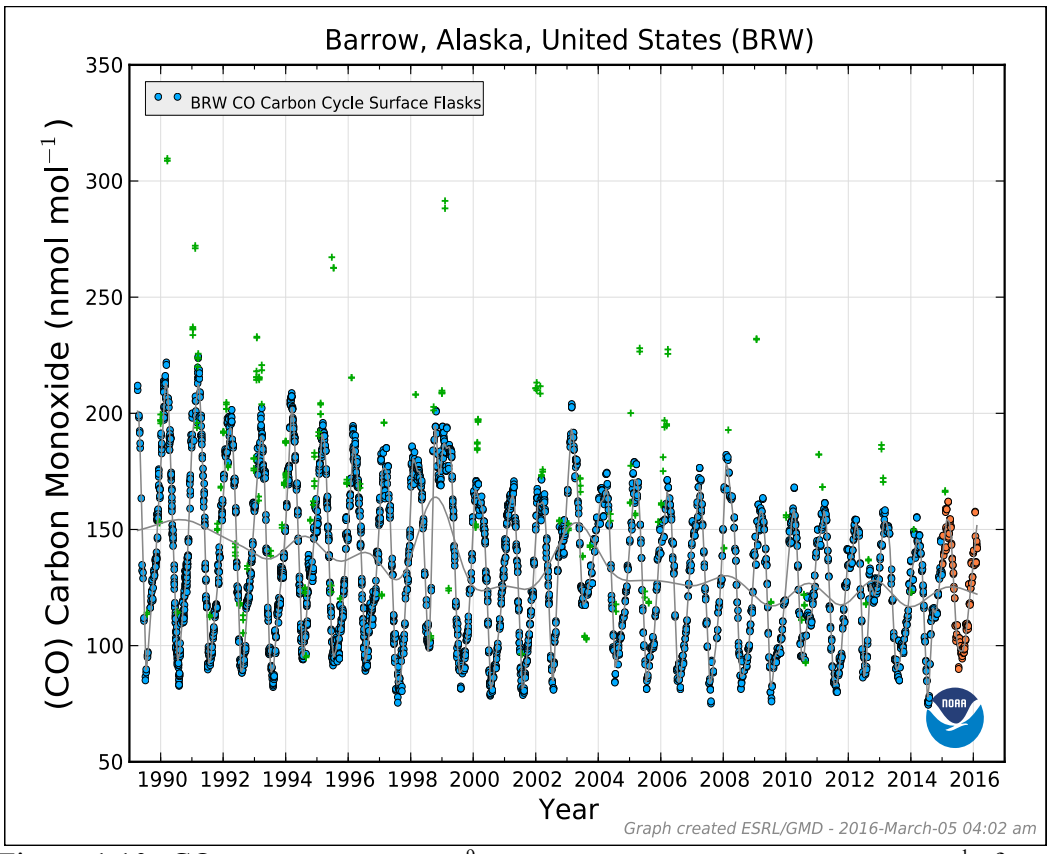

Figure 1.10: CO concentration in 10^{-9} mol CO per mol of dry air (nmol mol^{-1}) for a high latitude NH location, Barrow, Alaska USA (BRW) 71.32° N, 156.61° W. Circles (blue) are regionally representative of a remote, well-mixed troposphere. The grey line represents a smooth curve and long-term trend. Data shown in orange are preliminary. Data from NOAA ESRL/GMD possess an uncertainty of ±1 ppbv.

1.5 Methane budget and atmospheric chemistry

Methane has varied considerably over the last 10,000 years (figure 1.11). This time span is therefore interesting as CO concentration changes are related to CH_4. Moreover, CH_4, OH and CO form a complex system in the atmosphere

(figure 1.12). Both CH_4 and CO are oxidized by OH (figure 1.4 and 1.5.). Furthermore, the oxidation of methane is responsible for ~25% of CO produced globally, however in the remote SH this mechanism is responsible for ~40% of the CO present (Bergamaschi et al., 2000). As an example of the CH_4-OH-CO cycle, it was shown and discussed using a model employing … that the increase of CO in the Northern Hemisphere in 1997–1998 due to biomass burning caused a decrease in OH and therefore a decrease of CH_4 removal (Butler et al., 2005).

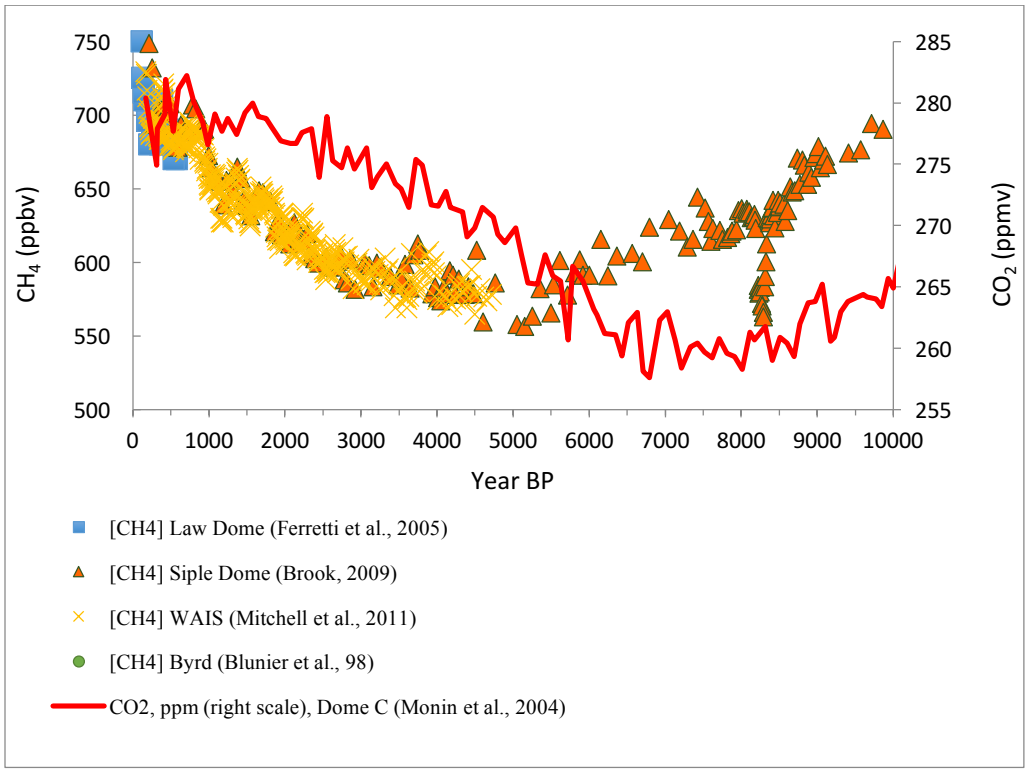

Figure 1.11: CH_4 (left scale, in ppbv) and CO_2 (red line) (right scale, in ppmv) record from Antarctic ice cores over the past 10,000 years.

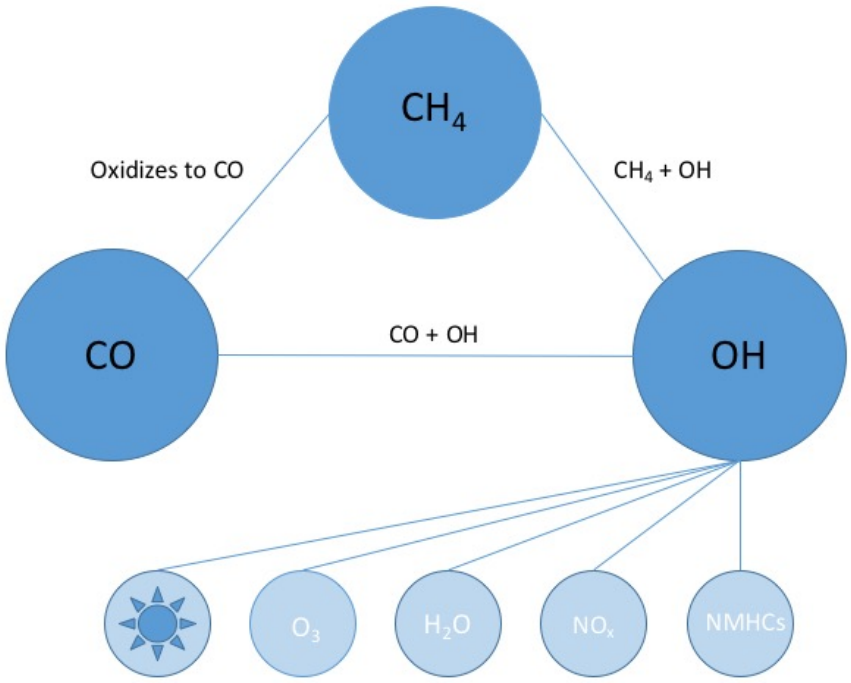

Figure 1.12: Simplified CH_4, OH and CO cycle

Ice core records indicate an increase of atmospheric methane since the mid-Holocene (~5,000 years ago) as displayed in figure 1.8 and figure 1.10 (Spahni et al., 2005). The cause for this increase is under debate (Ruddiman, 2003; Spahni et al., 2005; Chappellaz et al., 1997; Singarayer et al., 2011). There are four mechanisms proposed to explain the Holocene methane trend: An increase in tropical emissions (Chappellaz et al., 1997; Brook et al., 2000), an increase of circum-Arctic wetland emission (Sowers, 2010; Fischer et al., 2008), an increase in agricultural activity (Ruddiman, 2003; Ruddiman et al., 2008) and most recently from natural changes in Earth's orbital configuration (Singarayer et

al., 2011). Singarayer et al. (2011) believe that natural changes in Earth's orbital configuration are linked to precession-induced modification of seasonal precipitation with enhanced emissions in the Southern Hemisphere tropics. If the mechanism were strictly limited to the Northern Hemisphere, we would not expect significant changes in the Southern Hemisphere CO budget as a result of that same mechanism, since the lifetime of CO (weeks to months) is much shorter than the mean interhemispheric transport time (~1 year). However, it is possible that we may see structure within the CO record if the cause(s) of the observed CH_4 increase are regional within the Southern Hemisphere. For example, if both the trend in CO concentration and $\delta^{18}O$ of CO correlates with methane, it is likely that biomass burning was the main contributor to both, since biomass burning is a significant contributor to global methane emissions. If it deviates from methane that could suggest that some other sources are involved and should be investigated further. Significant variations in CH_4 concentrations have been documented in the recent past, which will impact the CO budget as well as global atmospheric chemistry. There is still a question as to what caused the increase in CH_4 over the past several thousand years (figure 1.13). A record of past [CO] and CO isotopes will contribute to a better understanding of the CH_4 budget. For example, global or hemispheric changes in biomass burning, which is a significant contributor to global CH_4 emissions, would be detected via [CO] and CO isotopes and could be used to help settle debate over the origin of the CH_4 rise.

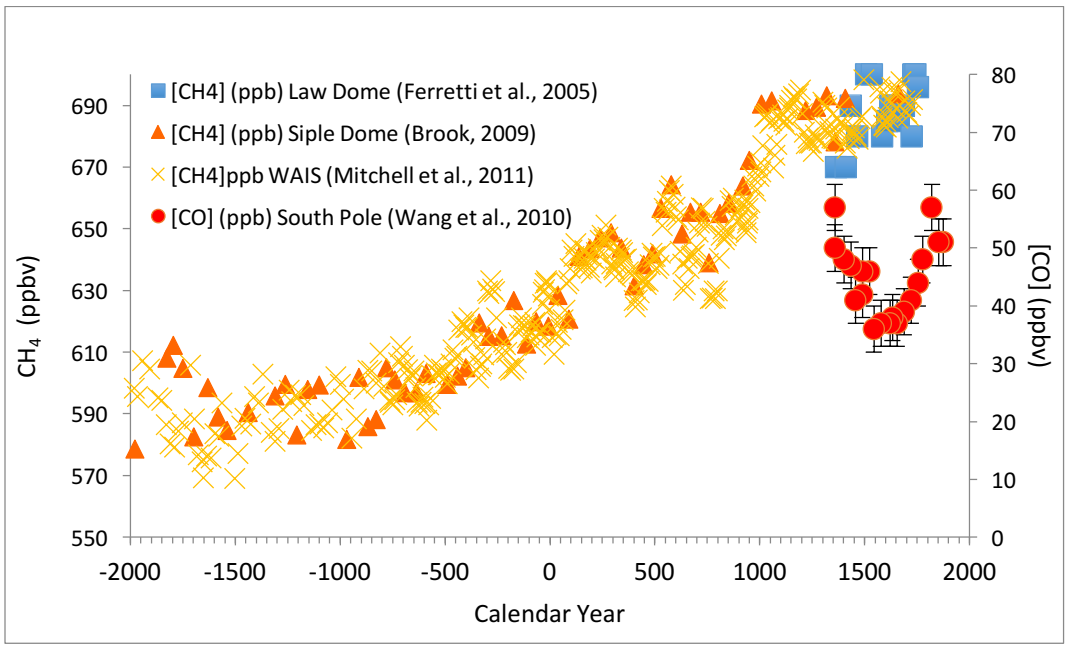

Figure 1.13: CH_4 and CO concentration record from Antarctic ice cores. Gas concentrations are plotted versus calendar year.

Additionally, CO plays a major role in global atmospheric chemistry because of its interaction with hydroxyl radical. There have been several modeling studies that investigated deglacial changes in the oxidative capacity of the atmosphere providing insight to past CH_4 sinks (Levine et al., 2011; Murray et al., 2013). However, available paleo-atmospheric data provide insufficient constraints for such studies (e.g., Levine et al., 2011). The key parameters needed to characterize large-scale tropospheric chemistry include OH, CO, CH_4, NO_x, and NMHC. Currently, of all those species, only CH_4 (and in some cases $\delta^{13}C$ of CH_4) is well understood. Analyzing ice from WAIS Divide and Dome C will allow me to expand the existing Antarctic CO data set and reconstruct the temporal evolution

of CO source strengths over the last few thousand years. Adding the record of [CO] from the Holocene together with isotopic constraints on the CO budget, will provide another useful parameter for atmospheric chemistry models studying the past 3,000 years. This will lead to better estimates of Holocene changes in atmospheric oxidative capacity. This CO isotope record for that time period will represent novel and unique data that will help to better understand the overall stability of the tropospheric CH_4-CO-OH cycle (figure 1.12).

1.5.1 Methane isotopes in ice cores

Isotopic analyses in ice cores provide a wealth of information on past climatic events and can be a valuable tool in determining past variations in sources and sinks (Ferretti et al., 2005; Francey et al., 1999; Schaefer and Whiticar, 2008; Sowers et al., 2002; Sowers et al., 2005b, Wang et al. 2010). As an example, $\delta^{13}CH_4$ has been used to investigate changes in methane cycling throughout time. This work started with Harmon Craig who proposed an increase of 2‰ of $\delta^{13}CH_4$ over the industrial period derived from polar ice cores, attributing the enrichment to anthropogenic biomass burning as the principle cause of this enrichment (Craig, 1953; Craig et al., 1988). A 2005 study reported a 2000 year high resolution record of methane concentration and $\delta^{13}CH_4$ from Law Dome Antarctica (Ferretti et al., 2005). Their $\delta^{13}CH_4$ data showed a 2‰ depletion with a minima ~1700 AD and modeled methane source partitioning implies that a

~10 ±1 Tg reduction in annual global biomass burning emissions of methane is the main cause of the $\delta^{13}CH_4$ depletion from 1000 to 1700 AD (Ferretti et al., 2005). A more recent study presents changes in methane cycling over the past 160,000 years by measurements of the carbon isotopic composition $\delta^{13}CH_4$ of in Antarctic ice cores from Dronning Maud Land (DML) and Vostok. This study finds that variations in the $\delta^{13}CH_4$ are not generally correlated with changes in atmospheric methane concentration, but instead more closely correlated to atmospheric CO_2 concentrations (Moller et al., 2013). It is thought that this reflects a climatic and CO_2-related control on the isotopic signature of methane source material, such as ecosystem shifts in the seasonally inundated tropical wetlands that produce methane, but this is under debate (Moller et al., 2013). Another recent study made high-resolution $\delta^{13}CH_4$ measurements of air trapped in NH ice cores from the North Greenland Eemian Ice Drilling program (NEEM) and from the EUROCORE (Sapart et al., 2013). This data also saw the same minimum as the aforementioned work, but it was revealed that $\delta^{13}CH_4$ exhibited pronounced centennial-scale variations between 100 BC and 1600 AD. Model results show that the centennial-scale variations in isotopic ratios can be attributed to changes in pyrogenic and biogenic sources. The changes in sources are thought to be brought on by anthropogenic changes in population and land use as well as natural climatic variability such as the Medieval Climate Anomaly and the Little Ice Age (Sapart et al., 2013).

1.6 Biomass burning

Biomass burning is a contributor to and an indicator of climate variations. Climate and biomass burning are directly correlated, as biomass burning is a function of temperature, humidity/precipitation and fuel load (Swetnam, 1993; Westerling et al., 2006; Kitzberger et al., 2007). The connection between climactic conditions and biomass burning has been previously reported in many studies. For example, Kitzberger et al. (2001) report more fire occurrences after El Niño/La Niña events in the south-western United States and Patagonia, Argentina (two regions of similar fire-climate relationships that are affected by El Niño Southern Oscillation (ENSO)).

El Niño events are typically characterized by enhanced growth rates of plants due to the increase in availability of moisture at these mid-latitude western Americas locations. This allows a reservoir of fuel to build up. La Niña events (which follow an El Niño event) are associated with drier conditions resulting in greater fire ignitions of the accumulated fuel and widespread burning. Power et al. (2008) demonstrated that large-scale climate controls such as temperature and drought correlate to fuel load and local changes in vegetation. The records imply that changes in fire regimes due to changing climactic conditions may have had important controls on the global carbon budget over time. Furthermore, local variations in biomass burning in the modern Northern Hemisphere are correlated to drought and temperature but it is less clear if this is the case in the Southern

Hemisphere (Power et al. 2012).

Biomass burning not only is an indicator of variations in climate conditions, but can also have an impact on climate through chemistry interactions and radiative forcing. For example, emissions of significant amounts of reactive gases (e.g. CO) can alter the oxidation state of the atmosphere. This in turn will have an impact on the mean lifetimes of certain radiatively active gases, such as CH_4 (Andrea and Merlet, 2001). For example, the reaction CO+OH is the main sink for both CO and OH, with CO occupying approximately 60% of the atmosphere's OH based oxidative capacity (Crutzen and Zimmermann, 1991)**.** An increase in the concentration of CO can therefore cause a decrease in atmospheric OH concentration, resulting in a buildup of other gases, such as methane, which is primarily removed by OH. CO is considered to be an important indirect greenhouse gas for this very reason (IPCC, 2001). In addition, under high NO_x conditions, the oxidation of CO leads to the production of ozone (figure 1.4). Furthermore, biomass burning can have an impact on CO_2 concentrations (Seiler and Crutzen, 1980), particularly in preindustrial times. Since preindustrial times, biomass burning-derived CO_2 is responsible for an estimated 19% of the increased radiative forcing (Bowman et al., 2009). Emissions of particulates including black carbon will also have direct effects on radiative forcing. In addition, water vapor, the strongest greenhouse gas, is produced during biomass burning which can furthermore support the formation of clouds (assuming there is

a cloud condensation nuclei available) and influence forcing. Clearly, there is a relationship between burning and chemistry and chemistry and climate.

1.6.1 Sedimentary charcoal record

Presently the most complete reconstruction of biomass burning and our understanding of its trends is based primarily on the records of charcoal found in lake, marine and peat sediments (Carcaillet et al., 2002; Marlon et al., 2008; Marlon et al., 2013). There is significant regional variation in biomass burning but overall global trends can be derived from charcoal data. The charcoal record reflects the controls of fire – mainly changes in climate (e.g. temperature and precipitation) and human activities (e.g. the expansion of agriculture) (Power et al., 2008; Marlon et al., 2008; Marlon et al., 2013). On long timescales, temperature is the main control of biomass burning through its influence on vegetation and fuel load (Harrison et al., 2010). Power et al. (2008) show that there is an increase in globally-averaged biomass burning during the transition from the last glacial maximum to the Holocene, consistent with an increase in global temperatures during deglaciation (21,000 to 11,000 calendar year BP). They also report increases in biomass burning in Australia and southern South America (SSA) during the last deglaciation (figure 1.14).

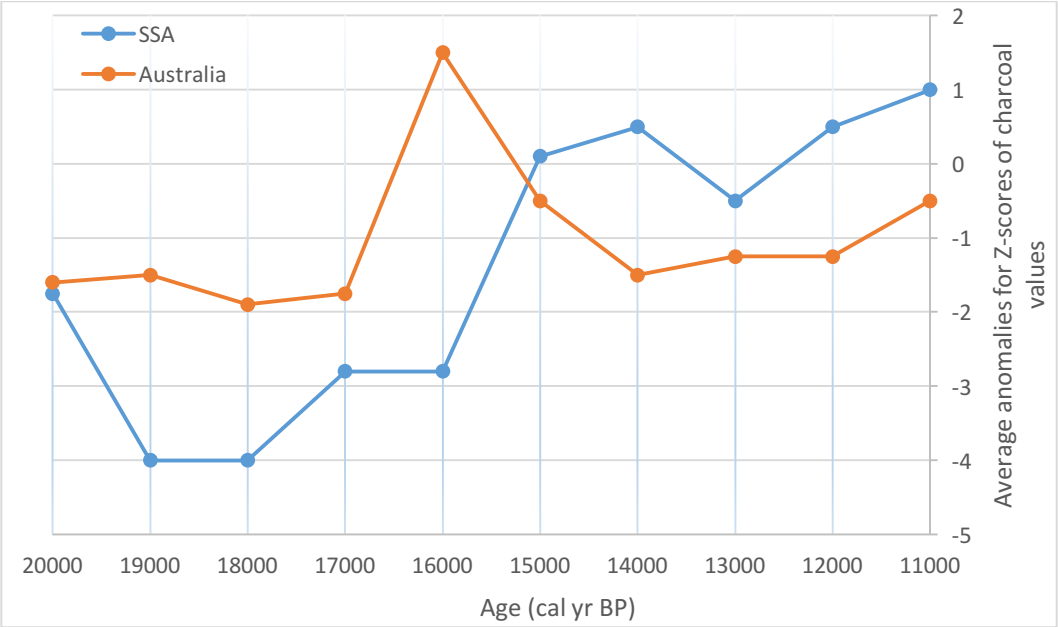

Figure 1.14: Regional averages of anomalies for Z scores of charcoal values from southern South America (>30ºS) (blue) and Australia (>10ºS to <50ºS). Data from Power et al., 2008.

Furthermore, van der Werf et al. (2013) reports that biomass burning emissions from these two locations is most influential on [CO] measured in South Pole ice cores. When averaged globally, fire activity was low during the early Holocene (11.7-8 ka) and increased during the Holocene, consistent with the global increase in temperature through the glacial-interglacial period (Marlon et al., 2013). However, when looking at the charcoal record from different regions discrepancies exist. For example, the charcoal record from the Pacific Islands indicates a moderate but declining level of biomass burning for the first half of the Holocene then relatively low burning activity during the mid-Holocene (8-4 ka) followed by an increase in burning in the late Holocene (4-0 ka). The regional

nature of this pattern suggests climate changes are responsible as opposed to human colonization (Marlon et al., 2013). Furthermore, the late-Holocene increase in burning in New Zealand has been linked to an increase in droughts due to the intensification of ENSO circulation patterns (McGlone et al., 1992). The sedimentary charcoal record is a relatively good proxy for biomass burning but the record is mostly local in nature and can vary greatly from one location to another. When attempting to extend the record back through the Holocene, large spatial gaps exist. Extending the CO record derived from ice cores will help to investigate the discrepancies in the charcoal record and help fill the spatial gaps.

Another record of biomass burning that reflects regional-scale variation is black carbon measured in ice cores. It has been reported that changes in black carbon occurred over the past 150 years based off of samples from the WAIS Divide ice and Law Dome ice core, both from Antarctica (Bisiaux et al., 2012). In theory, black carbon should be a good proxy, however, its short lifetime (days) makes it a tracer of regional variations and not a suitable tracer when considering hemispheric variation. For example, atmospheric transport can play a dominant role in these records (Bisiaux et al., 2012). CO is a complementary tracer for identifying hemispheric-scale changes in biomass burning because it is a gas with a suitable lifetime. The work presented here will add to the currently available data from charcoal records and the new information from black carbon.

Over time, naturally occurring fire and human activity are the primary

causes of variations in biomass burning. Carcaillet et al. (2002) show that biomass burning is significantly impacted by anthropogenic sources. It is assumed that as one extends the record back in time, the contribution from anthropogenic sources decreases to near zero because of decreasing population density, especially in the Southern Hemisphere. However, Ruddiman et al. (2003) report this assumption is not universally accepted. For the latter part of the Holocene, population/human practice is relatively well constrained for the Northern Hemisphere but population dynamics in the Southern hemisphere is less definitive. Studying the variations in biomass burning could potentially give new insight into human practices operating in the Southern Hemisphere. It is therefore necessary to quantify the CO isotope record in the Southern Hemisphere because any significant biomass burning component would be reflected in the record.

1.7 Dissertation objectives

The overall objective of this dissertation is to advance our understanding in the source evolution of CO in the Southern Hemisphere. This work focuses on the extraction of CO from Antarctic ice cores. Specific objectives include measuring the stable isotopes $\delta^{13}C$ and $\delta^{18}O$ of CO and quantifying CO concentration over the last ~250 years as well as reconstruct the relative source strengths of CO, in particular the biomass burning-derived CO. To achieve this, a new one-of-a-kind cryogenic vacuum extraction line was built and coupled to state-of-the-art

chemical instrumentation were used to quantify concentration and isotopes of CO over the past ~250 years.

Here I present atmospheric [CO] and stable CO isotopes ^{13}CO and $C^{18}O$ from 1700 - 1950 AD as recorded in bubbles trapped in ice cores from WAIS Divide, Antarctica. In particular, this study will help to better constrain the sources of atmospheric CO in the Southern Hemisphere during the late Holocene, including the contribution from biomass burning. The relationship between CO and CH_4 over this time period will be constructed based on these new observations and previously published CH_4 paleo data. Overall, the results obtained from this study will improve our understanding of CO and the overall stability of tropospheric chemistry of the CH_4-CO-OH cycle.

2 Background and Theory

2.1 Isotope effects

In the most elementary description, atoms are made up of positively charged particles (protons), negatively charged particles (electrons) and neutrons, which carry no charge. The defining property of an element is the number of protons it has in its nucleus. In a neutral atom the number of electrons balances that of the protons. The specific configuration of the electrons around the nucleus gives atoms its unique gross chemical properties. While the number of protons will always remain the same for an element, the number of neutrons can change. Varying the amount of neutrons in the nucleus of an atom does not affect the elements (or its compounds) unique gross chemical properties but the difference in mass with varying neutrons can cause slight chemical and physical differences between compounds containing elements of varying neutrons. Furthermore, these slight differences make up the foundation of this thesis.

An isotope of a particular element is defined by the number of neutrons in its nucleus. Different isotopes of the same element are nearly the same chemically meaning they have the same electronic configuration. However, slight chemical differences exist between isotopes so chemical reactions may fractionate the isotopes. Fractionate simply means to partition unevenly, (i.e., light isotopes somewhat enriched in one part of the system, while heavier isotopes enriched

somewhere else). This fractionation effect can be useful in many ways. For example, fractionation may be temperature dependent and can provide potential paleothermometers (Epstein et al., 1953 and Emiliani, 1955). Also, different mechanisms for reactions may have differing fractionations (Urey, 1947) In these cases, occurrences of certain reaction mechanisms might be inferred from isotope ratios. Lastly, different sources of an element or compound may have distinct isotope ratios, and we can use isotope abundances as indicators of source or mass balance and that is what is exploited in this study.

Fractionation separates isotopes of a given element by chemical, biological or physical processes and can involve chemical bonds or not. For example, let's consider the gaseous diffusion of H_2 vs. D_2 (an isotope of hydrogen). At any given temperature the average kinetic energies H_2 and D_2 are equal, where kinetic energy = $1/2\ mv^2$. Because D_2 is double the mass, its velocity is less by a factor of $\sqrt{2}$, therefore it diffuses more slowly. As an example, if we take a mixture of H_2 and D_2 and let it diffuse through a narrow tube the results would tend to show H_2 molecules come out first and the and D_2 molecules exit later. This process is demonstrating the partial separation of isotopes which is what we call isotopic fractionation. In the aforementioned example there is no chemical bonding taking place. However, fractionation may involve chemical bonding/isotopic chemical reactions and an example of this is the evaporation of $H_2{}^{16}O$ vs. $H_2{}^{18}O$ (two isotopologues of water). As the phase change of

evaporation commences, water breaks the hydrogen bonds and escapes liquid water. It turns out that $H_2{}^{16}O$ breaks hydrogen bonds with other water molecules more easily than $H_2{}^{18}O$. This effect is small but observable. Lighter isotopes are preferentially evaporated so vapor entering the air is enriched in $H_2{}^{16}O$ relative to the liquid water it originated from (by about 1%). While we can observe this experimentally, it contradicts classic physics; i.e. bond enthalpies/strengths are the same as they are determined by electronic configurations only, and all isotopes of an element have the same number of protons and thus the same electronic configuration. So how is possible for lighter isotopes to more readily break their bonds? For an answer, we must look to quantum mechanics. In short, bond energies are slightly different because of quantum effects.

A core principle in quantum mechanics is chemical bonds have particular discreet energy levels, and can't exist with energies other than those levels. This is because of the wave nature of matter (e.g. similar to harmonics on a guitar string). In addition, even at absolute zero, there is some fundamental vibrational energy (E), termed zero-point energy (ZPE) and is calculated as vibrational energy:

$$E=\tfrac{1}{2}h\nu \qquad (5)$$

where h is Planck's constant (6.624×10^{-34} J/sec) and ν is the frequency (sec^{-1}). Because of the associated ZPE the bond does not settle into the lowest energy point on the curve (figure 2.1).

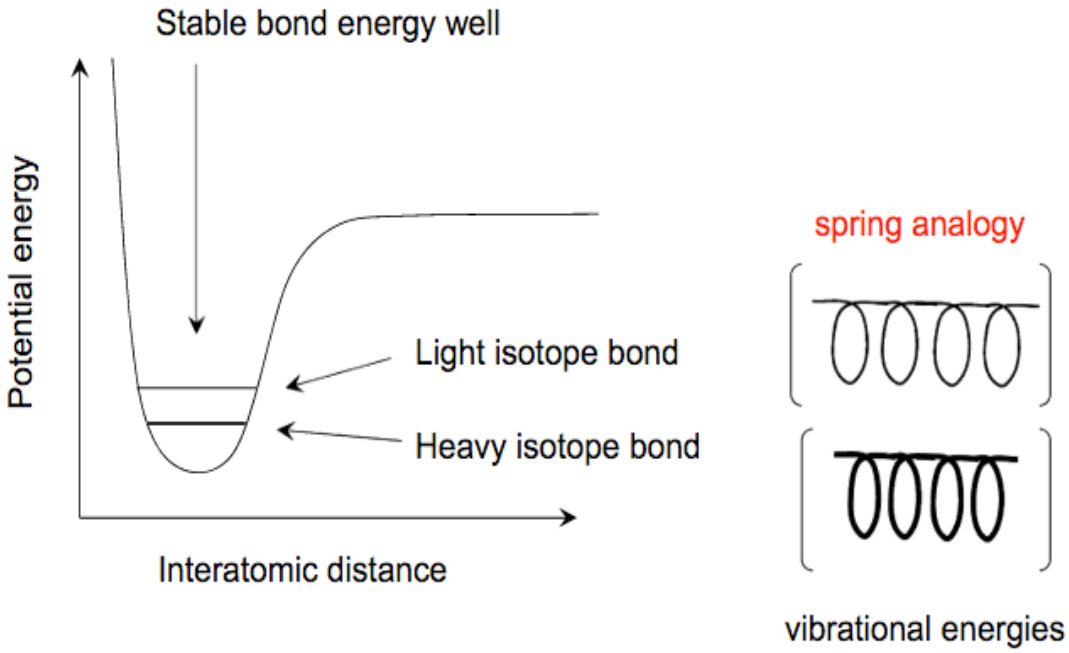

Figure 2.1: Potential energy curve for a light and heavy isotope bond. Based off Fry, 2006.

Figure 2.1 shows the potential-energy diagram (energy well) for bonds with light isotope atoms and heavy isotope atoms. In this classic model the bond can be thought of like a spring and it has energy based on how compressed or stretched (separation distance) it is. However, from observation of real molecules this model is not true. Rather, the molecules have discreet energy levels. Experiment and theory tell us the lowest energy is not zero but rather the zero-point energy. Zero point energies are lower for bonds involving heavy isotopes (bold line) than for lighter isotopes. In figure 2.1, the horizontal lines in the energy well represents the actual energy of a ground state molecules while the ZPE is the distance between the lowest point on the energy function and the

horizontal line. Light isotope bonds have slightly higher zero-point energies than heavier ones (figure 2.1). The energy needed to dissociate the light isotope bond is less than what is needed to dissociate the heavy isotope bond (bold line) because the heavy isotope bond molecule has a lower zero-point energy.

2.1.1 Kinetic isotope effects (KIE)

Isotopic effects include fractionation that occurs when bond energy is altered because of varying atomic mass (Equilibrium Isotope Effects) or when bonds are broken or rearranged (Kinetic Isotope Effects, KIE). When fractionation is kinetic, it involves rates and extent of processes (metabolic, physical). Kinetic isotope effects are normally associated with processes that are unidirectional, fast or incomplete such as diffusion, dissociation reactions, evaporation and almost all biological reactions. For diffusion and evaporation, KIE are explained by the varying translational velocities that the different isotopologues of a molecule possess as it crosses a phase boundary or moves through a phase. Let's consider as an example, the isotopologues $^{12}C^{16}O$ and $^{12}C^{18}O$, which have molecular masses of 28 and 30, respectively. Kinetic theory says that the average kinetic energy (KE) per molecule is the same for all ideal gases at a given temperature. If we equate the kinetic energies of the isotopologues at some temperature (T) we have:

$$KE\ (^{12}C^{16}O) = KE\ (^{12}C^{18}O) \quad (6)$$

and

$$KE = 1/2mv^2\ , \quad (7)$$

where m is mass and v is velocity. Substituting in the masses of the isotopes of CO, the equation reduces to

$$1/2(28)(v_{28})^2 = 1/2(30)(v_{30})^2, \quad (8)$$

or

$$v_{28} = \sqrt{30/28}\ v_{30} = 1.035v_{30}. \quad (9)$$

What this reveals is that no matter the T, the average velocity of the lighter isotope molecule $^{12}C^{16}O$ is 3.5% greater than the average velocity of the heavy isotope molecule $^{12}C^{18}O$ in the same system. The differences in velocity leads to isotopic fractionations in many different ways. For example, with evaporation, the lighter isotopologues of water have greater average translational velocities allowing them to preferentially break through the liquid surface, resulting in an isotopic fractionation between vapor and liquid that is superimposed on the equilibrium isotopic fractionation. This is observed in nature by looking at water vapor over a large lake or ocean. The vapor in these environments has a $^{18}O/^{16}O$ ratio that is much lower than the ratios that would occur at equilibrium. This is a direct result of the kinetic isotope effects associated with evaporation.

CO and methane are both removed from the atmosphere by homogenous gas phase oxidation reactions with OH. Isotopic fractionation occurs when CO

and methane react with OH radical due to the kinetic isotope effect, which is a result of the lower zero-point energy of the quantum vibrational state for an isotope of greater mass (as discussed in detail above). CO is particularly interesting because its two constituents, carbon and oxygen, have opposite KIE when considering CO + OH oxidation reaction. The kinetic fractionation of ^{13}C has a strong pressure dependence with an average strength of 4 to 5‰ in the lower troposphere (Röckmann et al., 1998, Steven and Wagner, 1989). However, there is an inverse isotope effect of approximately −10‰ for ^{18}O as measured by Röckmann et al. (1998) and Stevens and Wagner (1989), but this kinetic isotope effect shows only a weak pressure dependence. An inverse effect means that there is still a mass dependence, however, with an inverse effect there is a preference for the heavier isotope instead of the lighter isotope. The measured inverse kinetic isotope effect for ^{18}O is thought to occur because of isotopic substitution of the relative rate of unimolecular dissociation of the HOCO intermediate to reform reagents versus dissociation to products. However, this is phenomenon is not well understood to date and requires further investigation (Steven and Wagner, 1989; Brenninkmeijer and Röckmann, 1997 and Feilberg et al., 2002). This laboratory measurement was confirmed by field measurements by Brenninkmeijer and Röckmann (1997) using Southern Hemisphere aircraft data to calculate the fractionation effect to be -8‰. A result of this is that ^{12}CO and $C^{18}O$ will preferentially react with OH. This leaves the resulting CO enriched in ^{13}C and

depleted in ^{18}O. An important caveat to this is that below 400 mbar the isotope effect for ^{13}C follows an inverse effect, where ^{13}CO reacts faster with OH than ^{12}CO (Brenninkmeijer, 1999).

2.1.2 Equilibrium isotope effects

Equilibrium isotope effects deal with the effect that different atomic masses have on bond energy. When comparing a light isotope to a heavy isotope in a molecule, the electronic distributions and nuclear charges are the same. However, the different isotopes will exhibit slightly different internal energies due to mass differences and this causes a slight preference for the heavy isotope to be partitioned into one phase relative to another. According to Schauble (2004), equilibrium fractionation between two phases generally decreases with increasing temperature, proportional $1/T^2$. Since fractionation varies regularly with temperature, this can be used to estimate the temperature of formation (e.g. water and a precipitating phase like biogenic carbonate). Also notable is that the degree of fractionation is almost always bigger for elements whose mass ratio is significant, where mass ratio is defined as $m_{heavy} - m_{light}/m_{heavy}m_{light}$ and m_{heavy} and m_{light} are the heavy and light isotopes, respectively.

2.2 CO isotopes

The stable isotopes of carbon and oxygen in CO, ^{12}C, ^{13}C, ^{16}O, ^{17}O and ^{18}O occur on Earth at levels of 98.89% and 1.11% (for carbon) and 99.76%, 0.04%, and 0.20% (for oxygen) (Röckmann and Brenninkmeijer, 1998), respectively. Relative isotopologue abundance is expressed in delta units of per mil (δ), defined as:

$$\boldsymbol{\delta = \left(\frac{Rsample}{Rreference} - 1\right) \text{ x 1000, per mil }} \quad , \tag{10}$$

where R is the isotope ratio of the minor isotopologue to the major isotopologue (e.g., $^{13}C/^{12}C$ for carbon ($\delta^{13}C$), $^{18}O/^{16}O$ for oxygen ($\delta^{18}O$)). The reference material has been established by the International Atomic Energy Agency (IAEA) as Vienna Pee Dee Belemnite (V-PDB) for carbon-13 and Vienna Standard Mean Ocean Water (VSMOW), for oxygen-18. The result is given in per mil (‰) because naturally occurring variations are typically on the order of parts per thousand.

Previous studies have demonstrated the stable isotopes of CO and concentration can be applied to constrain the relative source strengths of CO (e.g., Stevens and Krout, 1972; Stevens and Wagner, 1989; Brenninkmeijer, 1993; Mak et al., 1998; Bergamaschi et al., 2000 and Wang et al., 2010). This can be achieved because particular CO sources have unique isotopic signatures as shown in figure 2.2 and table 2.1. For example, $C^{18}O$ can be used to distinguish between combustion derived CO sources and non-combustion sources such as CO from

non-methane hydrocarbon oxidation because of the relative enrichment of combustion sources compared to NMHCs (figure 2.2). In addition, ^{13}CO is a suitable tracer for separating methane derived CO from other sources. This stems from the observation that methane derived CO is isotopically depleted compared to other CO sources (figure 2.2).

Table 2.1: Isotopic signatures of CO sources

Source	$\delta^{13}C$ ‰	$\delta^{18}O$ ‰
Fossil fuel combustion	-27.5[a]	23 to 26[b]
Biomass Burning	-12[c] to -25[d]	18[b]
Methane Oxidation	-52.6[e]	0[f]
NMHC Oxidation	-32.2[b]	0[f]
Biogenic	-12 to -25[g]	0[h]
Ocean	-25[i], -40[j]	15[j]

[a]Stevens et al. 1972; [b]Stevens and Wagner 1989; [c]for C4 plants (Manning et al., 1997); [d]for C4 plants (Manning et al., 1997); [e]Value based on the $\delta^{13}C_{CH4}$ (− 47.2 ‰ (Quay et al. 1991)), and the fractionation in CH_4 + OH (5.4 ‰)(Saueressig et al., 2001); [f]Brenninkmeijer and Röckmann 1997; [g]Assign δ value based on assumption that biogenic emission is the same as that in plants (L.K. Emmons, personal communication, 2016); [h]Assume the same as oxidation source (Park et al., 2015); [i]Goericke and Fry, 1994; [j] Nakagawa et al., 2004.

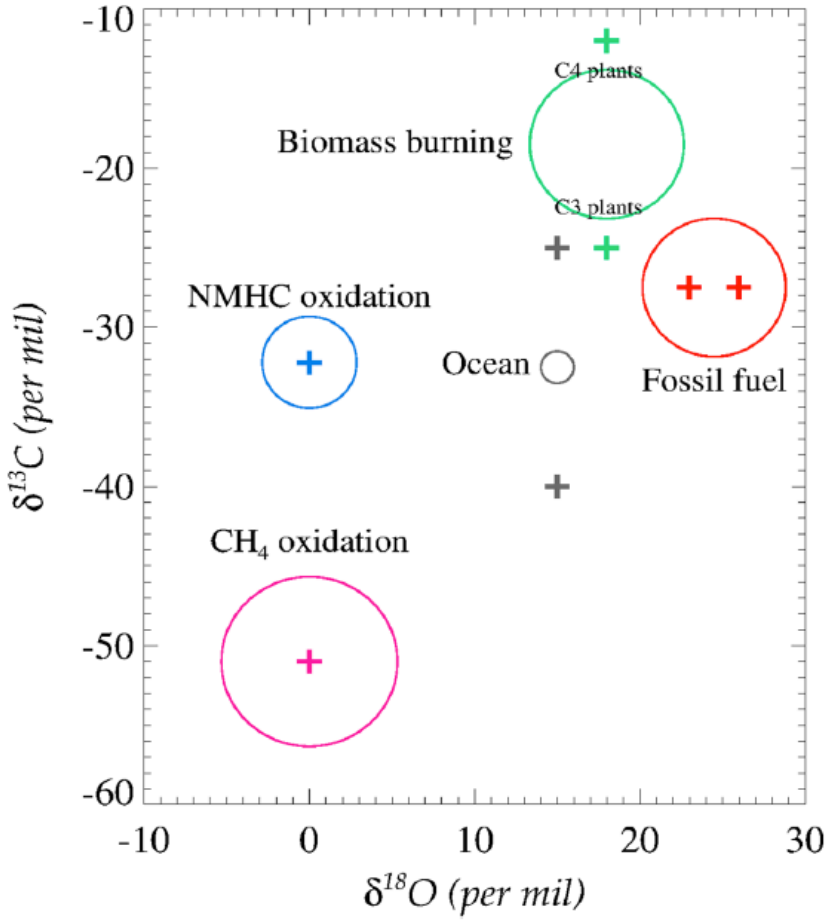

Figure 2.2: The stable isotopic signature of the major sources of CO based on data from Table 2.1. The size of each circle is proportional to the magnitude of its source according to data from IPPC (2001).

2.2.1 Methane oxidation

Prior to the industrial revolution, fossil fuel-derived CO is non-existent, thus the main sources of CO are methane oxidation, NMHC oxidation and biomass burning. Other sources of CO include direct biogenic emissions and direct emission by the breakdown of DOC from the ocean, however their contribution is

at most a few percent of the total (Wang et al., 2010, Park et al., 2015). Methane-derived CO is the largest source and is due to atmospheric oxidation of CH_4 by OH radical. Methane and $\delta^{13}C_{CH4}$ have been well characterized by direct measurement in Antarctic ice (e.g., Mitchell et al., 2013; Sowers et al., 2010, Ferretti et al., 2005; Spahni et al., 2005; Chappellaz et al., 1997; Mischler et al., 2009). The ^{13}C and ^{18}O kinetic isotope effects for the reactions CH_4+OH and CO+OH have also been measured (Cantrell et al., 1990; Stevens and Wagner, 1989), and are included in the data analysis. $\delta^{13}C_{CH4\text{-}CO}$ ~52‰, including a kinetic fractionation of about 5‰ during the CH_4+OH reaction which is based on an average $\delta^{13}CH_4$ of ~-47‰ in the SH (Lowe et al., 1991; Lowe et al., 1997; Mak et al., 2000; Quay et al., 1999) and the assumption that after the formation of CH_3 radicals no further fractionation takes place (Brenninkmeijer, 1999). Direct emissions from the terrestrial and marine biosphere have been both measured and modeled, and are estimated to be very small, particularly in Antarctica (Park, 2010, Park et al., 2015). Because the methane-derived CO is precisely calculated from observations of CH_4, we treat that source function as known. Since there is no fossil fuel-derived CO prior to the 18th century, the remaining unconstrained major source terms in the paleo CO budget are therefore NMHC oxidation by OH radicals and biomass burning (figure 2.3) and are discussed below.

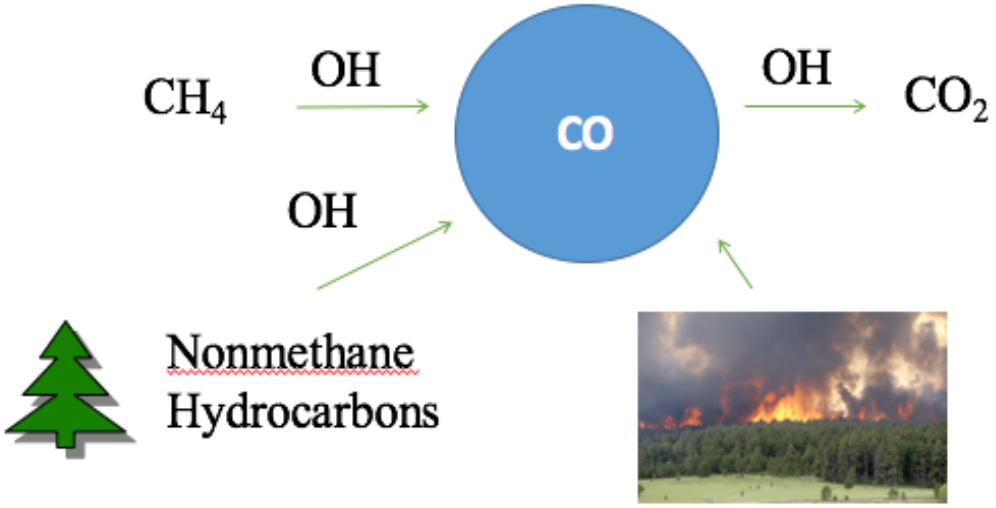

Figure 2.3: The interrelationship among CO, CH_4, and OH. The mean abundance of OH radical is largely determined by the abundance of CO and CH_4, because these two gases are the largest sink for OH.

2.2.2 Non-methane hydrocarbons

Atmospheric oxidation of nonmethane hydrocarbons (NMHCs) to CO via OH (and to a much lesser extent O_3) is one of the major sources of atmospheric CO. Direct emission from vegetation makes up approximately 90% of the NMHC inventory, with isoprene being the dominant species both from a flux and reactivity perspective (Guenther et al., 2008; Bergamaschi et al., 2000; Duncan et al., 2007; Park et al., 2015). Model estimates show that oxidation of isoprene contributes ~331 Tg CO yr^{-1} which represents 15-25% of the total CO emission as shown in figure 1.1 (Pfister et al., 2008). $\delta^{13}C$ of CO from NMHC oxidation has been characterized and is estimated to be -32‰ taking in to account a KIE of

6.94‰ for isoprene + OH (Rudolph et al., 2003). $\delta^{18}O$ of CO from the oxidation of NMHC and methane has not been directly quantified, and its characterization is largely based on indirect observations. One study using southern hemisphere atmospheric observations estimated $\delta^{18}O$ of CO from the oxidation of NMHC and methane to be ~0‰ (Brenninkmeijer and Röckmann, 1997). Another study reports a relatively enriched $\delta^{18}O$ of CO from NMHC oxidation with a delta value of 14.9‰ which was derived from air samples originating in rural Illinois (Stevens and Wagner, 1989). This value has a large uncertainty associated with it due to the possible oxygen exchange between water vapor and the many intermediates in the NMHC and methane oxidation reaction chains (Stevens, 1993). Almost all of the published papers since 1989 have used an isotopic signature of 0‰ for ^{18}O from hydrocarbon oxidation (Brenninkmeijer and Röckmann, 1997; Mak et al., 1998, Mak et al., 2000, Wang et al., 2010 and Park et al., 2015). This is largely because the observations from the Southern Hemisphere and subsequent modeling studies indicate that this is the value of the background source of CO due to hydrocarbon oxidation. However, it is acknowledged here that the oxygen isotopic signature of hydrocarbon-derived CO has never been successfully measured (J. Mak, personal communication, 2016). Furthermore, if one looks at the oxidation mechanism for CH_4, for example, there is no obvious physical reason as to why the oxygen isotopic signature of methane-derived CO should in fact be 0‰. However, this is the value that represents the

current state of knowledge and since it is an assigned value, a meaningful uncertainty onto this isotopic signature cannot be given.

2.2.3 Biomass burning

Over time, naturally occurring fire and human activity are the primary causes of variations in biomass burning. Biomass burning includes all the different types of vegetation that can be burned (e.g., grasslands, savannas, forests). The isotopic composition of CO from biomass burning is close to the isotopic composition of the actual biomass burned (Stevens and Engelkemeir, 1988). For example, C3 plants have $\delta^{13}C$ of -23.5‰ while the $\delta^{13}C$ of C3 plants burned is around -25‰ (Farquhar, 1993 and Manning et al., 1997). Furthermore, C4 plants have $\delta^{13}C$ of -15‰ while the $\delta^{13}C$ of C4 plants burned is around -12‰ (Ehleringer, 1993, Manning et al., 1997). The $\delta^{18}O$ value for biomass burning–derived CO is generally between 15 and 22‰, depending on specific combustion conditions (Brenninkmeijer 1993; Steven and Wagner, 1989; Kato et. al, 1999). $\delta^{18}O$ of CO from biomass burning was reported as 18±1‰ in Stevens and Wagner (1989) while Bergamaschi (1998) estimated it to be 10±1‰ based on the measurements of Siberian plumes. Laboratory chamber experiments have also been carried out to investigate the isotopic signatures associated with biomass burning and indicate a very large range. For example, the reported range for $\delta^{13}C$ is -33.8‰ to -10.2‰ and $\delta^{18}O$ is 3.0‰ to 26.0‰ which represents the burning of different plants (e.g.

C3 or C4) and different burning stages (e.g. flaming or smoldering) (Kato et al., 1999). It is reported that $\delta^{18}O$ is strongly linked to combustion temperature (Brenninkmeijer and Röckmann, 1997). Unlike high temperature internal combustion where no fractionation takes place, biomass burning has highest CO emissions during the relatively low temperature smoldering phase and fractionation occurs because of the isotopic exchange involving C, CO, CO_2 and H_2O (Lobert et al., 1992) which causes a range in $\delta^{18}O$. The lower limit of ~3‰ for $\delta^{18}O$ of CO from biomass burning can be explained by a continuous relative depletion that occurs during transport to the extra tropical SH (Brenninkmeijer and Röckmann, 1997). The strongest depletion of CO from biomass burning is expected to happen in the tropics because that is where CO has the shortest lifetime (Brenninkmeijer and Röckmann,1997). Because of the unique signatures in both ^{13}C and ^{18}O (figure 2.2), stable isotopes of CO can help resolve the relative abundance of the two unknown sources in the paleo CO budget – NMHC oxidation and biomass burning. This has been demonstrated in Antarctic ice cores (Wang et al., 2010). However, from a global perspective, on average, $C^{18}O$ from combustion-derived sources is significantly enriched compared to $C^{18}O$ from hydrocarbon-derived CO (Brenninkmeijer 1993; Brenninkmeijer and Röckmann, 1997; Bergamaschi et al., 2000; Mak et al., 1998) and, on average, ^{13}C from biomass burning is enriched compared to ^{13}C derived from NMHC oxidation (although there is significant variation in $\delta^{13}C$ that will depend upon fuel type,

combustion temperature, and/or origin). Largely the isotopic signature that is assigned to the different sources is firstly derived from observations, because they have to agree with the observations, then uncertainty analyses in the source signatures is performed (Park et al., (2015) and others), resulting in the best guess. We are confident in the isotopic signatures (figure 2.2) because it is based on interpretation of observation records, plus extensive uncertainty analyses (Park et al., 2015).

2.2.4 Fossil fuel combustion

For modern samples (post industrial revolution), fossil fuel combustion must be considered. ^{13}C from fossil fuel burning has a reported value of -27.5 ‰ (Stevens and Wagner, 1989; Stevens et al., 1972). Gasoline vehicles have a $\delta^{18}O$ of CO of 25.3±2.0 ‰ measured directly from the exhaust of automobiles whereas diesel vehicles exhibit a relative depletion of 15.1±1.0‰ (Tsunogai et al., 2003). CO from fossil fuel burning is the most enriched of all the sources with an average $\delta^{18}O$ value of +23 to +26 ‰ (Brenninkmeijer and Röckmann, 1997; Stevens and Wagner, 1989). $\delta^{18}O$ from atmospheric CO is depleted (-8‰ - +8‰) relative to fossil fuel burning while $\delta^{18}O$ of atmospheric oxygen (+23.5‰) is similar to fossil fuel burning (Bergamaschi et al., 2000b). The reason that internal combustion results in ^{18}O values close to the value of atmospheric oxygen is because during high temperature combustion, little to no fractionation occurs since at high

temperatures the ground state energy level of the different isotopologues and the vibrational energy are closer to each other (Brenninkmeijer and Röckmann, 1997).

2.2.5 Biogenic and oceanic emissions

Direct CO emission from leaf matter, both living and dead, constitutes the biogenic source. The contribution from this source is small and not well quantified (Bergamaschi et al., 2000; Duncan et al., 1997, Park et al., 2015). The IPCC 2001 report estimates the direct CO emission from plants to be ~2-3% of the total budget. A more recent modeling study by Park et al. (2015) estimates the contribution from CO emission from plants to be 3-4%. The direct emission is likely from photooxidation or direct photodegradation of cellular material but the mechanism and factors controlling the emissions are poorly constrained (Tarr et al., 1995, Guenther et al., 2000). Also poorly constrained is the isotopic signature of this source. $\delta^{18}O$ of CO is reported as 0‰ (the same as methane and NMHC oxidation) and $\delta^{13}C$ is estimated to be -12‰ for C4 plants and -25‰ for C3 plants (Park et al., 2015, L.K. Emmons, personal communication, 2016). Another source of uncertainty is the direct emission of CO from the ocean. One of the only reported values are from measurements from the Pacific where the authors report -40‰ for $\delta^{13}C$ and 15‰ for $\delta^{18}O$ of CO, which takes into account fractionation during photochemical production and the isotopic ratios in dissolved organic

matter (Nakagawa et al., 2004). It should be noted that the estimated contribution from direct oceanic emission to the overall CO budget is less than 1% so its contribution is negligible and is often excluded in budgets (Bergamaschi et al., 2000, Park et al., 2015).

2.2.6 Variability in CO isotopic signatures

The isotopic composition of the isotopologues (figure 2.1) can be affected by variations in the relative source strengths of CO. The impact on isotopic signatures from varying sources of CO is summarized in Table 2.2. ^{13}CO is mostly affected by the variation in CH_4-derived CO, which is known. An enrichment in $C^{18}O$ is evident when combustion processes become more prevalent. Therefore, variations in biomass burning will mostly be reflected in variations in ^{18}O. Another important process that may affect the mean isotopic composition is a change in the magnitude of the primary loss mechanism (which is the reaction with the hydroxyl radical). Previous studies show that OH is stable in the modern atmosphere (Montzka et al., 2011; Lelieveld et al., 2006). Nonetheless, the rate of destruction of CO may be impacted due to substantial differences in OH over time. The KIE for $C^{18}O$+OH is unusual in that it has an inverse mass dependence so that a significant increase in OH would result in an enrichment in ^{13}CO and depletion in $C^{18}O$ (Cantrell et al., 1990; Steven and Wagner, 1989). The impact of varying OH concentration on CO is summarized in the last two rows of table 2.2.

Table 2.2: Predicted variations in observed [CO], ^{13}CO, and $C^{18}O$ under different scenarios (read left to right).

Biomass burning	VOC oxidation	CH_4 oxidation	[OH]	Change in $\delta^{13}C$	Change in $\delta^{18}O$	Change in [CO]
INC	DEC	DEC	Constant	Variable	INC	Variable
DEC	INC	DEC	Constant	Variable	DEC	Variable
Constant	Constant	Constant	INC	INC	DEC	DEC
Constant	Constant	Constant	DEC	DEC	INC	INC

The first three columns represent the main sources of CO in the preindustrial Southern Hemisphere. 'INC' or 'DEC' indicate an increase or decrease, respectively, in the relative strength of that source. Column 4 is seasonally averaged hemispheric OH concentration; Columns 5-7 show the expected change in the observed signal for the three isotopologues considered here.

In conclusion, for some isotopic signatures shown in table 2.2 a degree of uncertainty is associated with the measurements as discussed above. This uncertainty does not take away from the fact that the signatures are still useful for deducing a particular CO source because of the large isotopic differences. For example, $C^{18}O$ can be used to distinguish between combustion derived CO sources and non-combustion sources such as CO from non-methane hydrocarbon oxidation. In addition, ^{13}CO is a formidable tracer for separating methane derived CO from other sources because $\delta^{13}C$ is sensitive to the fractionation of methane oxidation. This stems from the observation that methane derived CO is isotopically depleted with a value of $\delta^{13}C_{CH4\text{-}CO} \approx -52‰$. Therefore, even with given uncertainty, application of isotopic signatures is useful to provide constraints on the distribution of the CO fluxes from the various sources.

2.3 Trapping gas in ice

The process of trapping gas in ice is complex and is primarily controlled by the weight of the accumulated overlying snow and temperature (Gow, 1968). The overall transformation of snow to ice begins with firn. Firn is a porous layer which can be described as an intermediate stage between snow and ice and is important because air can be extracted and analyzed from the firn to investigate the history of the atmosphere. Gas in the firn is in constant exchange with the overlying atmosphere making it younger in age than the ice that surrounds it. The exchange continues until the air gets trapped in the ice matrix at the firn/ice transition region. This happens once the density of firn reaches ~90% that of air-free ice and the interconnected air passages between grains are pinched off to form bubbles, trapping the enclosed gases from the surface (Herron and Langway, 1980). This process happens more quickly in higher accumulation environments because of the faster advection downward of firn layers. Depending on local climate, the trace gas history from firn will vary in resolution and length (Kaspers et al., 2004). Generally speaking, sites with high accumulation rates and low temperatures have the longest records (there are a few exceptions as noted by Severinghaus et al., 2010). It is important to understand the various physical processes occurring in the firn since those can change the isotopic ratios as well as the composition of the air before pore closure is reached (Bender, 2002; Schwander,1989; Severinghaus et al., 2001; Severinghaus and Battle, 2006,

discussed below). Even after the gas is fully enclosed in ice, the abundance of a gas can be altered by processes occurring during storage or in situ processes (Bender 2002, Haan and Raynaud, 1998, Fain et al., 2014). For example, oxidation processes of organic matter after pore closure can contribute to elevated CO levels in gas extracted from ice cores (Haan and Raynaud, 1998). It is therefore necessary to understand and quantify these processes because they can influence how the gas record obtained from ice cores is interpreted.

2.3.1 Bubble formation at WAIS Divide

Figure 2.4 demonstrates the process of snow-ice formation. The firn can be separated into three layers based on the gas transport mechanism that dominates at a given depth: The convective zone, the diffusive zone and the lock-in zone. The shallow upper layer of the firn is the convective zone and air is well mixed and homogenous with the surrounding atmosphere in this layer (Raynaud, et al., 1993). Gas movement in the convective zone is dominated by convection due to highly permeable firn and/or wind pumping. At WAIS Divide the convective zone layer is shallow and ranges in depth from ~1.5 to 5 m (figure 2.4 b). The range in depth occurs because there are several methods to estimate the depth of the convective zone and each method defines the thickness of the convective zone in a marginally different way (Battle et al., 2011). Below the convective zone is a thick layer where molecular diffusion dominates and the fractionation of gases is

likely to occur. The main transport mechanisms in this layer are mass dependent gravitational settling and thermal gradients (Severinghaus et al., 1998) (Figure 2.4 right). Gravitational fractionation, which is mass dependent, results in the gravitational settling of heavy components therefore enriching the bottom of the firn column with the heavier isotope (Sowers, et al., 1992). Thermal gradients can also cause fractionation resulting in the heavier components moving toward the colder layers of the firn. Below the diffusive column is a low permeability layer termed the lock-in zone (LIZ). There is little vertical movement within the lock-in zone however air can still be extracted for analysis. Below the LIZ the firn-ice transition occurs (close-off). The close-off depth is different at different locations due to variations in temperature and accumulation rate (the weight of the overlying accumulated snow) (Khalil, 1993). For example, the close-off depth of the firn at WAIS D is 76.6 m (figure 2.4 b), for the South Pole ice core it is 119 m and for Dome C it is 98.6 m (Battle et al., 2011; Kaspers, et al., 2004). The process of going from snow to firn to pore closure and bubble trapping can take a few hundred years at sites with high accumulation rates and/or cold temperatures (i.e. WAIS D or Summit, Greenland). Conversely, this process can take up to a few thousand years at sites with low accumulation rates (i.e. Vostok, Antarctica) and are much more affected by accumulation-rate changes over time (Sowers 1992).

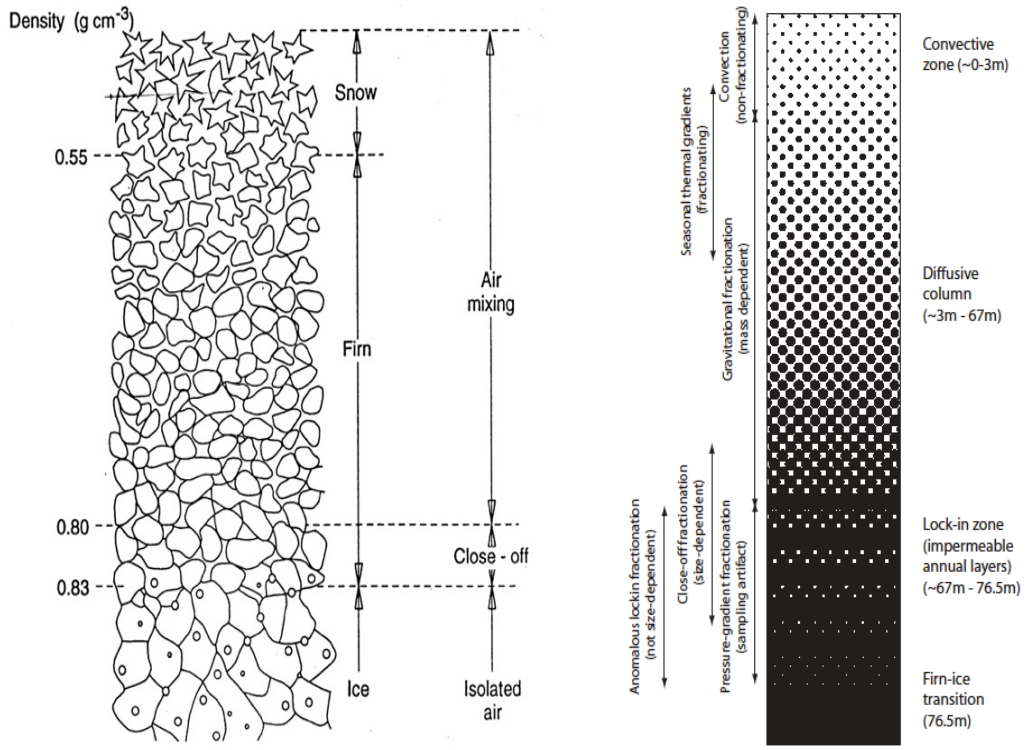

Figure 2.4: (a) Diagram of the snow-ice transformation illustrating the trapping process for air bubbles. The depth at which the pore close-off occurs is typically in the range of 50-130 m below the surface, depending on the site characteristics (temperature and accumulation rate). Adapted from Khalil, 1993. (b) A schematic diagram of regions in an idealized firn column, showing generic features (on the right) and the transport mechanisms expected to be significant in each region (on the left). Also shown (in parentheses on the right in b) are the approximate depths of the features for the ice at WAIS-D. The figure is not drawn to scale, and not all processes will be present in every naturally occurring firn column. Adapted from Battle et al. (2011).

2.3.2 Quantifying gravitational settling using nitrogen isotopes

Isotopic fractionation in the ice core samples is expected due to gravitational separation, however its magnitude can be estimated. Both $\delta^{13}C$ and $\delta^{18}O$ of CO

need to be corrected for gravitational effects at all sampling sites according to Sowers et al. (1992). Gravitational fractionation in the firn column is mass dependent meaning that the heavier isotopologues of CO are preferentially found at the bottom of the firn. The isotopes of nitrogen can be used to correct for gravitational fractionation because $\delta^{15}N$ of atmospheric N_2 has stayed constant, unlike the greenhouse gases CO_2 and CH_4, over the roughly 1 million year time scale spanned by the ice core record. Also, the mass difference between ^{13}CO and ^{12}CO is 1 amu and the enrichment with depth of ^{13}CO with respect to the ^{12}CO resulting from gravitational fractionation is the same as the gravitational enrichment of ^{15}N–^{14}N versus ^{14}N–^{14}N of N_2 because they exhibit the same mass difference. We therefore use the measured $\delta^{15}N$ of N_2 at the base of the firn (0.31‰ at 76 m) to correct for gravitational separation for all samples from WAIS Divide (Battle et al., 2011).

2.4 Dating ice cores

2.4.1 Smoothing

When looking at the different levels of firn, the air present is a mixture of air of different ages, due to the gas diffusion process and mixing with surface air as described above. Therefore, the longer the record, the larger the age spread (Trudinger et al., 1997), thereby limiting the time resolution with which past atmospheric histories can be reconstructed. Furthermore, diffusion in firn is also

known to smooth signals making it difficult to resolve smaller scale processes revealed in gas histories so only trends may be reconstructed (Witrant et al., 2012). Smoothing is also caused by the gradual bubble closure process that physically traps the air in bubbles at the base of the firn column (Mitchell et al., 2015). More specifically, the firn acts as a low-pass filter that attenuates high-frequency atmospheric signals such as the annual cycle of some trace gases (Buizert, 2013; Trudinger et al., 1997). For example, methane concentration measurements from Dome C samples indicated that firn smoothing was responsible for reducing the magnitude the signal from the abrupt 8.2 ka climate event by 34-59% (Spahni et al. 2003). Smoothing is directly related to the accumulation rate. The lower the accumulation rate the higher the degree of smoothing as well as a broader age distribution (Mischler et al., 2009; Mitchell et al., 2011, 2013; Marcott et al., 2014). Moreover, the broader the age distribution, the larger the smoothing is, thereby restricting the resolution of the atmospheric trend that can be reconstructed.

2.4.2 Ice age and gas age

Deducing the age of the gas is a rather difficult task because the gas in the firn is in constant exchange with the overlying atmosphere making it younger in age than the ice matrix that surrounds it. When assembling a timescale for ice cores the first step is to figure out the age of the ice itself and then assemble a gas age.

The ice age is calculated by various methods but most commonly it is calculated from counting annual snow layers. Going deeper into the ice, the layers of the ice core get older and thinner. For example, at WAIS D, the average layer thickness found at 40,000 years BP is ~1 cm compared to an average thickness of >15 cm at 0-2345 years BP (0-577 m) (Sigl et al., 2015). The layers are identified from measured variations in ice composition and impurity content (i.e. by identifying the chemical and physical difference between winter snow and summer snow). For example, WAIS D ice chronology was obtained for the upper 2800 m of the core by counting the annual layers observed in the dust and from the chemical and electrical conductivity records (Sigl et al., 2015) (figure 2.5 blue line). If layers are too thin to count, the ice can be dated by forward or inverse modeling. Reference horizons such as well dated volcanic eruptions can also be used to date the ice. Once the ice scale is determined the next step is to get the gas scale. For the gas scale, one must consider how the gas is transferred from the atmosphere to ice via diffusion and mixing in the firn column. Going deeper into the firn and reaching the close-off (firn-ice transition, figure 2.4), the entrapped gases (bubbles) show an age distribution which is later transferred deeper in the ice. From the age distribution a mean age can be calculated. The difference between the age of the ice and the age of the gas contained in this ice is called Δ age. Δ age will vary by site and is inversely proportional to accumulation rate. Generally speaking, the higher the accumulation rate, the smaller the difference between the

ice-age and Δ age. WAIS Divide (79.48° S, 112.11° W) Antarctica has a relatively high accumulation rate of 22 cm ice eq. yr^1. Accumulation rate for WAIS Divide is based on the combination of ion chemistry data (top 70 m of the core) and continuous electrical conductivity and di-electric property (ECM/DEP) measurements from 70 m down to 298 m in the core (Mischler et al., 2009). The WAIS D accumulation rate gives a Δ age of approximately 200 years for the top 2100 m of the core (figure 2.5). Δ age is approximated using the firn-densification model (Marcot et al., 2014).

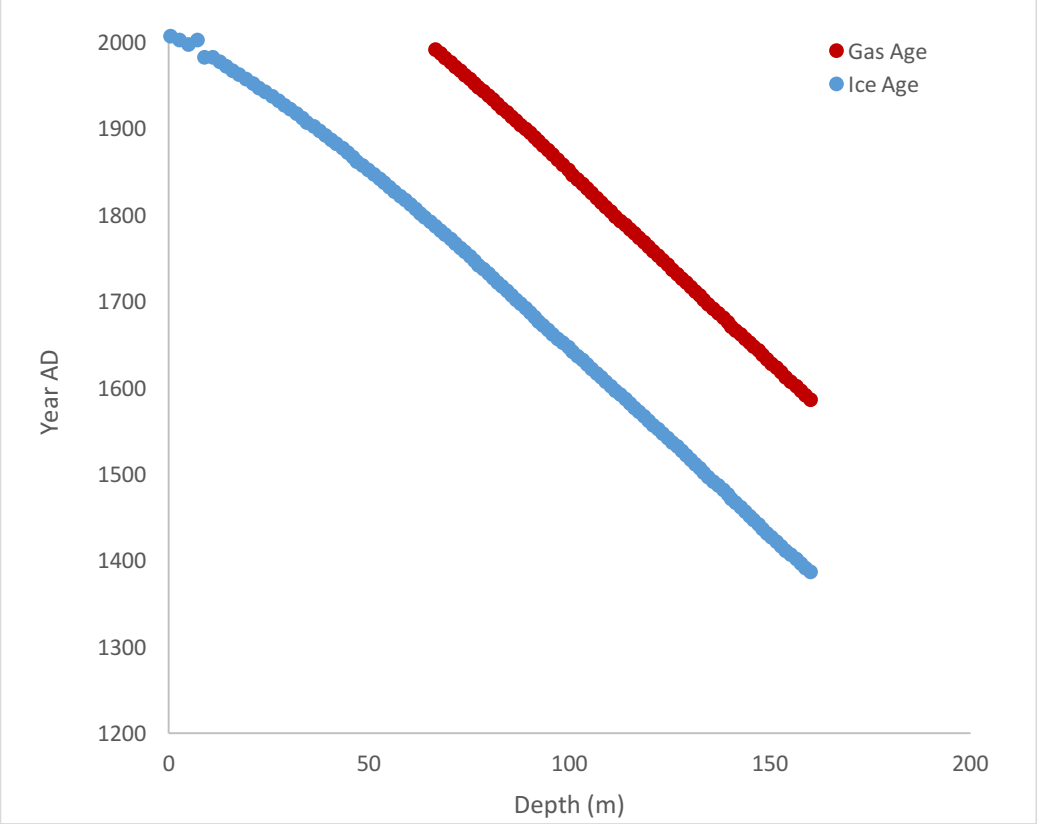

Figure 2.5: Timescale for WAIS Divide. Blue line is the age of the ice while the red line indicates calculated gas age. The difference between the lines is the Δ age which is approximated by firn densification models.

2.5 Sample site characteristics

Samples for this study come from an ice core that was drilled at WAIS

Divide in Antarctica (figure 2.6). The site characteristics can be seen in table 2.3.

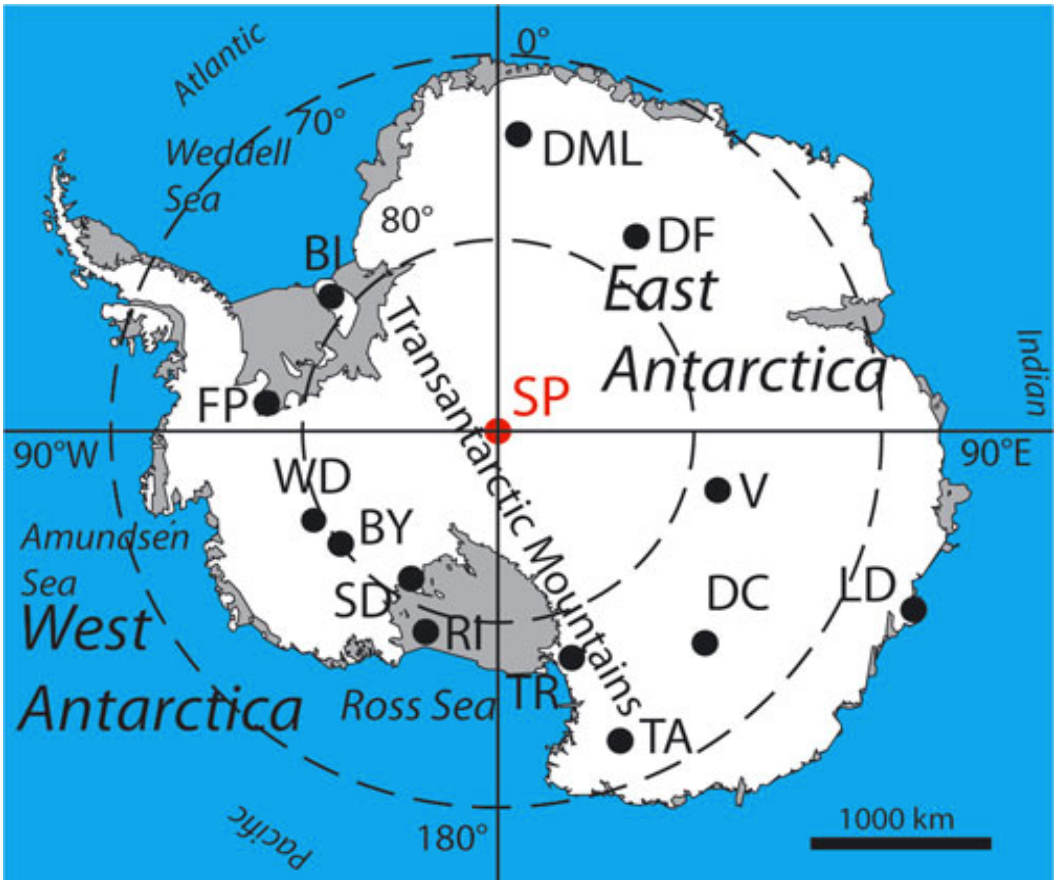

Figure 2.6: Map of Antarctica with deep ice-core locations labeled: South Pole (SP), Berkner Island (BI), Byrd (BY), EPICA Dome C (DC), Dome Fuji (DF), Dronning Maud Land (DML),Fletcher Promontory (FP), Law Dome (LD), Roosevelt Island (RI), Siple Dome A (SD), Talos Dome (TA), Taylor Dome (TR), Vostok(V), WAIS Divide (WD). Adapted from Casey et al., 2014.

Table 2.3: WAIS Divide site characteristics

Latitude-Longitude	79.28° S, 112.05° W
Elevation[a]	1,766
Mean Annual Temperature[b]	-31
Accumulation Rate[c]	22.2
Date Drilled	2006

[a]meters above sea level (m.a.s.l); [b]degrees Celsius; [c]ice equivalent per year

2.5.1 The West Antarctic Ice Sheet (WAIS Divide)

The ice core drilled at the WAIS Divide (WAIS-D) was an NSF funded US ice coring effort. A final depth of 3405 m was reached in 2011 yielding a 68,000-year-old climate record. Samples used in this study were drilled from borehole WDC06B in 2006. This borehole was drilled to a depth of 130 m and its core diameter is 10 cm. WAIS Divide is located at 79°28.048' S, 112°05.160' W (elevation m.a.s.l 1,766 m, mean annual temperature −31.0 °C) and is an ideal location for trace gas studies because of its high accumulation rate. Due its high accumulation rate of 22.2 ice equivalent per year, this site provides climatic records with unparalleled temporal resolution for the Southern Hemisphere. The core drilled also allows for trace gas analyses that are only marginally affected by diffusive smoothing throughout the firn column due to the high accumulation rate (Mischler et al., 2009; Mitchell et al., 2011, 2013; Marcott et al., 2014), as discussed in section 2.3. The high accumulation rate at WAIS D is also

responsible for the relatively small difference between the ice-age and gas-age (Δ age). Δ age is on the order of 205 years and can be considered constant throughout the 130 m core because the annual layer thickness obtained from the ECM/DEP counts show the accumulation rate at WAIS D remained constant over the last 1,000 years. The gas age versus depth scale was compiled by subtracting 205 years from the ice age at every dated depth below the lock-in-zone. The uncertainty with WAIS D chronology is ± 5%.

3 Experimental methods

3.1 Principles of cryogenic vacuum extraction

A new and improved version of a trace gas cryogenic vacuum extraction system based on the work by Wang and Mak (2010) was developed and utilized to extract CO from ice cores as shown in figure. 3.1. The principles behind this technique have been discussed in detail previously where Wang et al. (2010) describe an online gas extraction method (extraction line connected to mass spectrometer) and others an offline method (Brenninkmeijer (1993), Steven and Krout (1972)). In short, the isotopic composition of CO cannot be measured directly with sufficient sensitivity and accuracy. Application of a cryogenic vacuum extraction allows for the chemical oxidation of CO to CO_2 while other trace gases such as water vapor, CO_2, N_2O and other condensable species are cryogenically trapped and thus removed (Brenninkmeijer, 1993). These species are removed due to condensation at liquid nitrogen temperature. It is crucial that all atmospheric CO_2 and water vapor is removed prior to the oxidation process because atmospheric CO_2 would interfere with the determination of the CO_2 derived from CO. Furthermore, water vapor would hydrolyze the Schütze reagent that acts as a catalyzing agent to oxidize CO to CO_2. For this reason, a water trap as well as two clean-up traps are installed.

3.2 Instrumentation and general procedure

A schematic diagram of the extraction line for carbon and oxygen isotope analysis is shown in the figure 3.1. The cryogenic vacuum extraction system is made of ¼" OD glass tubing and is comprised of cryogenic purification (or cleanup) traps, used to condense out volatile species, a chemical reagent that selectively oxidizes CO to CO_2 (Schütze, 1949; Smiley, 1965), and a cryogenic collection trap for the CO-derived CO_2. All cryogenic traps are immersed in liquid nitrogen, which is cold enough to condense out all volatile trace gases such as water vapor, CO_2, volatile organic compounds (except for methane), N_2O, etc. The stable diatomic gases N_2 and O_2 are not condensed out at the relatively low pressure of the extraction line (~100 hPa). The extraction system is attached to a high-flow-low-flow system that 'cryo-focuses' the sample into a much smaller volume and then transfers and loads the sample cryogenically onto the gas chromatograph column. From there, the sample is injected into the IRMS (see end of section).

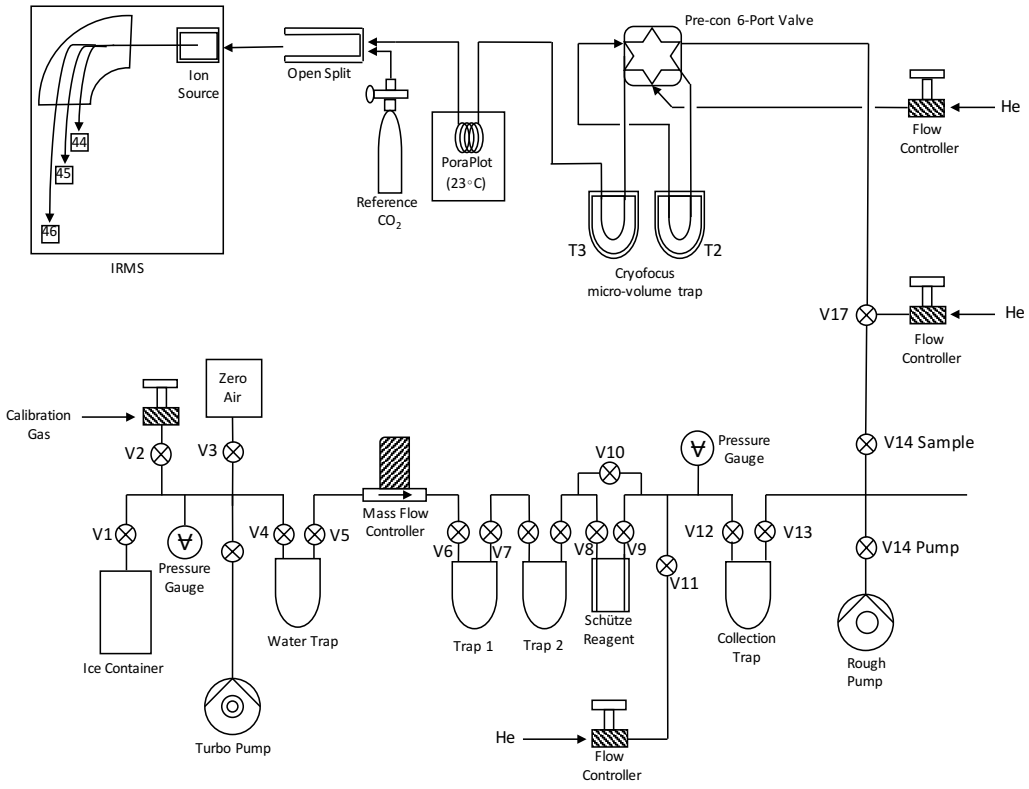

Figure 3.1: Schematic of the system used for CO concentration, $\delta^{13}C$ and $\delta^{18}O$ analysis of ice cores.

On the front end of the extraction line is an MKS mass flow controller (MFC) that controls the flow rate of the sample into the lower pressure part of the line. Upstream of the MFC is a gas manifold line that can introduce CO-free air (zero air) generated from a platinum furnace, calibration gas, or sample air that is derived from ice. A number of procedures was used to determine the efficiency of the line. Below I discuss the calibration gas and CO-free gas analyses to characterize the system's performance. Calibration gas analysis is central to all

analyses and involves the analysis of air with a known CO concentration and isotopic signature. The extraction line uses three different CO calibration gases. However, the working standard is a cylinder of air that was measured and certified by the National Oceanic and Atmospheric Administration/Climate Monitoring and Diagnostics Laboratory (NOAA CMDL). This working standard has a NOAA certified concentration of 85.9 ppbv CO in air. This allows us to trace back reported concentration to an established scale. Calibration gas is attached to the line via valve V2. The calibration gas passes through the water trap and through the MFC at a flow rate of 49.5 mL/min (STP) followed by passing through trap 1 and trap 2. Pressure of the extraction line on the downstream side of the MFC is kept at about 100 hPa by differential pumping, in order to prevent O_2 from condensing (liquefied O_2 is explosive upon warmup). Atmospheric CO_2, H_2O, N_2O, and other volatile species are trapped in the cleanup traps 1 and 2 (Trap 1, Trap 2 figure 3.1) (Brenninkmeijer, 1993). The purified CO is selectively and quantitatively oxidized to CO_2 by acidified I_2O_5 on a silica gel support (Schütze reagent) (Schütze, 1965; Smiley, 1949). This is an addition reaction (CO+O) which results in the retention of the original ^{18}O abundance of CO (Stevens and Krout, 1972). The Schütze reagent used was prepared previously and based on the original procedure (Smiley,1949). A bypass valve (V10) is installed for the Schütze reactor tube so that the breakthrough of CO_2 through multi-loop trap 1 and 2 can be evaluated. The bypass also allows continuous back-

flushing of the system with ultrapure helium between sampling days. The CO-derived CO_2 is collected in the collection trap and is then eluted with cryogenically purified ultrapure helium and cryogenically focused in a micro-volume trap. The micro-volume trap is then heated to room temperature and the CO-derived CO_2 is loaded onto a GC column (15 m x 0.25 mm Poraplot Q). The column separates from the CO_2 any trace amounts of N_2O (which is very small but detectable). Sample CO_2 exits the column via an open split into the isotope ratio mass spectrometer (see below).

Because of the small volume of sample extracted, continuous-flow isotope ratio mass spectrometry (CF-IRMS) is required for analysis. CF-IRMS has been used successfully in previous studies to measure small volumes of trace gases including atmospheric CH_4 (Rice et al., 2001; Merritt et al., 1995; Lowe et al., 1991), atmospheric N_2O (Röckmann et al., 2003) as well as volatile organic compounds (VOC) in ambient air (Rudolph et al., 1997). Mak and Yang (1998) were the first to report the use of CF-IRMS for CO isotope analysis. The analysis with CF-IRMS is based in electron impact ionization (ion source in figure 3.1) followed by acceleration and subsequent monitoring of the relative abundances of masses 44, 45, and 46 of CO-derived CO_2. The sample size needed for analysis is mostly determined by the minimum operating pressure to generate a current at the collector end which varies with mass spectrometer design (Merritt and Hayes, 1994). The CF-IRMS used in this study was a Thermo Scientific MAT 253

Isotope Ratio Mass Spectrometer and the minimum sample size is ~2-4 nmole of CO_2 to provide measurements with the accepted precision for $\delta^{13}C$ ($\pm 1\sigma$ =0.4‰) and $\delta^{18}O$ ($\pm 1\sigma$ = 0.6‰) (Mak and Brenninkmeijer, 1994; Mak and Yang, 1998). This instrument is five times more sensitive than the CF-IRMS that was used in previous work (e.g. Wang and Mak, 2010, Wang et al., 2010).

To calculate $\delta^{13}C$ and $\delta^{18}O$ of CO we use the two observable ion-current ratios 45/44 and 46/44 which is carried out by the Thermo Scientific software ISODAT 3.0. This software corrects for the ^{17}O abundance, which is required for ^{13}C analysis (^{17}O contributes to mass 45). This correction algorithm has 3 components: i) abundance of the ^{17}O-bearing molecules with mass 45 is calculated from an assumed mass dependent relationship between the ^{17}O and ^{18}O isotopic abundances; ii) $^{13}C/^{12}C$ isotope ratio is calculated by correcting the raw isotope ratio 45/44 for the participation of ^{17}O-bearing molecules, and iii) the ^{18}O abundance is determined by correcting the raw isotopic ratio 46/44 for the participation of ^{17}O-bearing molecules and based on the calculated $^{13}C/^{12}C$ isotope ratios (Assonov and Brenninkmeijer, 2003; Santrock et al., 1985). $\delta^{13}C$ of the original CO is determined by the $\delta^{13}C$ of derived CO_2, whereas $\delta^{18}O$ is determined based on calibration gas with blanks subtracted out (Brenninkmeijer, 1993). To calculate the concentration of CO in the ice sample the ratio of peak areas between a sample and a calibration gas is evaluated.

3.2.1 Schütze blank sampling procedure

As mentioned above, the Schütze reagent selectively and quantitatively converts CO to CO_2 at room temperature, while preserving the original oxygen isotopic ratio of the CO and no isotopic exchange happens with the I_2O_5 (Schütze, 1949; Smiley, 1965; Stevens and Krout 1972). An alternative method to convert CO to CO_2 is to use CuO at 450ºC as the oxidizing agent instead of Schütze reagent. This method is not suitable for our studies because this oxidation process destroys the oxygen isotopic composition of CO (Stevens and Krout, 1972). There is a background signal associated with the Schütze reagent that is likely due to impurities and/or diffusion of air across the o-rings located in the Schütze reagent vessel. To quantify the Schütze blank signal, a flow of zero air devoid of any CO was processed through the reagent. This CO free air is generated by passing ambient air through a platinum catalyst heated to 200 ºC followed by a molecular sieve trap to remove the remaining CO_2, H_2O, N_2O and non-methane hydrocarbons (Mak, 1992). Net sample signal is obtained by subtraction of the Schütze blank. Corresponding blank corrections for the C and O isotopes are also determined. To determine the blank, CO-free air is flowed through the extraction line at 49.5 mL/min (identical to the calibration gas procedure). The bypass valve (V10) is flushed with zero air for 1 minute before the Schütze reagent vessel (via valves V8 and V9) is opened and bypass closed. A sample is collected for 2-3 minutes (the typical collection time), however many tests at other collection times

were performed in order to quantify the variation of the Schütze blank. After collection, mass flow controller (MFC), Schütze and pump valves (V14) are closed. Since the MFC is a controller and not a valve we isolate the line closing the bypass and Schütze. A helium flow (UHP He with a liquid N_2 cooled cleanup trap for purity) is then introduced (via valve V11), until the pressure reaches about 1100 hPa. Once the pressure is above 1100 hPa, the sample is cryogenically transferred to the micro-volume trap, T2. A computer program is used to control this cyro-focusing procedure. Thirty seconds after starting the program, trap T2 is automatically immersed into a dewar filled with liquid nitrogen. Once T2 is cooled, the collection trap is warmed to -70°C by immersing it in a dewar filled with alcohol that was cooled to -70°C with liquid nitrogen. The sublimated CO_2 is then carried by the helium flow into trap T2 where it is once again cryogenically trapped. After 4 minutes the entire sample is transferred. Then trap T3 is immersed into the liquid N_2 bath and T2 is warmed up and the sample is cryogenically transferred in to trap T3. The reason for doing this, is to transfer the sample into successively smaller volumes so that the sample can be loaded onto a capillary column. The volume of trap T2 is about 500 µl, whereas the volume of trap T3 is less than 10 µl. After transfer into trap T3, that trap T3 is warmed by taking it out of the liquid nitrogen and the sample is sent to the capillary column for trace gas separation. In order to switch between traps T2 and T3, a two-way 6 port valve is used.

3.2.2 Bubble-free water procedure

High purity, bubble-free water is needed to process an ice sample. It is used to fill the residual volume in the ice container, increasing the gas sample pressure for a more efficient transfer into the extraction line. The sample transfer rate is determined in most cases by the MFC setting and pumping speed, however for very small samples at low fore pressure (e.g., for all ice core samples), the flow rate would be too low. Increasing the pressure of the sample upstream of the MFC is an important step in providing a sufficient transfer rate and therefore a short sample collection time, thus minimizing any system blank (which is largely time dependent).

The following procedure is carried out to make the bubble free water needed to process an ice sample: Thoroughly wash the container with detergent, rinse the glass container (1.4 L, 105 mm OD) three times with deionized (DI) water and dry the groove with a kim-wipe paper. Fill the container to the top with Milli-Q water. Place a viton o-ring (120 mm OD) in the groove of the container. Make sure the o-ring and the groove is dry and clean. Attach a piece of 1/8" stainless steel tubing to the arm of the container. Place the container on the hotplate and insert the 1/8" into a glass beaker with DI water (~250 mL). Open the valve on the container to vent and leave it open during heating. Turn on the hot plate to highest heating level. After 10 min of heating some gas bubbles should come out of the vent tube of the container. If it is not, it probably means

that the valve is closed or that the heating unit is set too low. In this case, the container is heated for for ~40 minutes and the water inside should start boiling (strong steam will vent). Keep the water boiling for another 30 minutes. Wearing an oven mitt, the valve is closed and the container remove from the heat. Afterwards the tubing is removed and the inlet is covered with aluminum foil. Subsequently the container is cooled by running it under cold water for ~ 10 minutes. Once cooled, the container is prepared for connection to the ice container by blowing out the stems on the container with nitrogen to remove any residual water and fasten the PEEK tubing (Alltech) to the bottom stem

3.2.3 Ice core sampling procedure

Once the bubble-free water container is prepared and hooked up to the system, the ice process can commence. 30 cm ice core samples (~1kg) are cut in a deep freezer (-20°C) in to two ~15 cm pieces (for WAIS-D samples) and are weighed. The samples are then scraped with a stainless steel medical grade disposable scalpel (Miltex #22) to clean the surface. Approximately 2-3 mm of ice is removed from all surfaces of the core during this process and weighed again. The weight of the ice is reduced by about 10% from the shaving process. The sample is then placed in a custom built borosilicate glass container (1.5 L) (110 mm OD) with a glass flange (165 mm OD), Viton o-ring (150 mm OD) and external horseshoe clamp. The container is then submerged in an alcohol cooling bath held

at -30 °C. The container is attached to the extraction line by ½" stainless steel (SS) flexible tubing on the bottom arm. The upper arm has PEEK tubing connecting it to a glass container filled with bubble free water (see procedure in 3.2.2). Once securely connected, the sample is evacuated with a rotary vane pump and turbo-molecular drag pump for five minutes. Subsequently the sample is flushed five times with CO-free air. After flushing the sample is evacuated again, and then flushed three times with the working gas standard. The ice container is filled to ~1050 hPa with calibration gas and valve V2, the regulator and tank are closed isolating it from the line. Now the system is ready for processing calibration gas on ice. This procedure is repeated several times for each sample, resulting in average errors of $\Delta\delta^{13}C=\pm 0.4‰$ and $\Delta\delta^{18}O=\pm 0.5‰$).

After the calibration tests are complete, the ice container is evacuated and flushed with zero air three times and then evacuated with the turbo pump for 20 minutes. After pumping, the ice container is isolated and immersed in a hot water bath to melt the ice core sample. During melting, two Schütze blank runs are processed. Once the ice is finished melting, the ice container is opened, allowing the gas from the sample to expand into the extraction line. Because the sample is small, and much of the sample is still in the ice container, bubble free high purity water is allowed to flow into the ice container, which displaces the air sample, and allows us to process more than 90% of the sample. At this point the gas sample is collected as described in earlier sections.

3.3 Diagnostic Experiments

3.3.1 System blanks

System blanks are used to determine the background of the analytical system. There are two types: the 'bypass blank', which is the blank from the vacuum line, and the 'Schütze blank', which is the background from the vacuum line as well as the Schütze reagent.

Bypass blanks are performed on the extraction line to test the breakthrough of CO_2 through multi-loop trap 1 and 2 by bypassing the Schütze reagent (by closing valves V8 and V9) while flowing zero air through the bypass (open valve V10) and being processed according to the procedure outlined in Section 3.2. This test is the first one done on the system in order to confirm the efficiency of the extraction line. More specifically, this blank reveals how well the clean-up traps are working and the presence of leaks. Periodic tests are done where the collection time of zero air is increased from 2 minutes to 9 minutes which allows for the quantification of the gas collection efficiency of the traps. Flow rate tests are also performed to test for leaks. Leak rates are function of absolute pressure in the line. A pressure differential exists between the lab and the line, which is ~800-900 hPa (ambient pressure - line pressure). We double the flow rate from ~40 mL/min to 80 mL/min while keeping internal system pressure the same by increasing the pumping speed and therefore maintain a constant

pressure differential to test for leaks. This allows us to process twice as much sample in the same time period. When we do this we see little change in peak height so that indicates there are no detectable leaks in the system. CO concentration from the bypass blank is 3.4 (± 0.26) ppb (see Table 3.1). Table 3.1 shows selected bypass blanks from 2014. Over the course of processing ice cores hundreds of bypass blanks were measured.

Table 3.1: Selected bypass blanks from 2014

Date	Peak Height (mV)	Peak Area (Volt-secs)	Sample time (s)	Volume (mL)	[CO] ppb
13-3-14	40	0.111	180	120	3.37
13-3-14	40	0.11	180	120	3.37
13-3-14	41	0.115	180	120	3.49
13-3-14	38	0.109	180	120	3.31
13-3-14	38	0.11	180	120	3.34
13-3-14	40	0.111	180	120	3.37
13-3-14	40	0.117	180	120	3.55
17-3-14	37	0.107	180	129	3.02
17-3-14	33	0.098	180	129	2.77
18-3-14	38	0.107	180	132	2.95
18-3-14	35	0.101	180	132	2.79
18-3-14	35	0.098	180	132	2.70
18-3-14	35	0.098	180	132	2.70
19-3-14	37	0.095	180	125.4	2.76
19-3-14	35	0.097	180	125.4	2.82
19-3-14	35	0.097	180	125.4	2.82
20-3-14	36	0.1	180	124.2	2.93
20-3-14	36	0.095	180	124.2	2.78
20-3-14	36	0.097	180	124.2	2.84
21-3-14	36	0.097	180	123	2.87
21-3-14	33	0.094	180	123	2.78
25-3-14	37	0.102	180	123	3.02

25-3-14	35	0.102	180	123	3.02
1-4-14	40	0.109	180	124.5	3.19
2-4-14	37	0.103	180	124.5	3.01
2-4-14	39	0.107	180	124.5	3.13
8-5-14	42	0.114	180	124.5	3.33
8-5-14	41	0.11	180	124.5	3.22
8-5-14	43	0.112	180	124.5	3.27

3.3.2 Schütze Blank

The Schütze reagent selectively and quantitatively converts CO to CO_2 at room temperature, while preserving the original oxygen isotopic ratio of the CO (Schütze, 1949; Smiley, 1965). There is a background signal associated with the Schütze reagent that is likely due to impurities and/or diffusion of air across the o-rings located in the Schütze reagent vessel. However, the impurities released (water, trace amount of I_2 and SO_2) are reduced by condensation in trap 3 cooled with a dry ice alcohol bath (-70 °C) while transferring CO_2 to the cryo-focusing instrument. To quantify the Schütze signal ("Schütze blank") CO free air (zero air) is processed through the extraction line. The blank is non-linear and decreases with time (figure 3.2). Figure 3.2 shows the peak area of the Schütze blank measured in units Volt-seconds for 135, 150, 180, 240, 600 and 1200 seconds. Characterization of the Schütze blank is crucial for the correction of sample signal. Net sample signal is obtained by subtraction of the Schütze blank. Typical values for the Schütze blank are ~8 ppb (± 1.5 ppb), which corresponds to 10-

15% of a sample signal (depending on concentration, see Table 3.2). The bypass blank is included in the Schütze blank in Table 3.2. Corresponding blank corrections for the C and O isotopes are also made.

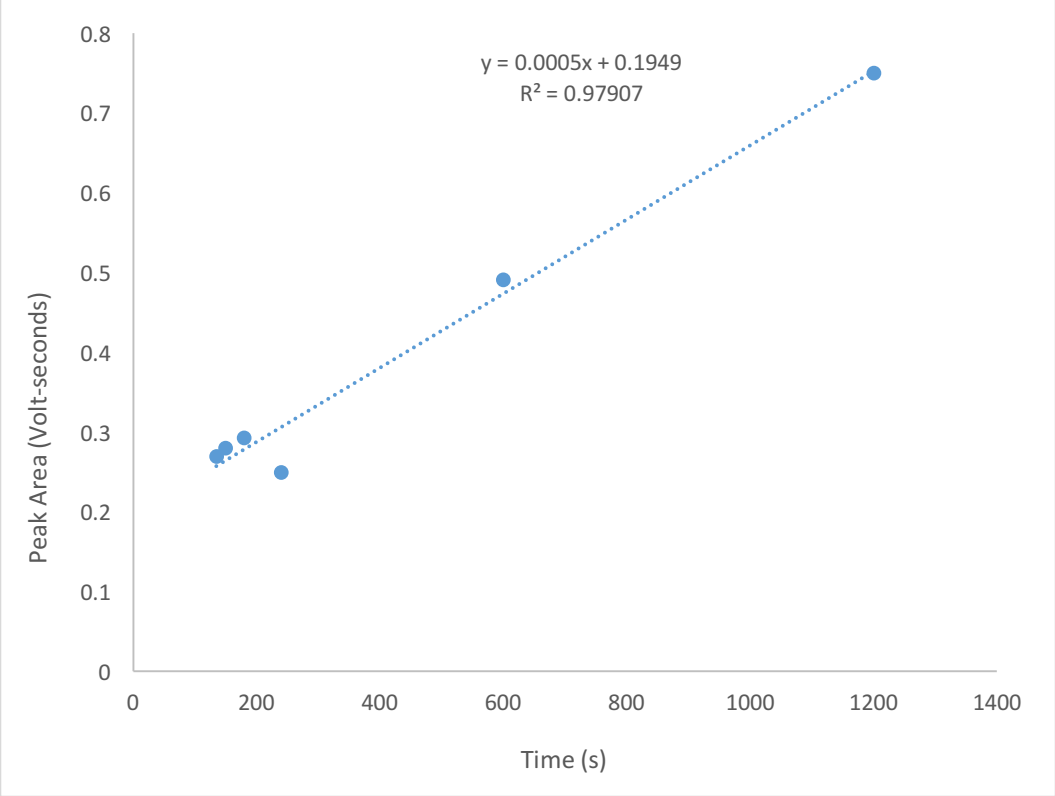

Figure 3.2: Schütze blank (V-s) as a function of time.

Table 3.2: Selected Schütze blank runs from 2015

Date	Sample time (s)	Peak Area (V-s)	$\delta^{13}C$	$\delta^{18}O$	[CO] ppbv
24-May	120	0.24	-22.4	21.8	10.2
23-May	120	0.21	-22.2	21.7	9.0
15-Oct	120	0.20	-23.3	21.8	8.5
11-Sep	120	0.17	-22.4	20.2	7.3
4-Sep	120	0.18	-22.4	20.2	7.7
24-Aug	120	0.17	-22.3	21.6	7.3
6-Aug	120	0.20	-22.4	21.2	8.5
24-Jul	120	0.17	-22.4	21.5	7.3

3.4 Calibration Gas

3.4.1 Isotope calibration gas

To validate the precision of the CO isotope analysis system, a calibration gas (secondary calibration) with a known concentration and isotopic composition is processed. During this work we used two different isotope calibration gases: a secondary standard and a working standard. The secondary standard has a known isotopic signature and concentration of CO, whereas the working standard only has a known concentration, but its isotopes are measured with respect to the secondary standard. The secondary standard isotopic values were determined previously and independently. An evaluation of calibration runs determines the accuracy and reproducibility of the system. The secondary calibration gas is ultrapure air mixed with CO, stored in an electropolished aluminum cylinder (Scott-Marrin, Inc., Riverside, CA) with an initial pressure of 102 atm (1500 psi).

Concentration and $\delta^{13}C$ and $\delta^{18}O$ values were determined by using an offline extraction of several hundred liters of calibration gas followed by dual inlet microvolume analysis with the IRMS (Mak and Kra, 1999; Mak and Brenninkmeijer, 1998). The CO concentration of the secondary calibration gas was determined volumetrically to be 141 ppbv based on a primary calibration using the NOAA/CMDL CO scale. $\delta^{13}C$ is calculated to be -45.56‰ with respect to V-PDB and $\delta^{18}O$ is -1.94‰ with respect to VSMOW based on the $\delta^{18}O$ of derived CO_2 and $\delta^{18}O$ of the oxygen from the I_2O_5 (Schütze reagent). $\delta^{18}O$ of the derived CO_2 from the secondary calibration gas was used for determining the $\delta^{18}O$ of the Schütze reagent and retrieving the original $\delta^{18}O$ of CO for ice core samples based on the following equation:

$$\delta^{18}O\ (‰, \text{VSMOW})_{sample} = 2\delta^{18}O_{CO2} - (2\delta^{18}O_{\text{2nd CalCO2}} - \delta^{18}O_{\text{2ndCal CO}}) \quad (11)$$

where $\delta^{18}O\ (‰, \text{VSMOW})_{sample}$ is the original $\delta^{18}O$ of CO in ice core samples, $\delta^{18}O_{CO2}$ is the measured $\delta^{18}O$ of CO_2 derived from sample CO, $\delta^{18}O_{\text{2nd CalCO2}}$ is the measured $\delta^{18}O$ of CO_2 derived from the CO in the secondary calibration gas, and $\delta^{18}O_{\text{2ndCal CO}}$ is the $\delta^{18}O$ of CO in the secondary calibration gas. There is a two in the equation to account for the two oxygen atoms; one from the Schütze and the other from the sample. The results of $\delta^{13}C$ (CO) and $\delta^{18}O(CO_2)$ are plotted as a function of 1/V-s (figure 3.3). Figure 3.3 shows a "Keeling plot", the inverse mole

fraction or in this case inverse Volt-seconds versus $\delta^{13}C$ (CO) and $\delta^{18}O(CO_2)$. V-s can be used because we can convert it to nanomoles. The Keeling plot analysis is used to confirm the isotope values of our 141 ppb reference gas as well as the value for $\delta^{18}O$ of our ice core samples. For the 141 ppb reference gas, the y-intercept, $\delta^{13}C$ (CO)=-45.08 and $\delta^{18}O(CO_2)$=-0.09 (figure 3.3) . The R^2 is 0.91 for both giving good confidence in the derived values. The accepted value for $\delta^{13}C$ (CO) of 141 ppb calibration gas is -45.56‰ therefore our Keeling plot shows a 0.48‰ offset, with respect to V-PDB. The $\delta^{18}O(CO_2)$ from the Keeling plot is -0.09 and is used in equation 11 to calculate $\delta^{18}O$ (‰, VSMOW) of the sample. The value calculated from equation 11 is later applied to correct all the ice core samples.

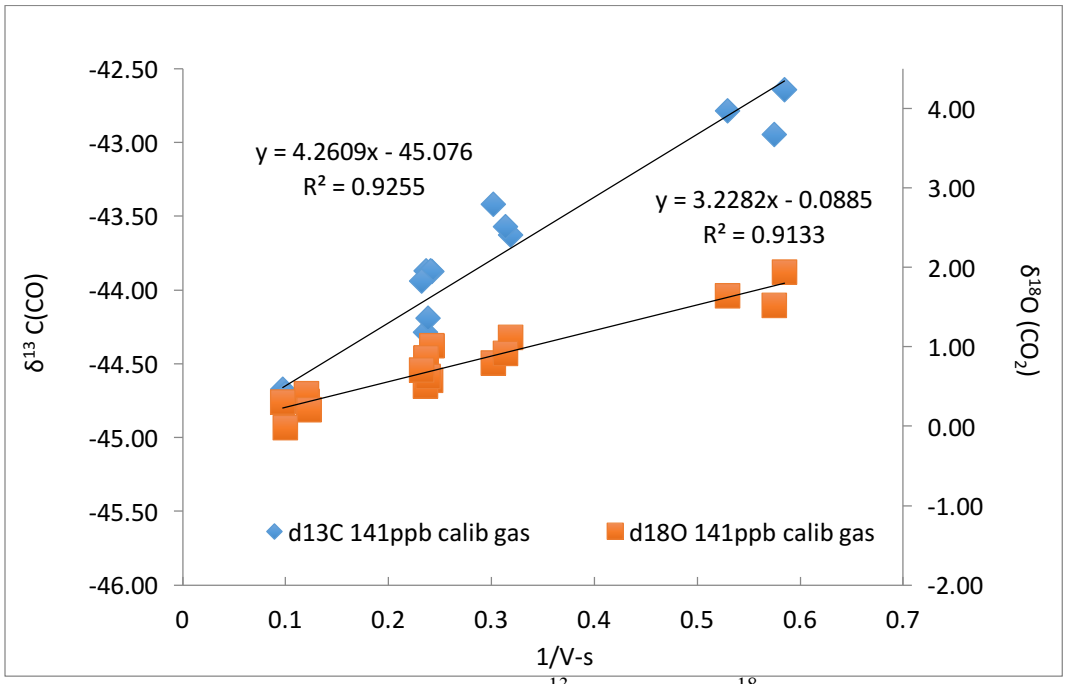

Figure 3.3: Keeling plot of 1/V-s versus $\delta^{13}C$(CO) and $\delta^{18}O(CO_2)$ derived for gas

samples from 141 ppb calibration gas.

3.4.2 Sensitivity and linearity tests

As mentioned above, the working standard is the one used daily, and has a known CO concentration (of 85.9 ppb, NOAA-CMDL scale). The isotopic signature has been characterized relative to the secondary calibration gas standard (above). We use the working standard to also determine the response (analytical sensitivity) of the IRMS by processing the gas according to the procedure described in section 3.2. Since we assume the concentration of the gas is 85.9 ppb, nanoliters of CO processed for calibration runs are calculated by the product of [CO] in the calibration gas (85.9 ppb) and the volume processed. From there the sensitivity or response of the instrument is calculated by dividing nanoliters of CO by the peak area (Volt-seconds) of the sample which is blank corrected (figure 3.4). Figure 3.4 shows the daily average sensitivity of the 85.9 ppb calibration gas (solid circles) calculated for the past year. Sensitivity varies over the course of the year from ~3.5 nL CO / V-s to ~4.5 nL CO / V-s and presently is at ~ 3.5 nL CO / V-s. The more recent data from August 2016 shows good agreement between the responses of our two different secondary standards (141 ppb, open circles and 85.9 ppb solid circles). The reason we observe this variation in sensitivity is due the blank changing throughout the year as opposed to an actual change in the response of the system. Also plotted is sensitivity of the calibration gas on ice which simply

means we loaded calibration gas into the ice container and are pulling the gas from the container instead of having a constant flow from the gas cylinder. There should be little to no difference between the two methods and our data are in agreement with this.

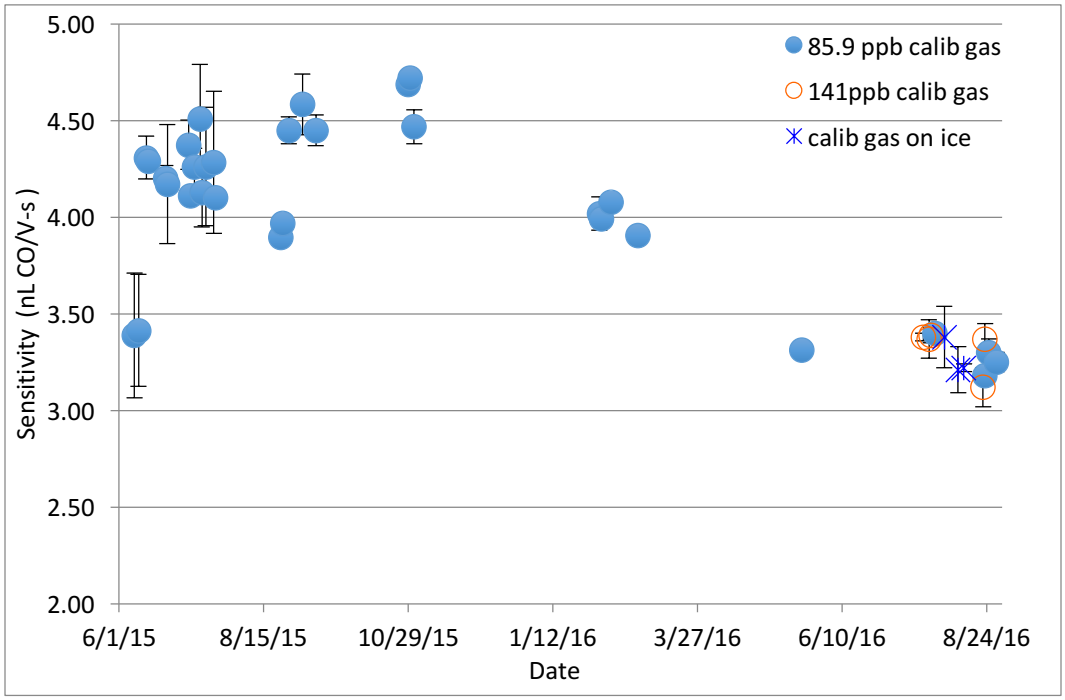

Figure 3.4: Sensitivity as a function of time. The error bars represent the standard deviation of the all the calibration gas samples run on that day. Samples with no error bars indicate that only one sample was processed that day.

Another indicator of the extraction line performance is to look at the linear response of the system (figure 3.5). Figure 3.5 is collection time versus Volt-seconds of 141 ppb calibration standard. This figure shows the excellent linearity observed between V-s and various collection times ranging from 45 s to 300 s of

the system and confirms the performance of the system.

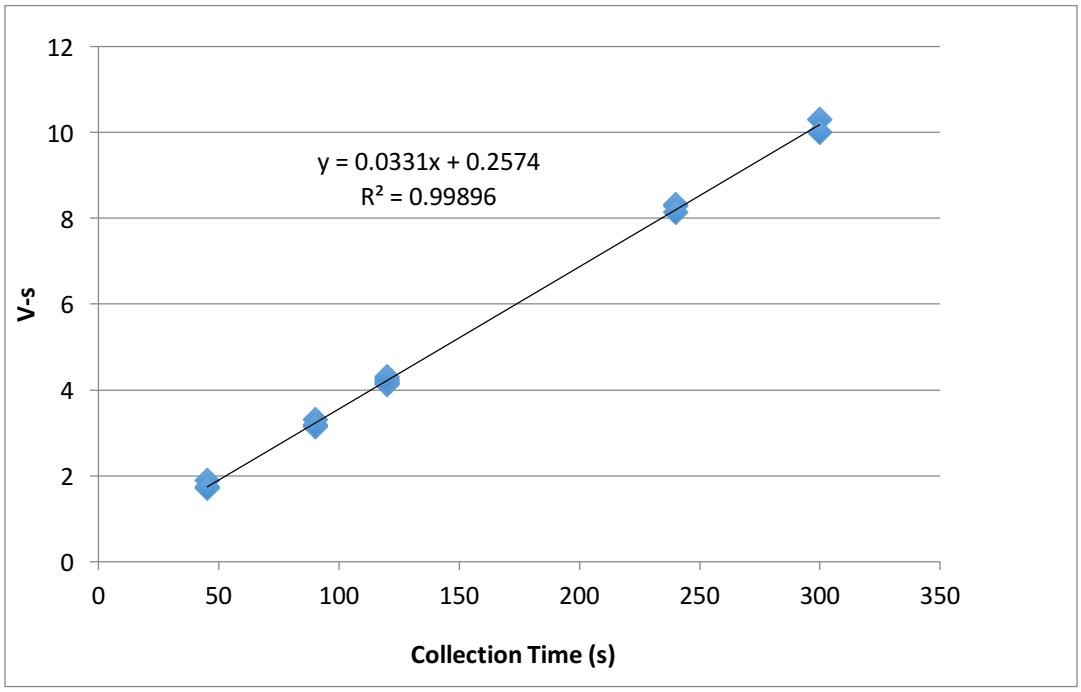

Figure 3.5: Collection time versus Volt-seconds of 141 ppb calibration gas standard

In summary, this chapter describes the successful implementation and performance of a newly built cryogenic gas extraction line allowing for the selective collection of the trace gas carbon monoxide from Antarctic ice cores samples for concentration determination and isotopic characterization.

4 Measurements of CO, ^{13}CO, and $C^{18}O$ in the West Antarctic Ice Sheet, Antarctica

4.1 Introduction

Reconstructing carbon monoxide concentrations over time is important because CO has a direct effect on atmospheric composition. When considering tropospheric chemistry, CO is involved with three main species: hydroxyl radicals, methane and ozone. First, and most importantly, is the control CO has on hydroxyl radical concentrations. Even though concentrations are relatively low (in the global troposphere, annual column average OH ranges from 1.0×10^5 to 22.0×10^5 molecules cm^{-3}) OH radicals greatly influence atmospheric chemistry as it is the main atmospheric oxidant for all reactive trace species (Lelieveld et al., 2016). An increase in CO concentration can reduce hydroxyl radical concentrations that therefore limits the oxidizing capability of the atmosphere to remove harmful pollutants such as hydrocarbons (Khalil and Rasmussen, 1988; Zimmerman et al., 1978). Second, an increase in CO concentration may also lead to an increase in the concentration of the important greenhouse gas methane, by inhibiting OH, since oxidation by OH is the major sink for methane. Lastly, CO also plays an important role in the regulation of tropospheric ozone. The interplay with ozone is difficult though as it has both negative and positive feedback mechanisms. CO can either increase or decrease concentrations of tropospheric ozone, which is

dependent upon the concentration of nitric oxide (Cicerone, 1988; Finlayson-Pitts and Pitts, 1986; Finlayson-Pitts and Pitts, 1997). Ozone, like methane, is also an important greenhouse gas as well as being a tropospheric oxidant and precursor to hydroxyl radical formation. In addition, OH and ozone are also important for the formation of secondary organic aerosols (Hallquist et al., 2009). Given all the complex reactions that involve CO, reconstructing past CO concentration and the contribution from different sources is of importance. In this chapter I present CO concentration and isotope data as measured in air bubbles trapped in ice cores and extracted according the procedure discussed in Chapter 3.

4.2 West Antarctic Ice Sheet Divide

4.2.1 Drilling site properties

Ice core samples in this study came from the West Antarctic Ice Sheet Divide in western Antarctica (79°28.048' S, 112°05.160' W). WAIS Divide is an ideal location for extracting ice cores and analyzing trapped gases because of its relatively high accumulation rate of ~22 cm yr^{-1}. The analyzed core was drilled at WAIS Divide (WAIS-D) under an NSF funded ice coring effort. A final depth of 3405 m was reached in 2011, yielding a 68,000-year-old climatic record. Samples used in this study were dry-drilled from borehole WDC06B in 2006. This borehole was drilled to a depth of 130 m and core diameter is 10 cm. After the core was drilled and allowed to settle onsite for one season, it was shipped to the

National Ice Core Laboratory (NICL) in Denver, CO were it sat in storage until the samples were cut for this analysis in November and December 2014. The cores were cut in half lengthwise and then cut in to 0.3 m pieces weighing ~1000-1100 grams each. Once we obtain the half cores, they are cut in half into two ~15 cm pieces, and processed face to face, thus reverting to the original 10 cm diameter core. WAIS Divide is located about 24 km from the current West Antarctic ice-flow divide, between the Amundsen Sea and Ross drainage basins. Due its high accumulation rate of about 22 cm ice equivalent per year, this site provides climatic records with unparalleled temporal resolution for the Southern Hemisphere. This location was chosen because it provides an undisturbed, high-resolution history as well providing a SH analogue to the GISP2 ice core from Greenland. The core also allows for trace gas analyses that are only marginally affected by diffusive smoothing throughout the firn column due to the high accumulation rate (Mischler et al., 2009; Mitchell et al., 2011, 2013; Marcott et al., 2014). Since the coring site is close to the divide, correction of climatic records for the effects of ice flow is minimized, and internal layers are more likely to be undisturbed and smooth. Accumulation rate for WAIS D is determined by the combination of ion chemistry data (top 70 m of the core) and continuous electrical conductivity and di-electric property (ECM/DEP) measurements from 70 m down to 298 m in the core (Mischler et al., 2009).

4.2.2 Dating the core

There is a relatively small difference between the ice-age and Δ age at WAIS Divide because of the high accumulation rate. Gas age reflects the diffusion that takes place within the firn (Schwander and Stauffer, 1984). Gases in the firn are in constant exchange with the overlying atmosphere, making it younger in age than the ice that surrounds it. This exchange continues until the air gets trapped in the ice matrix at the firn/ice transition region (76.54 m depth) and takes a few hundred years at WAIS D (Battle et al., 2011). Δ age is on the order of 205 years for the top 2100 m of the core and is determined using a 1-D firn-densification model (Marcott et al., 2014). The transport model gave a mean gas age of 9.9 years at the top of the lock-in-zone (65.5 m). The ice at this level was 215 years old at the time of drilling so Δ age is ~205 years. Δ age can be considered constant throughout the 130 m core because annual layer thickness obtained from the ECM/DEP counts show the accumulation rate at WAIS D remained constant over the last 1,000 years. Ice age is derived by various methods but mostly commonly it is calculated from counting annual snow layers similar to counting annual rings in a tree. The layers of the ice core get older and thinner with increasing ice depth. For example, at WAIS D, the average layer thickness of found at 40,000 years BP is ~1 cm compared to an average thickness of >15 cm 0-2345 years BP (0-577 m) (Sigl et al., 2015). The layers are identified from measured variations in ice composition and impurity content (i.e. by identifying

the chemical and physical difference between winter snow and summer snow). WAIS D ice chronology was obtained for the upper 2800 m of the core by counting the annual layers observed in the dust, chemical and electrical conductivity records (Sigl et al., 2015). Finally, the gas age versus depth scale was compiled by subtracting 205 from the ice age at every dated depth below the lock-in-zone. The gas age scale can be seen in figure 4.1. The uncertainty of the WAIS D ice core chronology is ±5%.

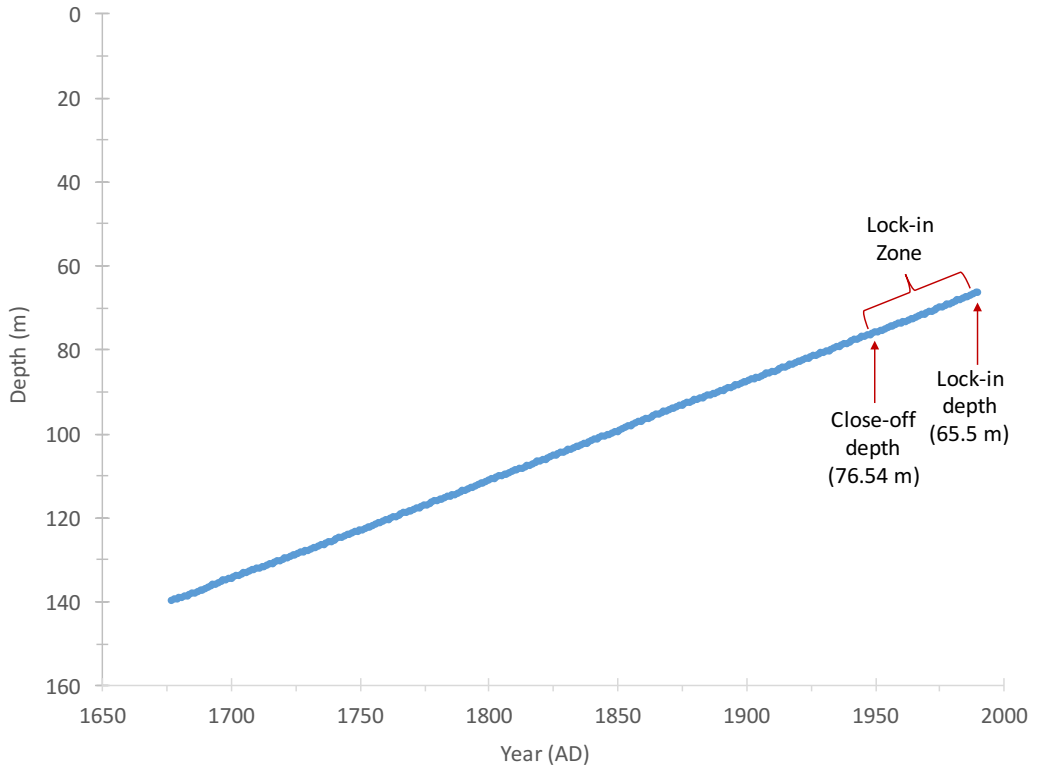

Figure 4.1: The depth-age relationship for WAIS-D. The lock-in zone (LIZ) extends down to 76.54 m (the close-off depth). The bottom of the LIZ is at the close-off depth beyond which all pores are closed off from one another both vertically and horizontally and no gas transport exists.

Even though the ice age is known with a high level of certainty, there

exists an uncertainty with the gas age scale. This is because the gas exhibits an age distribution before it is closed off. The only means to investigate the distribution is through modeling, typically a 1-D firn air diffusion model (e.g. Trudinger, et al., 2002; Schwander et al., 1993; Mischler et al. 2009 and Mitchell et al., 2011). Initial results indicate that the age distribution is ~ 30 years (Ahn et al., 2012; Battle et al., 2011). Generally speaking, in regard to firn air distribution trends, firn air from shallow depths is young and would be found in greater relative abundance compared to older air, reflecting the brief time over which diffusion has been taking place. However, as depth increases, the firn air becomes older, with a broader age spread. When this age distribution is averaged, an approximate 30-year gas age distribution is obtained. There is ultimately a smaller age distribution at WAIS Divide compared to other locations such as Berkner Island. Berkner Island has an accumulation rate of 12 cm yr^{-1} and a large age distribution of ~100 years (Assonov et al., 2007). This is because at higher accumulation sites like WAIS Divide, the air spends less time in the lock-in-zone so there is less time for mixing, therefore, giving a narrow age distribution. When considering a sample at some depth, to improve the accuracy of dating the gas, a more sophisticated model compared to the standard 1-D firn air diffusion model should be employed. Such a model is currently being developed by Patricia Martinerie and colleagues at the Laboratory for Glaciology and Geophysics of the Environment in Grenoble, France, and was not available at time of this

dissertation. For this reason, a conservative estimate of ± 10 years uncertainty are assumed in dated concentrations and isotopes in this thesis (Mitchell et al., 2011).

4.3 CO concentration results and discussion

4.3.1 CO Concentration

The CO concentration data is displayed in figure 4.2. Of the 42 samples processed from WAIS D there are five samples that are located above the close-off (76.5 m, 1950 AD), at depths 71, 72, 74, 75 and 76 meters. All of these samples exhibit anomalously high concentrations of 105, 100, 99, 78 and 107 ppbv, respectively (figure 4.1, patterned red circles). There could be several reasons why the concentrations are high but the most likely scenario for the observations is the entrapment of modern ambient air after the collection of the ice cores. This could happen because open pores existed at the time of core recovery. A study by Aydin et al. (2010) supports this idea. In their paper, firn air and ice core samples from three Antarctic sites including WAIS D were analyzed for CFC-12. The firn air data are consistent with the known atmospheric history of CFC-12. However, some of the ice core samples collected near the firn-ice transition exhibit high CFC-12 level and are indicative of modern air entrapment. It is highly unlikely that the observations can be attributed to in-situ production or analysis artifacts because CFC-12 levels are undetectable in deeper ice not to mention the firn air profiles are consistent with the known history of industrial production of CFC-12

(Aydin et al., 2010).

The data presented in figure 4.2 is the first CO concentration record from the WAIS Divide, as well as the first record of CO concentration from ice for the time period ~1900-1950 in the Southern Hemisphere. Filling in the record from ~1900-1950 is of importance since no CO measurements from ice are available for this time period in the Southern Hemisphere. For the time period between 1900-1950 the data show a ~7 ppbv increase relative to the end of the 20th century with an average concentration of 62 ppbv ±5 ppbv (figure 4.2). One might expect more CO from fossil fuel burning in the early 20th century, but the contribution would still be small considering the location of the site (the remote SH).

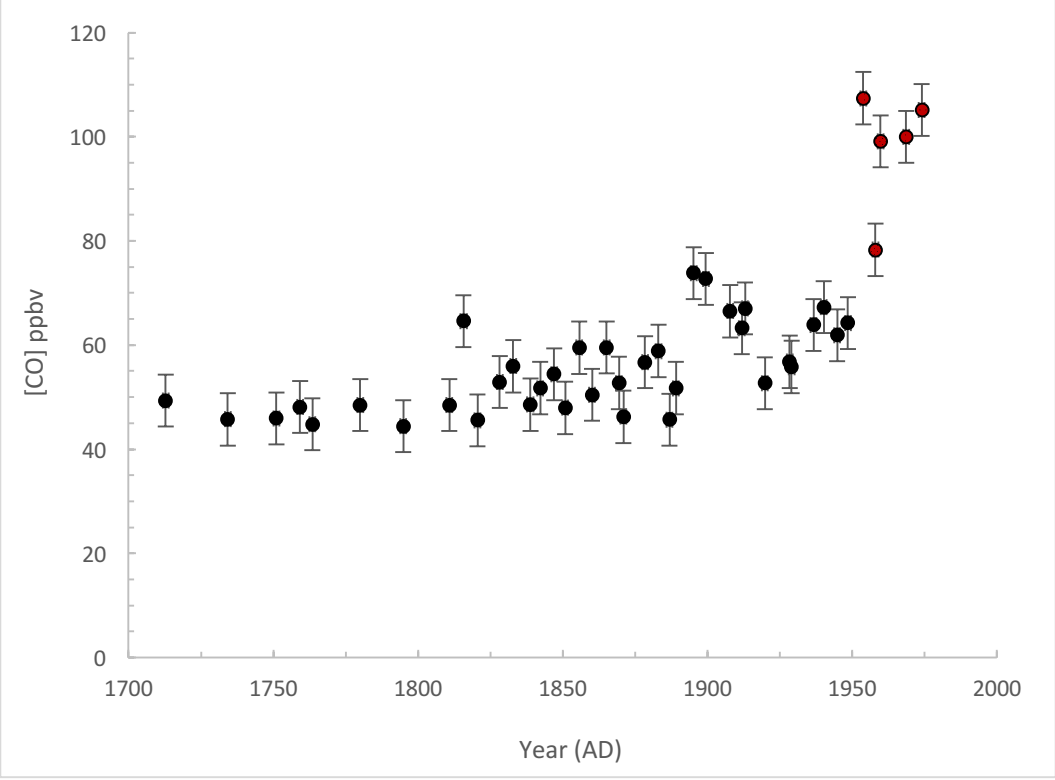

Figure 4.2: CO concentration from WAIS Divide, Antarctica. The patterned red circles represent the samples taken above the close-off (76.5 m, 1950 AD).

For example, a recent modeling study by Park et al. (2015) showed that only 2.6 ppbv CO from fossil fuel combustion contributes to CO concentrations at Scott Base, Antarctica. The charcoal index, which is a proxy for burning (see Chapter 1), including both natural and anthropogenic sources, shows an increase in regional burning from tropical South America from 1900-1950 but a decrease from Southern South America (Power et al., 2012). It should be noted that while the charcoal record is used as a proxy for burning, it is not without limitations. Charcoal is a particulate, not a gas, and therefore neither homogeneously mixed nor transported long distances compared to CO. However, it can serve as a very regional tracer. Just because there is structure within the charcoal record does not necessarily mean it will be, or should be, reflected in the CO budget in the remote SH. Nonetheless, it can be used to help identify biomass burning trends.

Prior to the 20th century, from about 1825 to 1900, concentration was close to modern day southern hemisphere values (55 ppbv) while in the hundred years prior from ~1700-1825 CO concentration was lower by about 7 ppbv relative to present day (figure 4.2). In general, these new data show that CO concentration over the past 250 years deviated from modern measurements indicating a change in the relative contribution from different CO sources.

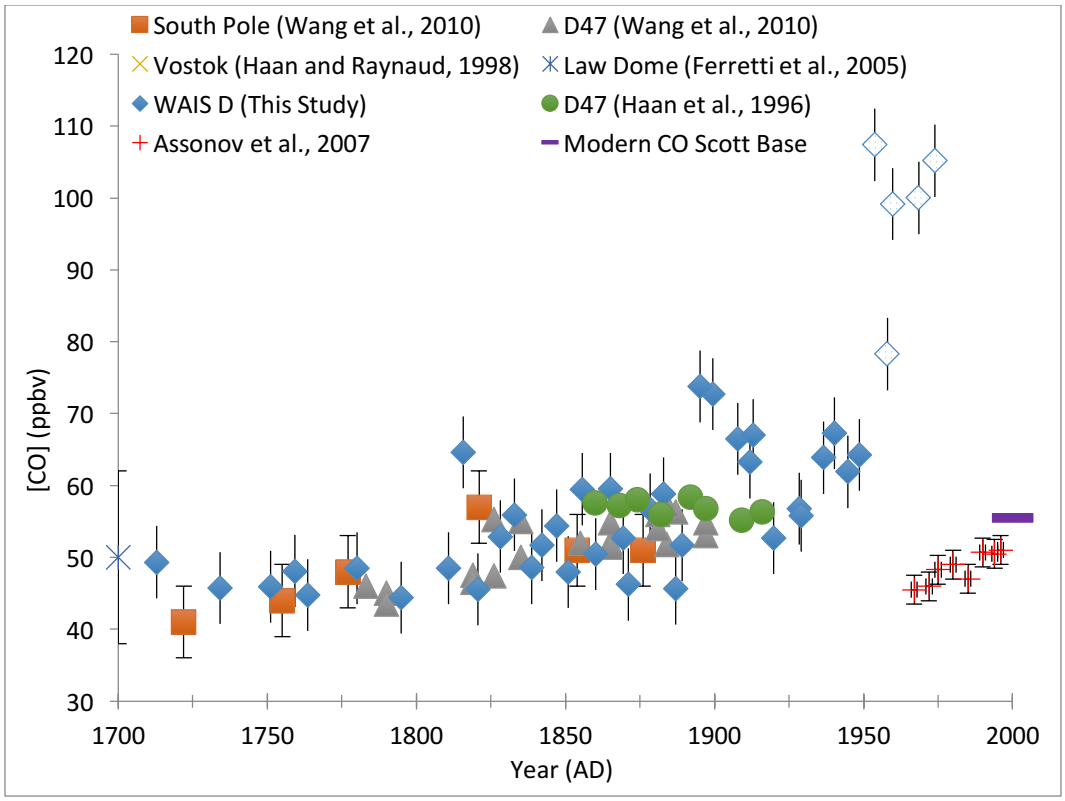

Figure 4.3: CO concentration from Antarctica, 1700 - 2000 AD, from different data sets as indicated in legend. The new data from this work is shown as solid blue diamonds. The open diamonds represent the samples that were taken above the close-off depth and are contaminated by ambient air.

WAIS D CO concentration data is plotted along with the [CO] record from previously published work from South Pole, D47, Vostok, Law Dome and Berkner Island in figure 4.3 (Wang et al., 2010; Haan and Raynaud, 1998; Haan et al., 1996; Ferretti et al., 2005; Assonov et al., 2007). Wang et al., (2010) shows a fairly constant [CO] of 55.2 ppbv (±1σ standard deviation: 2.3 ppbv) between 1865 and 1897 while Haan et al. (1996) indicates a fairly constant [CO] of 56.9 ppbv (±1σ standard deviation: 1.1 ppbv) in D47 ice core between 1860 and 1916.

The data presented here also indicate a fairly constant [CO] of 55.2 ppbv (±1σ standard deviation: 5 ppbv) between 1860 and 1900. It should be noted that the analytical method by Haan et al. (1996) and Haan and Raynaud (1998) was much different than ours and relied on gas chromatography using a mercuric oxide detector for CO concentration where we use a CF-IRMS, and absolute calibration of his measurements is not known since the gas standards he used are no longer available.

Overall, the WAIS D data is in good agreement with previously published work from D47 and South Pole from 1700-1900 (Wang et al. 2010). The data by Ferretti et al. (2005) does not agree with previously published work but that record has a large uncertainty (± 13.5 ppbv) (figure 4.9). In that study, the authors reported significant CO contamination in their results, and the reported concentration values are seemingly unrealistic for the remote southern hemisphere. The CO measurements by Assonov et al. (2007) show CO concentration record from firn as opposed to ice cores. Extracting air from firn is much different than ice cores and introduces its own set of analytical uncertainty. For example, the air is sucked out from the firn in situ, using a pump and big gas containers including ample Teflon tubing and sealants on the top of the ice hole (Assonov et al., 2007). The firn air samples from Assonov (2007) were from Berkner Island, a coastal Antarctic site with a much lower accumulation rate (12 cm yr^{-1}) and warmer temperature (−25.0 ºC) than WAIS Divide. In general, firn

measurements have been proven difficult especially since there is a large uncertainty associated with dating the firn air, which is derived from firn diffusion models (Trudinger et al., 2004; Assonov et al., 2007). Furthermore, an additional uncertainty is present due to smoothing of atmospheric signals in firn as well as loss of information caused by processes such as diffusion (Trudinger et al., 2004). Another issue with the data from Assonov is they stored their samples in electropolished stainless steel cans. Storage of CO is always a challenge, because of in situ production from possibly contamination (Novelli et al., 2003). Overall their data show a range in CO concentration from 45-51 ppbv (±2 ppbv) from ~1970-2000 (figure 4.3). They report a higher mean CO level of 52.5 ppbv (±2 ppbv) for the years 1994 to 2002 compared the same period for flask measurements by NOAA/CMDL at Antarctic stations where the CO concentration measured was 48.6 ppbv (±1 ppbv). Comparison with the Assonov CO measurements is difficult since the underlying calibration standards are different. Our CO measurements are calibrated to the NOAA CMDL scale whereas the absolute scale used by Assonov et al. (2007) is based on volumetric determinations only (Brenninkmeijer et al., 2001).

Ideally, multiple ice core records from sites with different physical and chemical characteristics (e.g., temperature, accumulation rate and organic impurity levels) are needed to validate that the observed record is in fact an atmospheric signal. The good agreement between our data and records from South

Pole, Vostok, D47 and WAIS-D until about 1920 supports our measurements of atmospheric CO.

4.3.2 Methane contribution to atmospheric [CO]

Examining atmospheric methane concentrations can help to provide insight into measured CO concentrations. Methane is a relatively long-lived gas with an average lifetime of 10 years. It is therefore well-mixed in the troposphere and has a one-year interhemispheric gradient reflecting the average mixing time between the two hemispheres. Methane and CO are both trace gases that have natural as well as anthropogenic sources not to mention both are associated with biomass burning although it is well documented that biomass burning has a larger effect on CO than on methane (Andreae and Merlet, 2001). As discussed in detail in Chapter 1, methane is oxidized to CO and is the dominant source of CO in the southern hemisphere present day with contributions up to 45% of the total budget (figure 4.11, Park et al., 2015). Methane has many sources including emission during the production and transport of coal, natural gas, and oil. Methane emissions also result from livestock and other agricultural practices and by the decay of organic waste in landfills. Termites, rice and biomass burning are additional sources. However, the largest source of methane today is emitted by wetlands and how its emission has changed overtime is debated in the community (Ruddiman, 2003; Spahni et al., 2005; Chappellaz et al., 1997; Singarayer et al., 2011). The major sink for methane is oxidation by OH which produces CO.

Globally average methane concentration present day is 1840 ppb (NOAA ESRL/ GMD).

The atmospheric methane record is well document for the time period of ~1700-1950 as depicted in figure 4.4. The record is robust and there are multiple measurements because methane concentration is relatively easy to determine due to is stability (long lifetime and high concentration) relative to CO (Ferretti et al., 2005; Brooks et al., 2009; Mitchell et al., 2011). Looking at the record, methane nearly doubled during the 20th century and increased 150% since 1750 (figure 4.4) (data from Etheridge et al., 1998). We can use the well-known methane record to calculate the contribution from methane to the SH CO budget as is discussed in detail below.

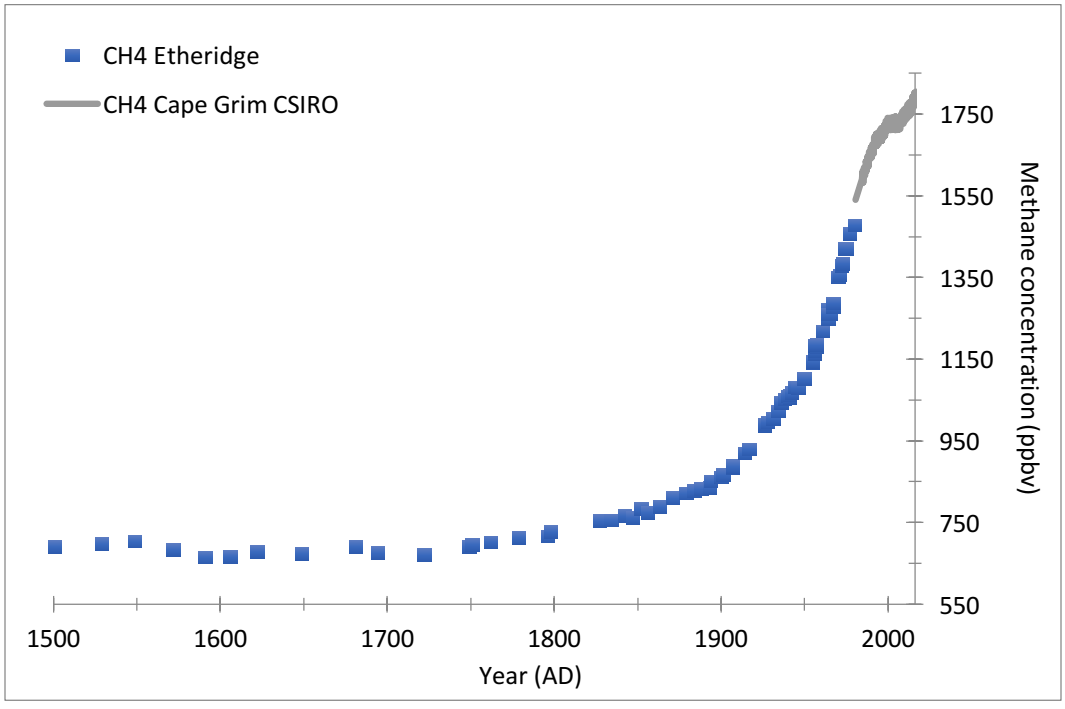

Figure 4.4: Methane concentration (ppbv) record through time from Law Dome, Antarctica (blue squares) (uncertainty ±5ppbv) (Etheridge et al., 1998) and from Cape Grim Tasmania, Australia (grey line) (data from Commonwealth Scientific and Industrial Research Organization (CSIRO)).

The steady state contribution of CO from methane can be calculated as the product of the ratio of the CO+OH and CH_4+OH rate constants and CH_4 concentration ($[CO]_{CH4,ss}=(k_{CH4+OH}/k_{CO+OH})*[CH_4]$) (figure 4.5) Steady state is assumed, since the average atmospheric lifetime of CH_4 is on the order of ten years, and the average CO lifetime is a few months. The rate constant for CO + OH is $k(CO)= 9.1x10^{-19}T^{1.77}e^{580/T}$ x $[1+2.4x10^{-20}[M]\ (T/298)^{-1}]$ cm^3 $molecule^{-1}s^{-1}$ (where [M] is equal to the concentration of air, O_2 or N_2 in molecule cm^{-3}). As can be seen from the equation there a strong linear dependence of pressure and a small dependence of temperature (Atkinson, 2003). The rate constant for CH_4+OH is $k(methane)=1.85x10^{-20}T^{2.82}e^{-987/T}$ cm^3 $molecule^{-1}$ s^{-1} (Atkinson, 2003). The overall uncertainty in the rate constant is estimated to be ±20-30%. The methane-derived CO calculated using this approach and historic methane concentrations (figure 4.4) are shown in figure 4.5. While this method is a reasonable approach to calculate the CO concentration from methane, representing a kind of back on the envelope estimate, it is not the most accurate method. Rather, we use the output from a 3-D CTM (chemical transport model), in this case the Model for OZone And Related chemical Tracers (MOZART-4) (Emmons et al., 2010). MOZART is a three-dimensional chemical

transport model and uses a complete CO-CH_4-OH atmospheric chemistry package. Methane-derived CO for 2005 was calculated for Antarctica using MOZART and was found to be 27 ppbv (Park et al, 2015). The methane concentration used for this simulation was taken from NOAA ground based measurements and was ~1728 ppbv in the Southern Hemisphere (Dlugokencky et al. (2005). To calculate the methane-derived CO component in the past, we use the ratio of methane-derived CO to CH_4 concentration from the MOZART model simulation of the year 2005, and normalize it to the historic concentration of CH_4. Historic CH_4 concentrations are from Etheridge et al., 1998 (figure 4.4) Figure 4.5 shows the results from this approach along with the back-of-the envelope approach discussed previously. The trend in both cases is the same but the values differ by between ~1.5-3 ppbv. This offset is mostly due to the assumed yield during CH_4 oxidation (100% yield was assumed whereas the model takes into account loss of intermediate species, wet and dry deposition of CH_2O, etc.). The difference between the two approaches varies with time mostly because of the the temperature dependence of the CH_4-OH rate constant and the pressure dependence of the CO-OH rate constant, which are not captured as precisely in the simple approach compared to the model. However, both calculations mirror each other because they use the same CH_4 concentrations, which is the most important variable in the calculation in both cases.

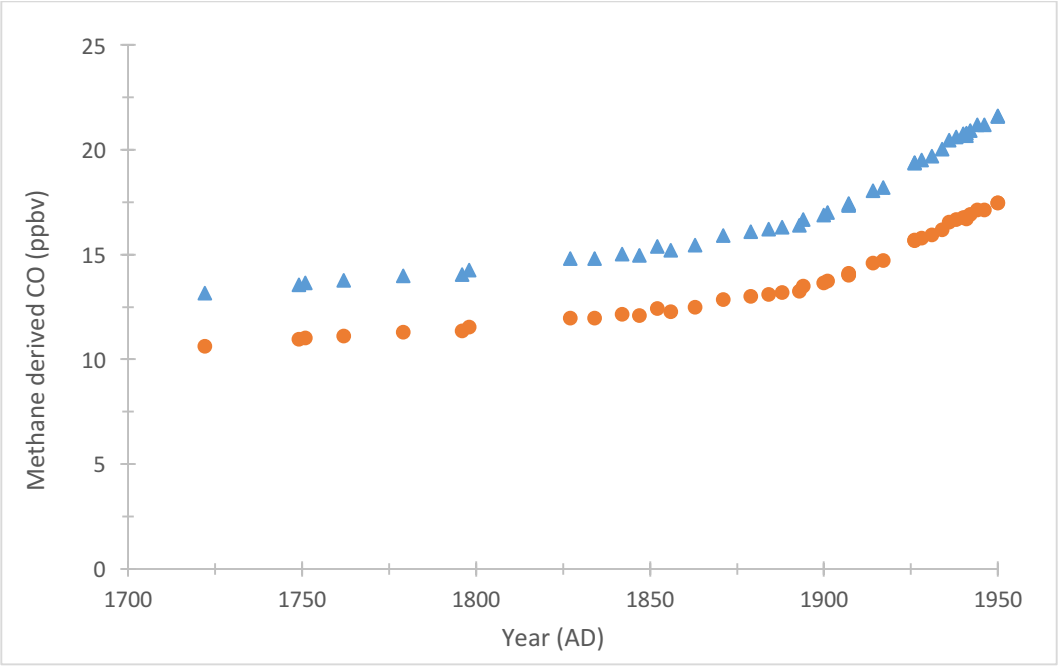

Figure 4.5: Methane derived CO based on rate constants from Atkinson (2003) (blue triangles) and MOZART (orange circles) (Park et al., 2015).

Figure 4.6 shows the concentration of methane (grey circles) and the contribution of methane to CO based on the MOZART results and the CH_4 data from ice cores (figure 4.4) (orange triangles) over the time period relevant to this study (1700-1950). During this time period, methane concentrations increased by 40% as did the methane contribution to the CO budget. The most rapid change occurred from 1900-1950. There are many reasons why methane concentrations increased, with the most important being an increase in agriculture activity, specifically cattle and rice paddy fields. Cattle (for beef and dairy) and rice paddy cultivation make up ~30% of the present day methane budget (Reeburgh, 2004). Between 1900 and 1950, there was more than a 50% increase in world population,

from 1.6 billion to 2.5 billion people (Kremer, 1993). This caused an increased demand for higher food production, including dairy, beef, and rice. A typical dairy cow releases between 70 and 120 kg of methane annually. Rice paddy fields account for ~20% of the anthropogenic emissions of methane (IPPC, 1996). The major mechanism for methane production in the flooded soils of rice paddy fields is the reduction of CO_2 with H_2, with fatty acids or alcohols as hydrogen donor, and the transmethylation of acetic acid or methanol by methane-producing bacteria (Takai, 1970; Conrad 1989).

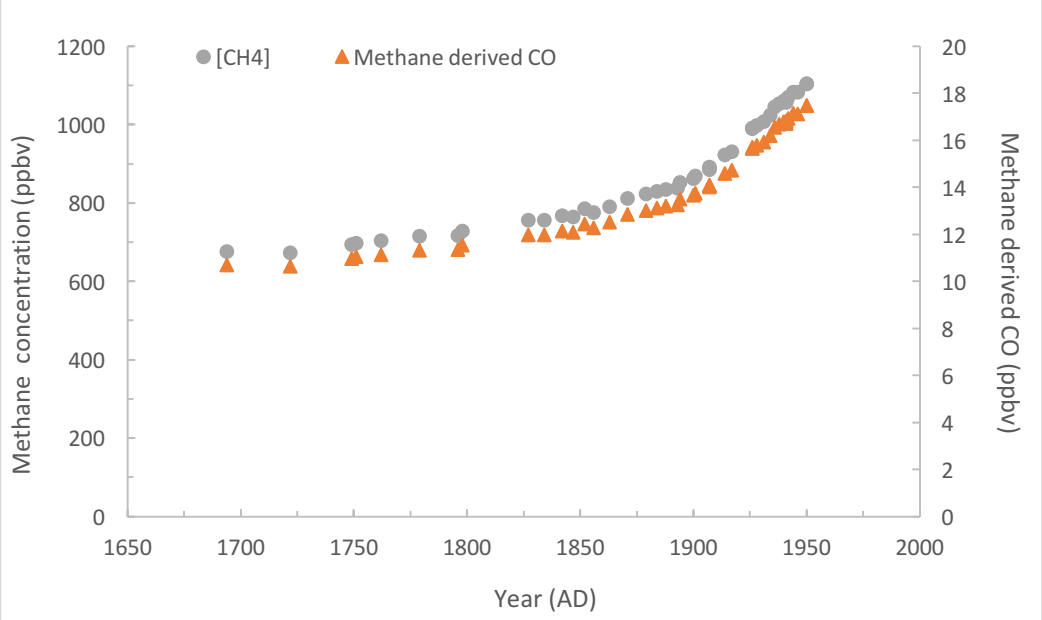

Figure 4.6: The evolution of atmospheric methane (grey circles, left scale, Etheridge et al., 1998 and CSIRO) and methane derived CO (orange triangles, right scale) in ppbv.

4.3.3 The non-methane fraction of observed CO

Since the concentration history of methane is well known, its contribution to the

overall budget can be calculated with high accuracy. The methane-derived CO (figure 4.6) can be subtracted from total observed CO concentration (figure 4.2) to obtain the non-methane CO fraction, or the residual CO (figure 4.7). Residual CO represents all the non-methane sources of CO; i.e. biomass burning, VOC oxidation, fossil fuel combustion, and oceanic emissions (the latter being small). Overall, our data show consistently low CO from 1730-1800, a significant increase in the beginning of the 19th century followed by a significant decrease in the late 19th century, then an increase in the early 20th century (figure 4.7). The residual CO shows little variation (~4 ppbv) from 1700-1820 and then significant variability from 1820 on. To examine decadal trends in non-methane CO concentrations, the residual CO data are binned every 10 years starting at 1710 (figure 4.8). The open circles represent bins where there was only one data point. All the other data points (solid circles) had 2 or 3 samples which were averaged and the error bars show the uncertainty ($\pm 1\sigma$). The binned data better show the 19^{th} century increase of ~7 ppbv and the 20^{th} century increase of another ~7 ppbv (figure 4.8). What this implies is that there is more CO from non-methane sources than from methane sources. For the time period of the new data, 1900-1950, even though there is an observed 22% increase in atmospheric methane, the contribution from non-methane sources is higher than the methane contribution. There are 5 samples at the turn of the 20^{th} century (1895 - 1913) that are higher than the 19^{th} century concentration (figure 4.7). These data include five samples,

spanning 18 years giving us confidence that these data represent actual CO concentrations and thus represent a true spike in the atmospheric signal. There is no indication that the analyses system was not functioning properly as the blanks and the calibration gas from those days are all within our accepted uncertainty. Also, all five of the samples were processed on different days. In some cases, the samples were processed months apart.

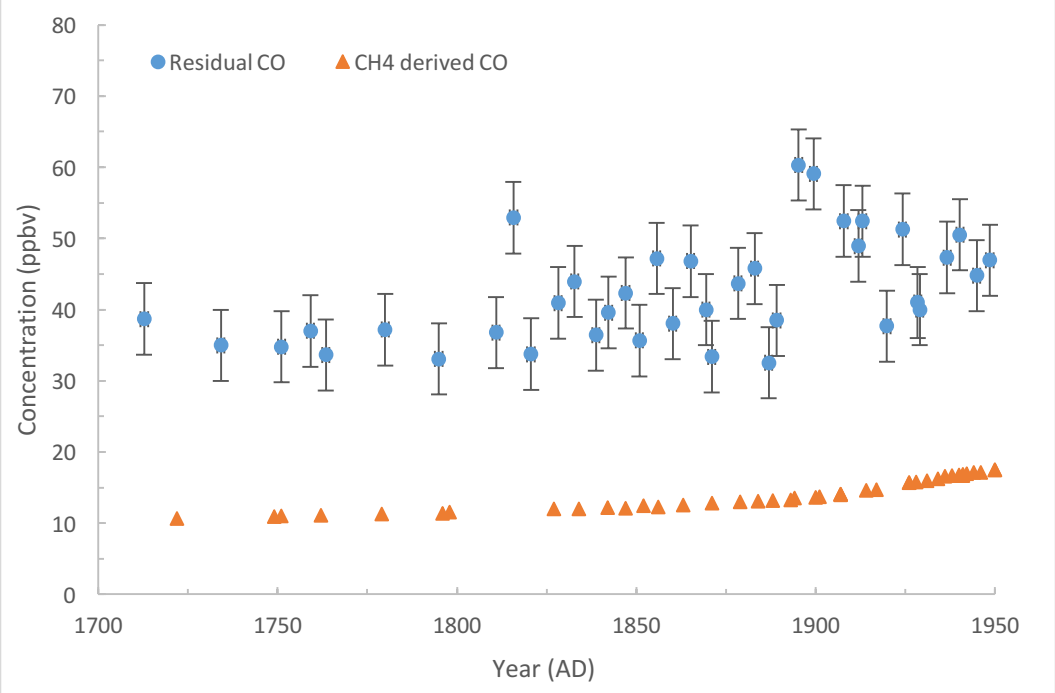

Figure 4.7: Residual (blue circles) and methane derived (orange triangles) CO in ppbv.

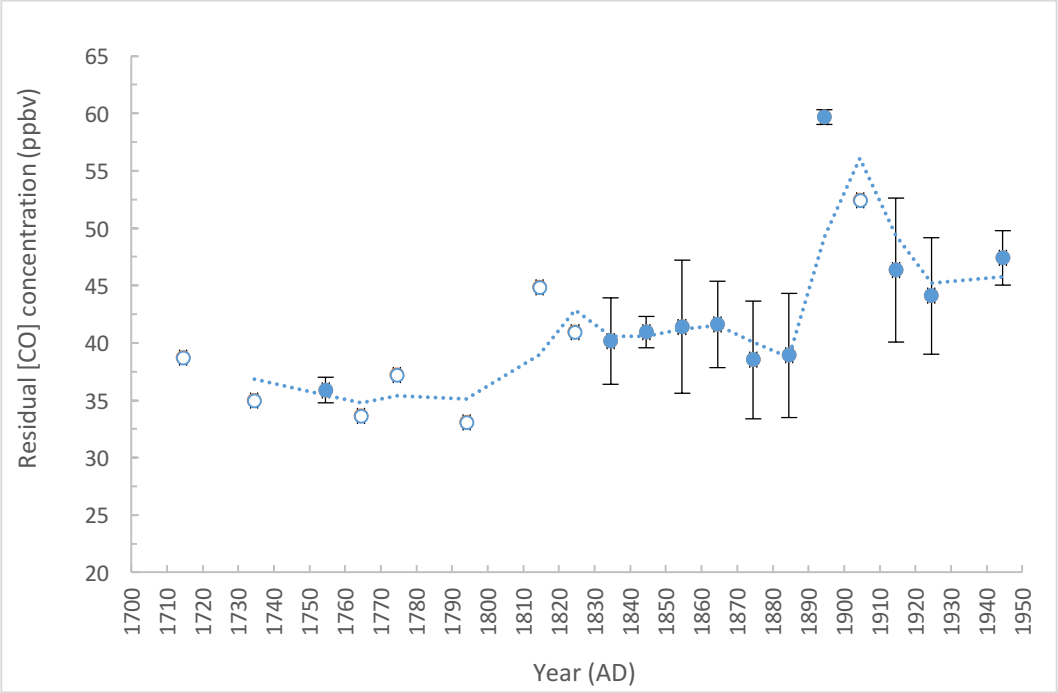

Figure 4.8: Residual CO concentration data binned every 10 years (circles) with a 2 variable moving average (line). Open circles represent a 10-year bin that only consisted of 1 data point. All other bins included 2-3 data points and are shown with (±1σ).

In conclusion, we present here the first CO data from Antarctic ice cores covering the time period 1900-1950. We also present the first CO measurements from WAIS Divide, a site allowing for trace gas history with high temporal resolution dating back to 1700 AD. Our record is in good agreement with previously published work and shows a 20 ppbv (±5ppbv) increase from 1700-1950 (figure 4.9).

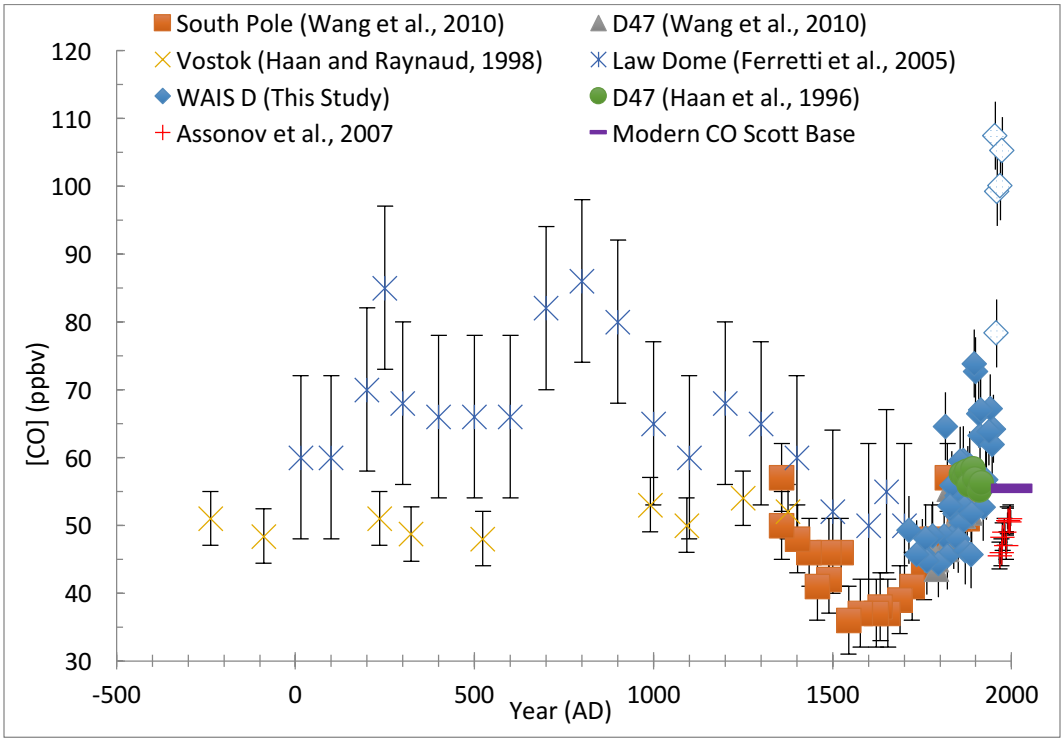

Figure 4.9: CO concentration over time from different data sets as given in legend. The new data from this work is shown in solid blue diamonds. The open diamonds represent the samples that were taken above the firn ice close-off and likely contained ambient air. Other Antarctic concentration data are from Wang et al., (2010) (orange squares, South Pole and grey triangles, D47); Haan and Raynaud (1998) (yellow X, Vostok); Haan et al. (1996) (green circle, D47) and Ferretti et al. (2005) (blue stars, Law Dome). Also shown is CO concentration from firn air (red cross, Berkner Island, Assonov et al., 2007) and modern CO concentration (purple dash, Scott Base, Park et al., 2015).

4.4 $\delta^{13}C$ and $\delta^{18}O$ in CO from WAIS Divide

The isotopic record of CO coupled with concentration data can provide insight to the relative contribution of the various sources of CO. Since different CO sources have distinct isotopic signatures, the isotopic ratios can be used to investigate the relative contribution from different sources (see tables 4.1 and 4.2). In the Southern Hemisphere, the fossil fuel component to the CO budget is minimal, leaving three main sources: methane derived CO, biomass burning, and NMHC oxidation. Methane-derived CO is calculated as described above, and once that component is removed from the equation, the primary sources of CO are biomass burning (including biofuels) and NMHC oxidation. Each of these sources have distinct $\delta^{18}O$ signatures. In the next few sections I discuss the application of both $\delta^{13}C$ and $\delta^{18}O$ in the paleo CO record.

As discussed in Chapter 3, during sample extraction, atmospheric CO is oxidized to CO_2 via the Schütze reagent, so that the CO-derived CO_2 can be handled cryogenically (CO does not condense at liquid nitrogen temperature and it is a difficult gas to process). Thus, what is measured is the peak area of mass 45 (in V-s) in the CO-derived CO_2, which then corresponds to $\delta^{13}C$ of CO-derived CO_2. In the case of $\delta^{13}C$, the oxidation step does not alter the signature of CO, however there is an added correction from the background signal emanating from the Schütze reagent, as discussed in Chapter 3. The $\delta^{18}O$ of CO_2 undergoes an

additional step to get to the $\delta^{18}O$ CO because of the addition of an oxygen atom from the Schütze to yield $\delta^{18}O$ of CO The equations to calculate the $\delta^{18}O$ of CO are shown in section 3.4.1, Chapter 3.

The other correction that is applied to the $\delta^{13}CO$ record is for gravitational effects. Gravitational fractionation in the firn column is mass dependent meaning that the heavier isotopologues of CO are preferentially found at the bottom of the firn (discussed in Chapter 2). We follow the approach as outlined in Sowers et al. (1992). In this method the isotopic shift in $\delta^{15}N$ of N_2 between the top (surface) of the firn and the base (close-off; 76 m depth) is used to determine the isotopic shift for CO. The correction for gravitational settling for $\delta^{13}C$ of CO is 0.31‰ and for $\delta^{18}O$ of CO is 0.62‰. The final corrected data set for both $\delta^{13}C$ and $\delta^{18}O$ of CO is shown in figure 4.10. The uncertainty in the isotope ratios is calculated by taking the average of the standard deviations of 85.9 ppbv calibration gas runs on the actual ice sample for each day that a sample was processed. The uncertainty is 0.4 ‰ and 0.7 ‰ for $\delta^{13}C$ CO and $\delta^{18}O$, respectively.

This is the first time $\delta^{13}C$ and $\delta^{18}O$ in CO have been measured from WAIS Divide (figure 4.10). Because of the high accumulation rate at WAIS Divide, these data represent a much higher resolution over the past 200 years than any previously published data set (Ferretti et al., 2005; Wang et al., 2010). As can be seen in figure 4.10, $\delta^{13}C_{CO}$ shows a negative trend with time, meaning that CO is becoming isotopically depleted, by about 4‰ in $\delta^{13}C$ from the 1700s to the mid-

1900s. On the other hand, $\delta^{18}O$ of CO (with respect to V-SMOW), is more variable with no immediately observable trend. Because these data have been examined carefully and no experimental error has been identified for the data shown, it is assumed the observed variability in $\delta^{18}O$ is a measurement of the temporally varying change in relative sources and sinks of CO, and that the temporal variations are observable because of the high accumulation rate at the WAIS D site (22 cm yr^{-1}) results in a minor amount of smoothing of the CO record; each data point is an integration of only 2-3 years. The globally averaged atmospheric lifetime of CO is about 3 months so interannual variations in the flux of certain sources of CO could result in potentially large variations in observed [CO] and its isotopes. A detailed analysis of the observed variability is presented in the subsequent sections.

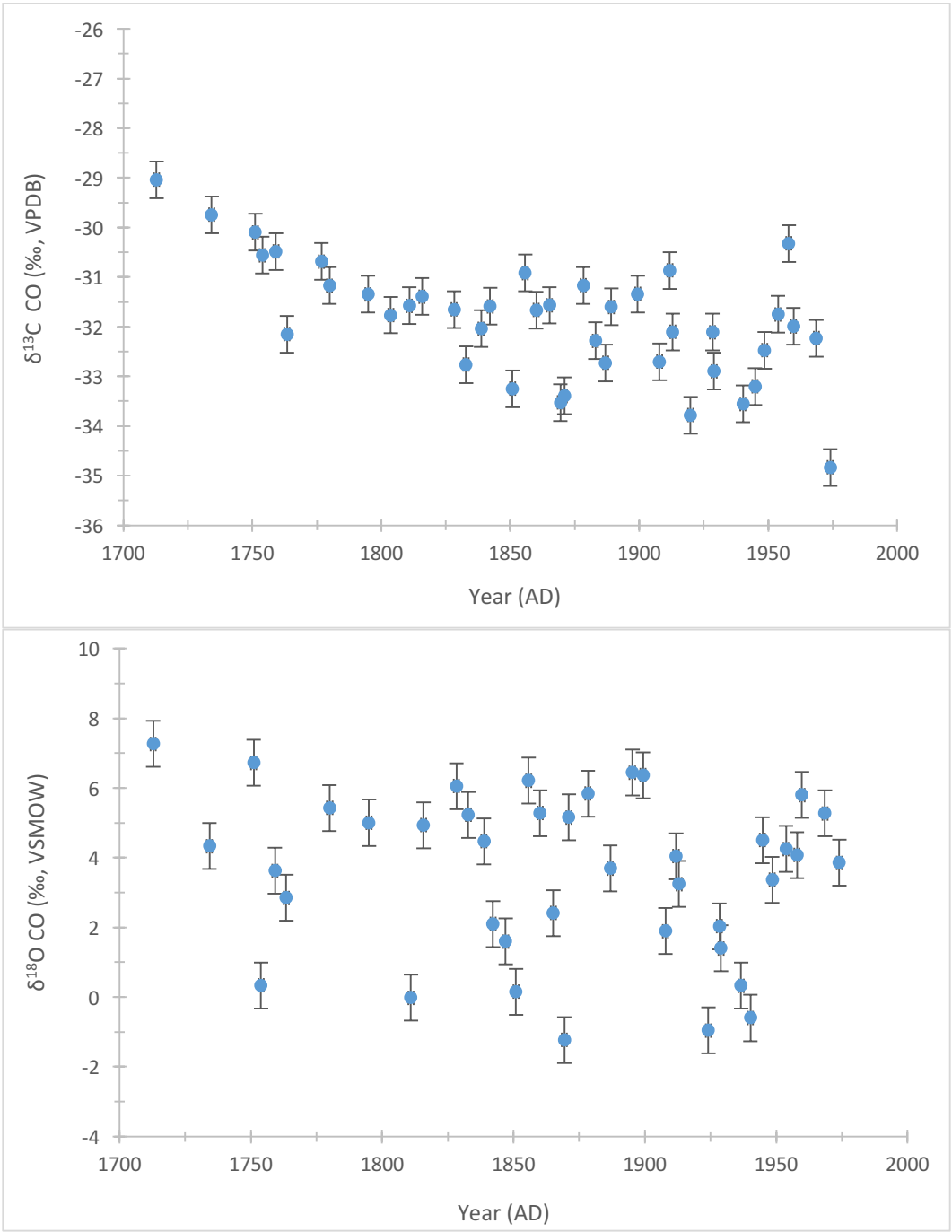

Figure 4.10: Top panel: $\delta^{13}C_{CO}$ (‰, VPDB). Bottom panel: $\delta^{18}O_{CO}$ (‰, VSMOW) from WAIS Divide.

4.4.1 Isotopic mass balance analysis

In order to help understand the contribution of the different CO sources to the overall budget an isotope mass balance model is applied to our data. The source compositions of CO can be evaluated based on the following equations:

$$[CO_A]+[CO_B]+[CO_C]+[CO_D]+[CO_E]+[CO_F]+[CO_G] = [CO_T] \quad (12)$$

$$[\delta^{13}C_A]x[CO_A]+[\delta^{13}C_B]x[CO_B]+[\delta^{13}C_C]x[CO_C]+[\delta^{13}C_D]x[CO_D]$$
$$+[\delta^{13}C_E]x[CO_E]+ [\delta^{13}C_F]x[CO_F]+[\delta^{13}C_G]x[CO_G] = [\delta^{13}C_T]x[CO_T] \quad (13)$$

$$[\delta^{18}O_A]x[CO_A]+[\delta^{18}O_B]x[CO_B]+[\delta^{18}O_C]x[CO_C]+[\delta^{18}O_D]x[CO_D]$$
$$+[\delta^{18}O_E]x[CO_E]+ [\delta^{18}O_F]x[CO_F]+[\delta^{18}O_G]x[CO_G] = [\delta^{18}O_T]x\ [CO_T] \quad , \quad (14)$$

where A, B and C represent the three major sources (methane oxidation, non-methane hydrocarbon oxidation and biomass burning, respectively) of CO in the remote Southern Hemisphere and D, E, F and G represent the minor sources (biogenic, fossil fuel, bio-fuel and oceanic emission, respectively) (figure 4.11). *T* represents total CO and is obtained from our ice core measurement. It should be noted that steady state conditions are assumed when using this model. This assumption is valid if you consider the timescale of our ice core record (~ years on average) and the short lifetime of CO (~3 months). We use these equations

combined with information on CO sources from the MOZART model to evaluate changes in CO source strengths over time.

MOZART-4 is a three-dimensional chemical transport model (Emmons et al., 2010). MOZART-4 has a tracer version and can used to calculate the contribution of each CO source to the concentration and isotope ratios in the modern Southern Hemisphere troposphere, particularly Antarctica (Park et al., 2015). The tracer version of MOZART contains simplified chemistry that focuses on the reactions related to CO. CO in the tracer version is tagged for $C^{16}O$ and $C^{18}O$ from each source including fossil fuel, biomass burning, methane oxidation, NMHC oxidation, biofuel, direct biogenic and oceanic emissions (figure 4.11). The CO tags are treated as artificial tracers in the model containing isotope and source information. The source inventories of $C^{16}O$ and $C^{18}O$ are separated based on the oxygen isotope source signatures and they are individually reacted and transported with different kinetic isotope effects. Figure 4.11 is the MOZART-4 simulation results showing the contribution of CO sources at Scott Base, Antarctica (77°51' S, 166°46' E) from April 1996 through December 31, 2004.

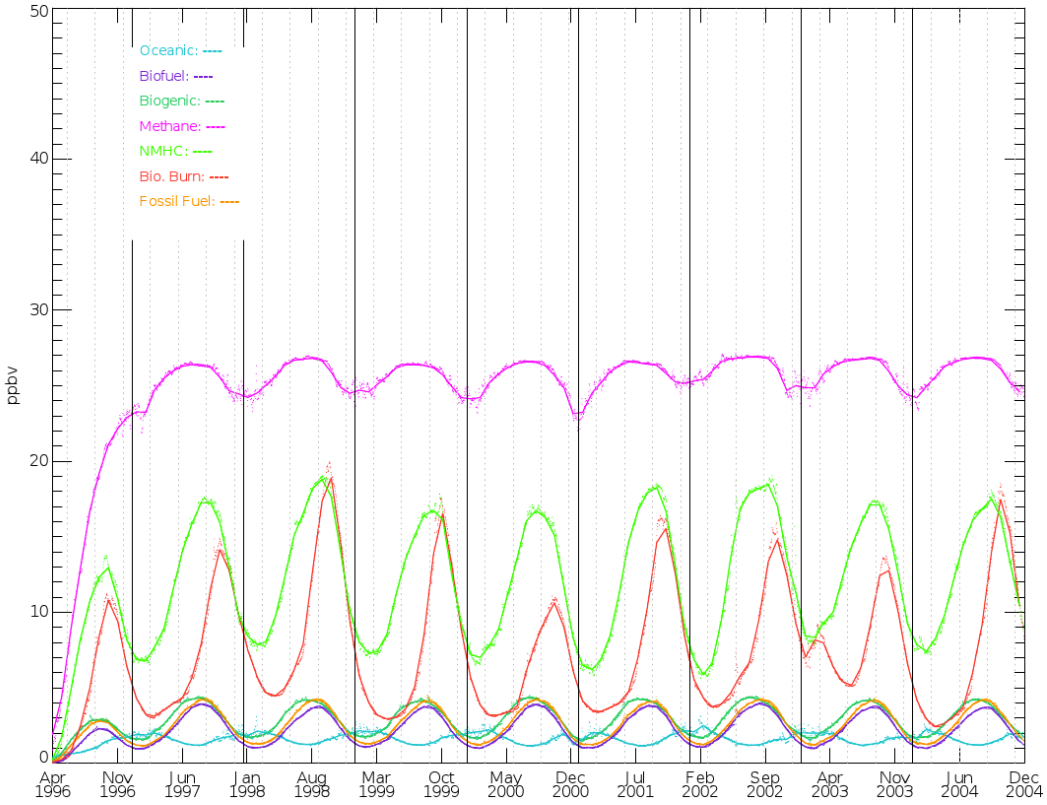

Figure 4.11: MOZART-4 simulation showing contribution of CO sources at Scott Base, Antarctica from April 1996 through December 31, 2004. Adapted from Park et al., 2015.

For the purposes of this study, we are simplifying equations 12-14 and are focusing on the major sources of CO (methane oxidation, NMHC oxidation and biomass burning). The other sources are minor contributors to the overall CO budget (figure 4.11). Some minor sources like oceanic emissions are thought to be constant over our sampling period. More specifically, the contribution from oceans to total CO emissions in the modern Antarctic troposphere is 2.7% based on model simulations (Park et al., 2015) (figure 4.11). As far as our CO budget is

concerned we are assuming the oceanic CO source remained fairly stable during the 250-year sample period. This stems from the idea that CO emission from the ocean is driven by the photochemical oxidation of dissolved organic matter (DOM) and (Bauer et al., 1980; Conrad and Seiler, 1980) and the intensity of solar radiation (Nakagawa et al., 2004; Seiler, 1974). Furthermore, it has been reported that the essential nutrient phosphorous in the Southern Ocean, which can be used as a proxy for ocean productivity, has remained in stable supply over the past 250 years (Filippelli et al., 2007). In addition, solar radiation is considered to be stable for the sample time period as well (Bard et al., 2000). Presently, MOZART estimates [CO] from the ocean source at Scott Base as 1.5 ppbv when the overall mixing ratio is 55.4 ppbv. The other minor sources could have changed over time, especially fossil fuel combustion, but are not explored here, since their contribution to the overall CO budget is small (figure 4.11). Below I discuss the contribution from the major CO sources.

4.4.2. Methane isotope contribution

The contribution of CO from methane (figure 4.8) can be accurately calculated because the concentration and isotope record is well known (figure 4.7, Etheridge et al., 1998), as are the CH_4-OH reaction kinetics. We use the known concentration and record of CH_4 concentrations from Law Dome (Etheridge et al., 1998) and the $\delta^{13}C_{CH4}$ record from Ferretti et al. (2005) (figure 4.12) and a

simplified version of equation 13 to account for the contribution of methane to CO:

$$[\delta^{13}C_T]x[CO_T]= [\delta^{13}C_{CH4}]x[CO_{CH4}]+[\delta^{13}C_r]x[CO_r] \quad (15)$$

$[\delta^{13}C_T]$ and $[CO_T]$ are from the ice core observations, $[\delta^{13}C_{CH4}]$ and $[CO_{CH4}]$ have been previously measured ((Ferretti et al., 2005) (figure 4.12) (Etheridge et al., 1998) (figure 4.4)). *r* is the residual (all non-methane CO sources) and $[CO_r]$ was calculated (figure 4.7) leaving the only unknown $[\delta^{13}C_r]$. Subtracting the residual from our observations, we obtain the remaining CO from other sources and the aggregate isotopic signature. This component is termed the 'residual' CO, or the methane corrected CO. Residual CO comprises all the sources of CO except for methane. This is done for both $\delta^{13}C$ and $\delta^{18}O$. $\delta^{18}O_{CH4}$ is assumed to be 0 ‰, consistent with previous studies (Brenninkmeijer 1993; Brenninkmeijer and Röckmann, 1999). However, it is noted that this value has never actually been measured in the laboratory. Residual CO, $\delta^{13}C$, and $\delta^{18}O$ are shown in figure 4.13 and 4.14.

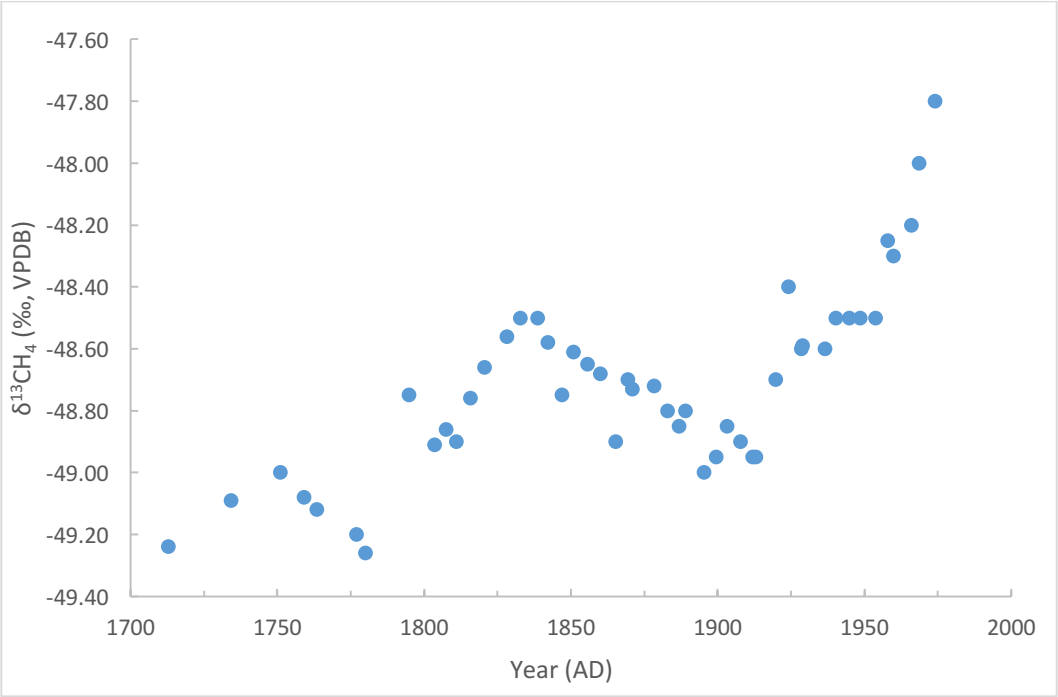

Figure 4.12: Law Dome, Antarctica record of $\delta^{13}C_{CH4}$ (‰, VPDB) (uncertainty ± 0.2 ‰). From Ferretti et al., 2005.

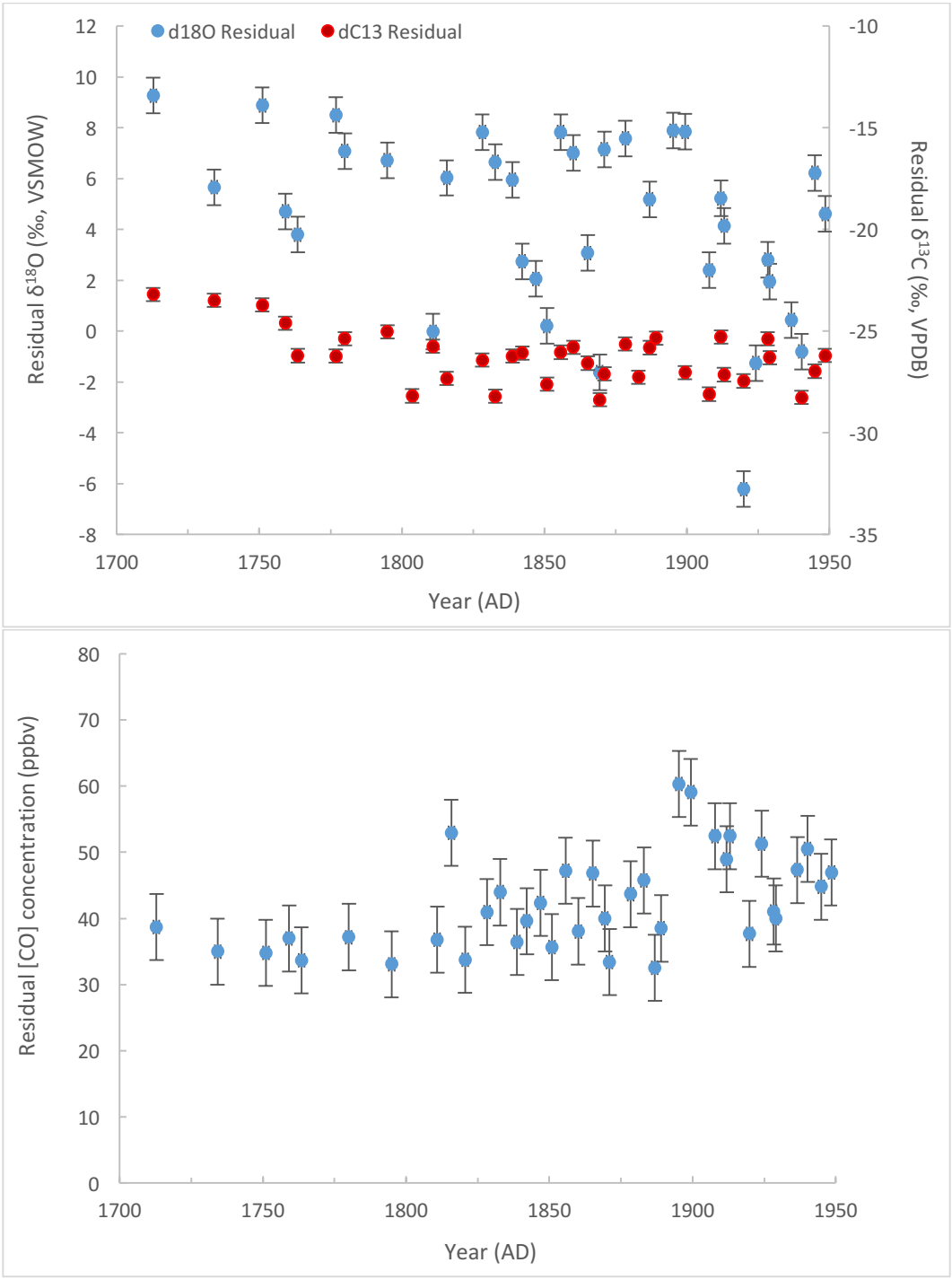

Figure 4.13: Top panel: residual $\delta^{13}C$ of CO (‰, VPDB) (right scale, red circles)

and residual $\delta^{18}O$ of CO (‰, VSMOW) (left scale, blue circles). Bottom panel: residual [CO] concentration (ppbv).

4.4.3 Residual $\delta^{13}C$ and $\delta^{18}O$ CO 1700-1900

The residual CO data are binned into ten-year time slices facilitating the visualization of interdecadal trends (figure 4.14). Figure 4.14 shows the CO data binned and the open markers represent a bin that only had 1 data point. All other bins had 2-3 data points. The residual $\delta^{13}C$ CO data (figure 4.13 and figure 4.14, top panel, orange circles) show a trend of more negative $\delta^{13}C$ values over most of the 19th century with a 4‰ decrease from from 1700-1900. In general, more negative $\delta^{13}C$ sources are going to be indicative of relatively greater amounts of NMHC oxidation (table 4.1). However as can be seen in table 4.1, $\delta^{13}C$ of NMHC oxidation varies significantly with what species is being oxidized (Huang et al., 2001). Also, the kinetic isotope effect for NMHC + OH exhibits a large range of values, depending on the stability of the alkyl radical that is produced thus depending on both the size and structure of the alkyl group(Rudolph et al., 2000). However, more complex oxidation pathways likely result in greater isotopic fractionation resulting in a more depleted ^{13}C (Rudolph et al., 2000). In our analysis we assume an average $\delta^{13}C_{NMHC}$ signature of -32.2‰ (Tsunogai et al., 2002).

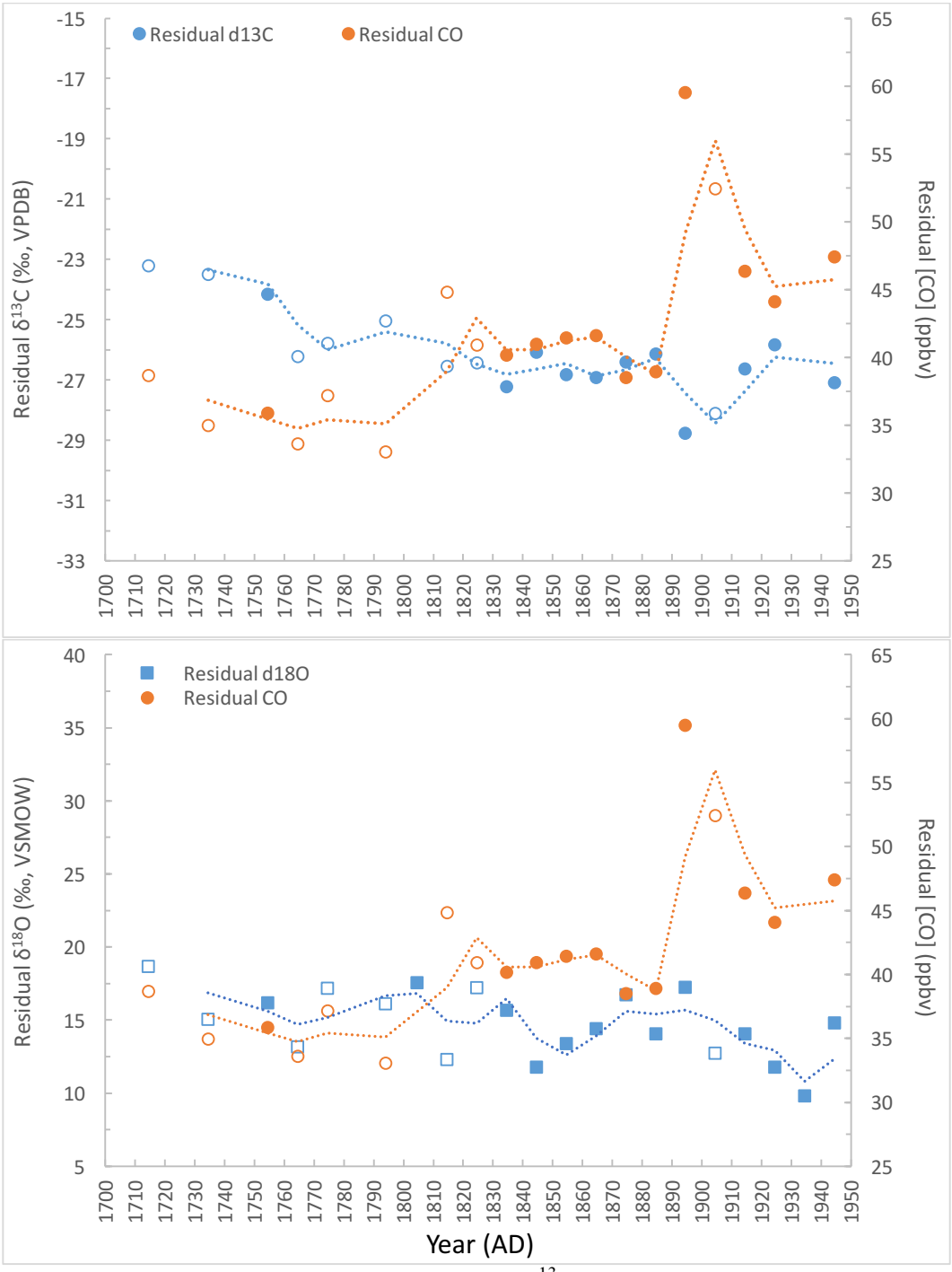

Figure 4.14: Decadal binning of residual $\delta^{13}C$ (‰, VPDB) (top panel, blue circles), $\delta^{18}O$ (‰, SMOW) (bottom panel, blue squares) and residual CO

concentration (ppbv) (orange circles). The dashed line is a 2 point moving average.

The residual $\delta^{13}C$ signature is also going to be dependent on the burned C3/C4 plant ratio which is known to vary considerably both spatially and temporally. Generally speaking, the enriched sources in $\delta^{13}C$ are going to be biomass burning, especially C4 savannah grasses (table 4.1). C4 savanna grasses burning results in a $\delta^{13}C$ of about -12‰ to -15‰ versus -28‰ to -32‰ for C3 plants, because of isotopic discrimination that occurs during carbon assimilation due to the different photosynthetic pathways among C3 and C4 plants (Farquhar et al., 1982) (table 4.1). A trend to more depleted $\delta^{13}CO$ from 1700-1900 is indicative of a relatively larger source from NMHC oxidation and/or a shift from burning C4 grasses to burning C3 plants, not to mention the vast majority of species are C3 type. The residual $\delta^{18}O$ for this time does show variability but the overall trend is flat. Since we see an increase in concentration while there is no observable trend in $\delta^{18}O$ but there is one for $\delta^{13}C$ (becomes depleted), we conclude that NMHC oxidation changed during this time since the only aspect differentiating CO from biomass burning and that from NMHC oxidation is the $\delta^{18}O$ signature (table 4.2). This conclusion is hard to quantify because there are many different NMHC species with different lifetimes and varying spatial distribution. This isotope data is not consistent with the only other published data available by Wang et al. (2010) (figure 4.15). Figure 4.15 presents a comparison of the residual data from this

study (blue circles) and the Wang et al. (2010) study (orange circles). Residual CO concentration is shown in the top panel, residual $\delta^{13}C$ (‰, VBDB) is the middle panel and residual $\delta^{18}O$ (‰, VSMOW) is the bottom panel.

Table 4.1: MOZART-4 simulation of $\delta^{13}C$ isotopic ratio at Scott Base (From Park et al., 2015).

CO Source	Source $\delta^{13}C$ (‰)	$\delta^{13}C$ at Scott Base (‰)
Biomass Burning	-25[1]; -12[2]	-21[3]; -9[3]
CH_4 Oxidation	-49	-48
NMHC Oxidation	A	-27[4]
Ocean	-25	-23.5
Biogenic	-25[1]; -12[2]	-25

Notes: [1]: forest burning (C3); [2]: savanna burning (C4); [3]: estimated based on C3 (-21‰) and C4 (-9‰) burning (L. Emmons, personal communication, 2015); [4]: based on $\delta^{13}C$ signature of NMHC oxidation (Stevens and Wagner, 1989) and ~ 4‰ KIE of CO + OH reaction (Stevens et al., 1980); A: $\delta^{13}C$ has been assigned to different organic compounds (L. Emmons, personal communication, 2015). Other $\delta^{13}C$ values are from L. Emmons, personal communication, 2015.

Table 4.2: MOZART-4 simulations of CO at Scott base from 1996-2004 (Park et al. 2015).

Source	[CO] Source	Source $\delta^{18}O$ (‰)[a]	$\delta^{18}O$ at Scott Base (‰)[b]
Oceanic	1.5	15	9.2
Biofuel	2.3	17.5	0.6
Biogenic	3	0	-10.5
Methane	25	0	-9.4
NMHC	13	0	-11.8
Biomass burning	8	17.5	5.3
Fossil fuel	2.6	23.5	9.3

[a]: These are original $\delta^{18}O$ signatures used for each type of emission in the model, references are the same as Table 2.1 in Chapter 2, and biofuel can be combined to biomass burning and its $\delta^{18}O$ signature is thus considered the same as that for biomass burning; [b]: $\delta^{18}O$ at Scott Base is the isotopic ratio calculated in the model based on the ratio between $[C^{16}O]$ and $[C^{18}O]$ at Scott Base. From Park et al., (2015).

In their work, Wang et al. (2010) observed an enrichment in residual $\delta^{13}C$ of ~3‰ (even though there is some variability in their record) and residual $\delta^{18}O$ became enriched by ~5‰ while residual concentration increased ~10 ppbv from 1700-1900. Wang et al. (2010) attributed the increase in CO and enrichment of $\delta^{18}O$ to an increase in biomass burning. While this new record only extends back to 1700, the Wang et al. record goes back to 1350 AD and shows an unexpected high CO concentration before industrialization, which was again attributed to a greater contribution from biomass burning with supporting evidence from an enrichment in $\delta^{18}O$. Van der Werf et al. (2013) were not able reconcile model and absolute values of the Wang et al. (2010) study. Those authors reported that in order to get the model to reproduce the ice core CO concentrations, all savannas in the Southern Hemisphere had to burn annually at a time where population density was lower. Van der Werf et al. (2013) concluded that while this is scenario is possible, it is highly unlikely. Our calculated residual CO from WAIS Divide is consistent with that reported in Wang et al. from 1700 - 1890 AD (top panel figure 4.15). However in the late 1890s, the two records diverge significantly. Compared with the decades prior, we observe 5 individual ice core samples with significantly higher CO (and therefore residual CO) concentrations. For the same time period, Wang et al. reported 20 ppbv less residual CO than our data. After 1900, we observe a decreasing concentration trend in CO and residual CO for 40 years. Compared to present day residual CO (shown in figure 4.15 as a

horizontal line), we see our samples yield 20%-100% more residual CO than present day.

Our residual $\delta^{13}C$ from WAIS Divide is consistent with Wang et al. for the earlier parts of our record, until about 1750. After that, the two records diverge continuously. In contrast to this, our residual $\delta^{18}O$ is enriched compared to Wang et al. in the beginning of the 18th century and then remains scattered but consistent over the subsequent centuries, while the Wang et al. record converges (becomes more enriched). We don't see a direct correlation between concentration and $\delta^{18}O$, however that is because $\delta^{18}O$ is enriched throughout the entire period of measurement. Any additional CO, even if it were from a source enriched in $C^{18}O$, such as biomass burning, would not result in a large accompanying increase in $\delta^{18}O$. Furthermore, the new data suggests that the relative proportion of biomass burning to NMHC must have changed over this time.

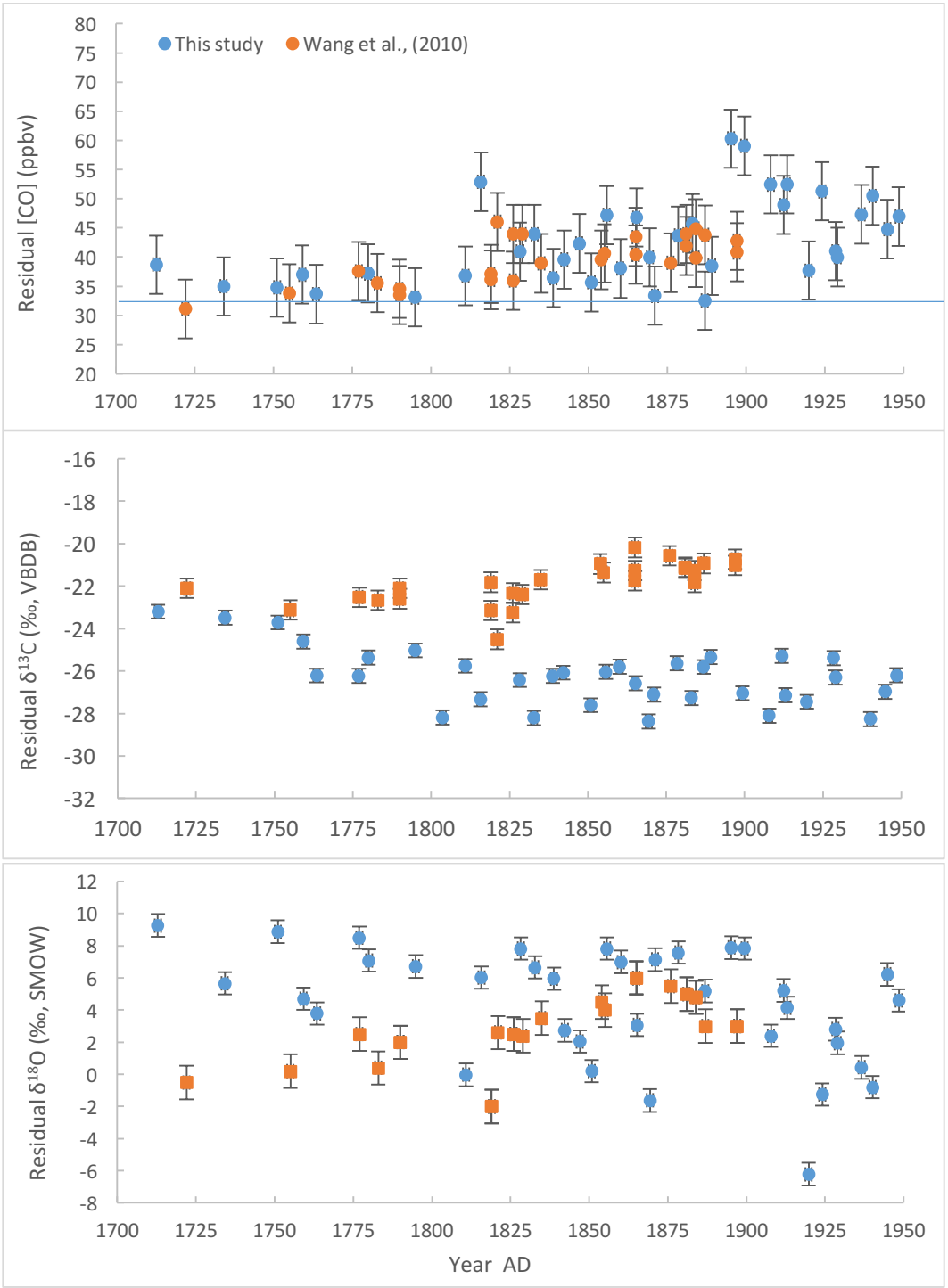

Figure 4.15: Residual CO (top panel), residual $\delta^{13}C$ (‰, VBDB) (middle panel) and residual $\delta^{18}O$ (‰, VSMOW) (bottom panel) from this study (blue circles) and

from Wang et al. (2010) (orange squares). The blue horizontal line (top panel) is present day residual [CO] from MOZART, for comparison.

4.4.4 Residual $\delta^{13}C$ and $\delta^{18}O$ CO 1900-1950

For the time period of the new data (1900-1950), there is an anti-correlation between $\delta^{13}C$ and CO concentration (figure 4.16). At the turn of the century, $\delta^{13}C$ shows a depletion of ~ 2 ‰ while concentrations increased by ~15 ppbv. From 1905-1925, $\delta^{13}C$ shows an enrichment of ~2 ‰ while CO concentration decreases ~10 ppbv. Then from 1925-1950, $\delta^{13}C$ shows another depletion of ~1.24 ‰ while concentration increased by 3.3 ppbv. On the other hand, post 1900, $\delta^{18}O$ and CO concentration are correlated (figure 4.14). From ~1905 to 1925 residual $\delta^{18}O$ shows a depletion of ~5 ‰ while concentration decreases to ~10 ppbv. Overall, the $\delta^{18}O$ from 1900-1950 shows a slight depletion which is supported by the charcoal record. There are hardly any records to compare our data set to so even though the charcoal record is not without limitations as discussed in Chapter 1, it can be helpful in our analysis. Powers et al. (2010) reports a charcoal record from Southern South America (SSA) which shows a decline at the same time ~1900-1930. Antarctic locations are far more sensitive to CO emissions from Southern South America and Australia/New Zealand relative to Africa (Van Der Warf et al., 2013). Furthermore, Marlon et al. (2013) has a record from New Zealand that reveals a downturn in burning in New Zealand for this same time. The fact that

these records show a decline in charcoal adds some supporting evidence that the decrease we observe in both concentration and $\delta^{18}O$ could be from a reduction in biomass burning from locations in the Southern Hemisphere that are known to effect the CO budget in Antarctica. However, we cannot rule out that the variation we are seeing in CO concentration could be from a change in NMHC oxidation as these two records mirror each other (figure 4.16). It is possible that the vegetative coverage changed which would impact the littler load and have a direct effect on the isotopes.

The new $\delta^{18}O$ isotope data reveals that there was the same relative proportion of biomass burning over time regardless of residual concentration. This tells us that the contribution from biomass burning has been constant. There is some overlap of the $\delta^{18}O$ values with Wang et al. (2010) and considerable overlap with residual CO concentration (figure 4.15). For the data point at 1874, our $\delta^{18}O$ is enriched relative to Wang et al. (2010) but then both records start to show a depletion at the turn of the 20th century. The Wang et al. (2010) record ends and the WAIS Divide record continues the trend of depletion into the early 20th century. Overall, the new $\delta^{18}O$ values are variable but are clearly dominated by biomass burning as indicated from the observed enrichment of the oxygen isotope.

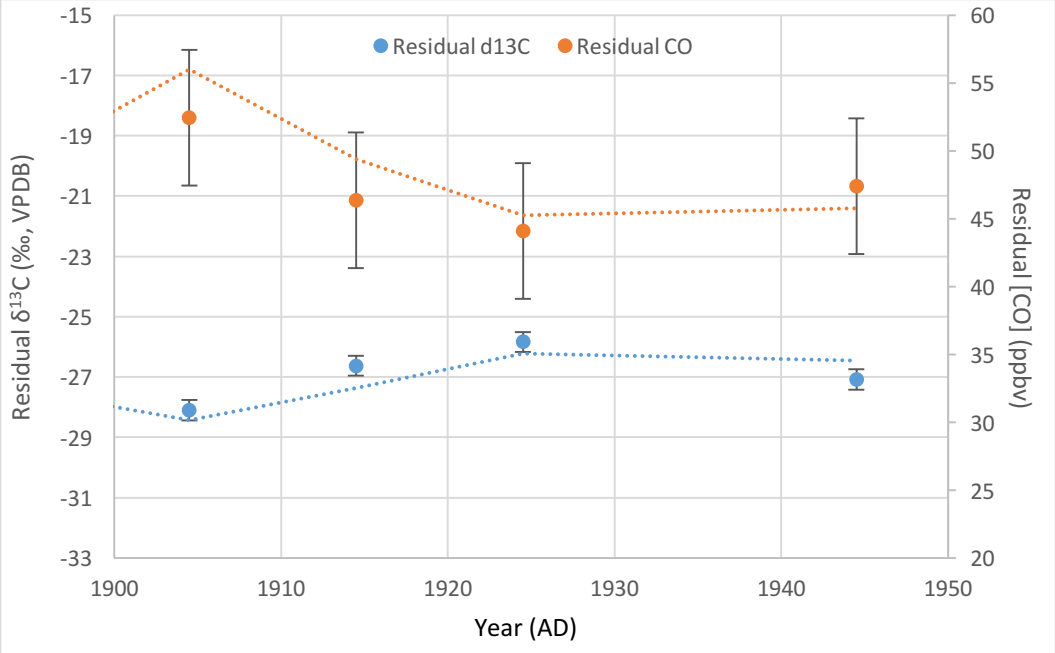

4.16: Residual CO (orange circles) and residual $\delta^{13}C$ (‰, VBDB) (blue circles) from this study for 1900-1950. The line is a 2 variable moving average.

In summary, there are large variations of residual [CO], residual $\delta^{13}C$ and residual $\delta^{18}O$ over the last 250 years which suggests there was a change in the two primary non-methane CO sources which drove these variations of atmospheric CO. Overall, our CO concentration record increases over time and our analysis is constrained by the isotopes.

4.4.5 CO partitioning based on an isotopic mass balance model

In order to better understand the evolution of the two main sources of CO and quantify their contribution we used the mass balance model calculated residual

$\delta^{18}O$ (figure 4.7) and assign $\delta^{18}O$ signatures according to table 4.2 to solve equation 12 and 14. Equation 12 in this case is simplified to the two unknown major sources of [CO] residual, $[CO]_{\text{biomass burning}}$ and $[CO]_{NMHC}$:

$$[CO_r] = [CO_{NMHC}]+[CO_{\text{Biomass burning}}] \quad (16)$$

Equation 14 simplifies to:

$$[\delta^{18}O_r]x[CO_r] = [\delta^{18}O_{NMHC}]x[CO_{NMHC}]+[\delta^{18}O_{\text{Biomass burning}}]x[CO_{\text{Biomass burning}}] \quad (17)$$

This is an oversimplification and several assumptions are made. For example, we are assuming oceanic emissions stayed constant and are not considering this minor emission. Also not considered are the other minor sources of CO including fossil fuel, biofuel and biogenic emissions and how they could have changed over time. These minor sources contribute 2.6, 2.3 and 3.0 ppbv, respectively to the present day modeled CO budget at Scott Base (Park et al., 2015). In addition, there is an uncertainty associated with assigning isotopic signatures in equation 17. It is possible the signature changed over time but this cannot be quantified (Schaefer and Whiticar, 2008). Also, there is a large range in the $\delta^{18}O$ signature dependent on temperature and fuel load type (Kato et al., 1998; Chapter 2). It is very difficult to assign a $\delta^{18}O$ signature because of the different composition of plant material as well as not knowing how much is coming from smoldering (low temperature) versus open flame burning. For example, if plant material has

oxygen that is enriched at 30 ‰, once it burns that value will decrease but can still be higher than atmospheric oxygen (23.5 ‰) (Kato et al., 1998). For this reason, two scenarios were modeled/calculated/performed in which we take a range of the isotopic signature for $\delta^{18}O$ from 17.5 to 23.5 (Chapter 2, table 2.2). There is also uncertainty with assigning $\delta^{18}O$ signatures for methane and NMHC oxidation. Unlike biomass burning there are no direct measurements for $\delta^{18}O$ from methane and NMHC oxidation. The community uses an accepted signature of 0‰ (Brenninkmeijer and Röckmann, 1997). It should be noted that if this signature was not zero than our whole mass balance model would change. Unfortunately, no uncertainty can be assigned to this component and this reflects an obvious weakness in the analysis. The results are presented in figure 4.17 and show modeled CO source partitioning based on ice core observations and mass balance model for methane derived CO (top panel), NMHC derived CO (middle panel) and biomass burning derived CO (bottom panel). In scenario 1, 17.5‰ is assigned as the $\delta^{18}O$ signature (blue circles) and in scenario 2, 23.5 ‰ is assigned for the isotopic signature of $\delta^{18}O$. Also shown is [CO] derived from the three main sources of CO present day at Scott Base, based on MOZART-4 model simulation (orange square) (Park et al., 2015). The results show that the CO derived from methane was constant from 1700-1800, followed by a slight increase from ~11.3-13.3 ppbv during the subsequent century and then increased significantly at the turn of the 20th century with a ~4.1 ppbv increase to ~17.4

ppbv in just 50 years followed by a rapid increase from 1950 to 2000 to a present day contribution of ~26 ppbv (figure 4.17 top panel). The rapid increase from 1900-2000 can be explained in terms of excess anthropogenic emissions of methane during this time (Etheridge et al., 1998). Prior to 1900 it is evident that methane emission did not significantly impact the CO budget due to the stability of the record.

The biomass burning derived record shows considerable variability throughout the record but always contributes a significant amount to the overall budget (figure 4.17 bottom panel). Of particular interest is the decline from 1900-1950. The data point at 1944 could possibly be contaminated due to its close proximity to the close-off and the increase observed is not considered reliable. This finding is in agreement with the charcoal index present by Marlon et al. (2008) and Powers et al. (2012). The decline in biomass burning from 1900-1950 would also help explain the low contribution in today's modeled budget. Biomass burning derived from CO that makes it way to Antarctica mostly originates from the Southern Hemisphere tropics (Park et al., 2015). These findings support the idea that biomass burning must have change drastically from 1900 on. What exactly caused this change can be debated. As an example, the cause could be due to climatic change, land use changes (i.e., changing fire prescribing) or population. The fact that the literature shows a strong decline in the sedimentary charcoal index from the Southern Hemisphere tropics gives more confidence to

the findings of the new CO concentrations from 1900-1950. To speculate on a likely cause of the biomass burning decline of the 1900 we can look at the land use change. With an increasing population and a greater demand for food, there was a widespread clearing of native vegetative cover to introduce land for grazing animals (Goldewijk, 2001; Pongratz et al., 2008; Savage and Swetnam, 1990). The destruction of the native canopy could provide an explanation for the decrease in biomass burning derived CO that is observed.

As for the NMHC derived CO, there is a lot of uncertainty with this measurement. The data support that there was less of a contribution to the overall CO budget earlier in the record (figure 4.17, middle panel) and then its contribution steadily increased. There does appear to be some decadal variability. An increased contribution of NMHC derived CO over time is supported by the present day modeled contribution of Scott Base of ~13 ppbv. The NMHC oxidation contribution is difficult to quantify because the lifetime of these gases are short and present in low concentration. Also, as discussed above, non-methane hydrocarbons exhibit varying kinetic isotope effects when reacting with OH which adds another dimension of complexity to the analysis. For that reason, the biomass burning derived CO analysis is likely more significant for interpretation of the underlying cause.

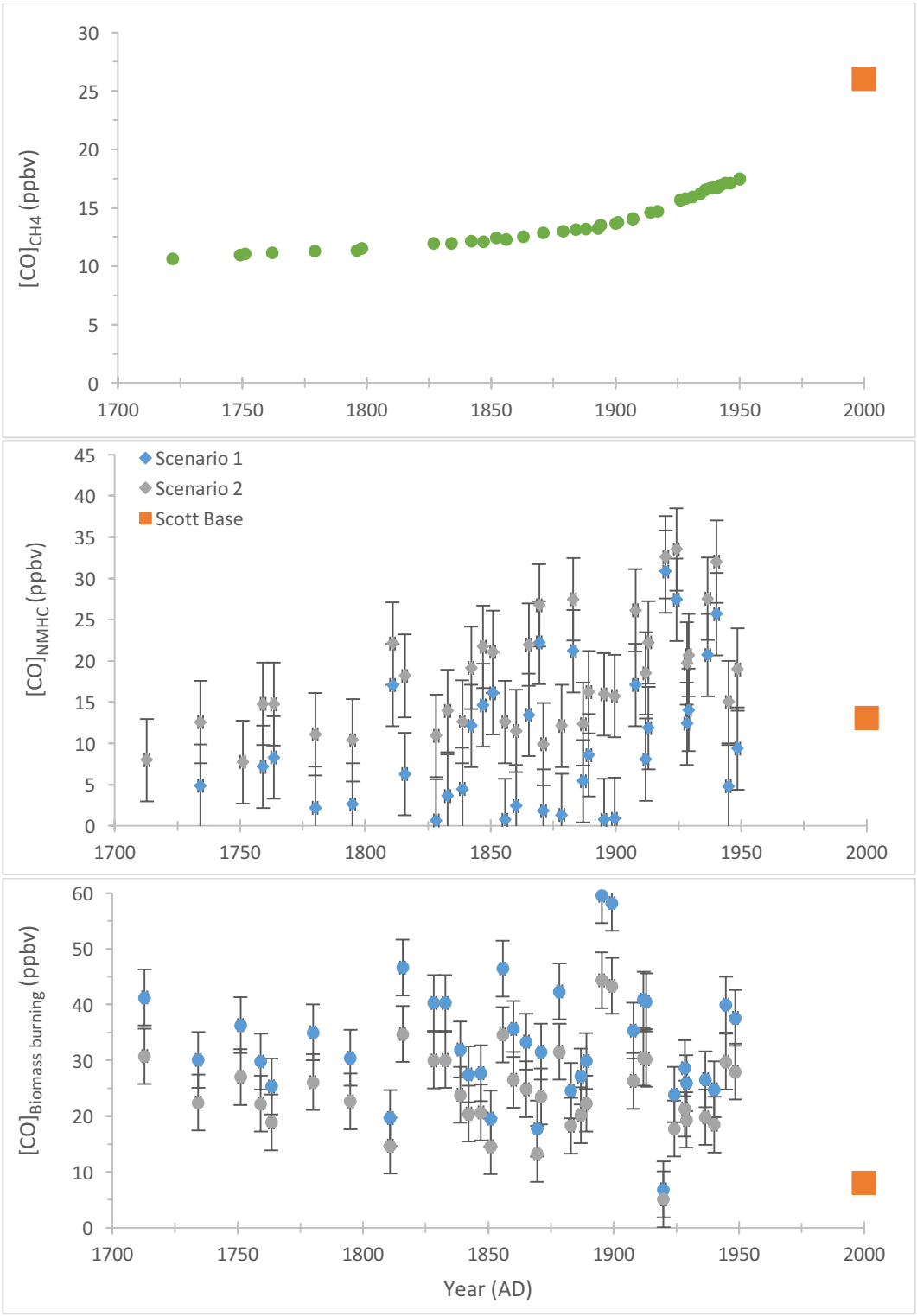
[CO]CH4 (ppbv)
30
25
20
15
10
5
0
1700
1750
1800
1850
1900
1950
2000
[CO]NMHC (ppbv)
Scenario 1
Scenario 2
Scott Base
45
40
35
30
25
20
15
10
5
0
[CO]Biomass burning (ppbv)
60
50
40
30
20
10
0
Year (AD)

Figure 4.17: Modeled CO source partitioning based on ice core observations and mass balance model. In scenario 1, 17.5‰ is assigned for the $\delta^{18}O$ biomass burning signature (blue circles) and in scenario 2, 23.5‰ is assigned for the $\delta^{18}O$ signature. The [CO] derived from methane, NMHC and biomass burning from 2000 AD at Scott Base, Antarctica, calculated from the MOZART-4 model simulation are also shown (orange square) (Park et al., 2015).

5 Conclusions and outlook

The work presented here extends the record of CO concentration and its isotopes to 1950 AD. CO is of importance because of its pivotal role in tropospheric chemistry, particularly its impact on hydroxyl radical abundance. Furthermore, the historic variations in sources of CO, which are primarily biomass burning and hydrocarbon oxidation, can help to shed light on how atmospheric conditions have changed in the past. CO concentration coupled with its stable isotopic composition are excellent tracers of the relative source strengths. There is currently little knowledge on how CO and its isotopes have varied through time and this work helped to fill the spatial gaps. The conclusions from this work are presented below:

1. Atmospheric [CO] was constant ~48 ppbv (±5ppbv) from 1700 - 1820 AD and then exhibited variability and an overall increase to ~55 ppbv (±5ppbv) from 1820-1900 AD. At the beginning of the 20th century there is a spike in the record and then a decrease and a subsequent increase. The last decade of the record shows a gradual decline. In general, these new data show that CO concentration over the past 250 years deviated from modern measurements indicating a change in the relative contribution from different CO sources.

2. $\delta^{13}C_{CO}$ shows a negative trend with time (becoming isotopically depleted) by about 4‰ from the 1700s to the mid-1900s. On the other hand, $\delta^{18}O$ of CO (with respect to V-SMOW), is more variable with no immediately observable trend. It is assumed the observed variability in $\delta^{18}O$ is a measurement of the temporally varying change in relative sources and sinks of CO, and that the temporal variations are observable because of the high accumulation rate at the WAIS D site. Overall, the new $\delta^{18}O$ values (1900 - 1950 AD) are variable but are clearly dominated by biomass burning as indicated from the observed enrichment of the oxygen isotope.
3. Residual data on concentration and isotopes coupled with modeled CO source partitioning reveals that biomass burning was always a significant contributor to the overall CO budget in Antarctica. There is a marked decline from 1900-1950 which is supported by the charcoal index and could help explain the present day low contribution of biomass burning.

5.1 Outlooks and future work

The future of this field is rather exciting. Since this work presents the first data from 1900 - 1950 and there are no records to compare it to, it would be beneficial to process replicate samples from a different borehole at WAIS Divide as well as samples from other sites that could provide a comparable high resolution record. It would then be interesting to see if MOZART can reproduce this new record and

potentially help reveal the underlying processes governing the biomass burning component of the CO budget. Another area that should be explored is the contribution of the minor sources of CO. The minor sources make up ~17% of the total CO budget at Scott Base presently, so looking into how these sources evolved is of importance.

A shortcoming of this work is the uncertainty associated with the dating of the gas. This is area where more research should be done. For example, the models used to estimate the mean gas age have an uncertainty associated with them but this has not been quantified. For example, different firn diffusion models vary in how they correct for temperature and pressure and use overall different numerical codes (e.g. Trudinger, et al., 2002; Schwander et al., 1993; Mischler et al., 2009 and Mitchell et al., 2011). As described in Chapter 2, firn is a multi-dimensional layer where many factors can change on a year to year basis such as density, porosity, accumulation rate, etc. These variables are not captured in the models and it is unknown how this effects the reconstruction of CO, a gas that exhibits seasonality (Chapter 1). Also, a model that investigates the age distribution of the gas at depth needs to be developed. This will allow us to infer which percentage of the sample is actually from that year and which percentage is due to older and younger time periods. For this reason, an effort should be made to investigate the uncertainty in current models and develop new models for age distribution.

Since a major conclusion of this work is biomass burning was a significant contributor to the measured CO concentration, the spatial and temporal evolution of biomass burning should be investigated further. One way to accomplish this is through modeling. van der Werf et al. (2013) employed a model that reproduced the CO mixing ratios from South Pole (Wang et al., 2010) by combining contemporary landscape fire emissions and a chemical transport model. Running such a model can help understand the evolution of biomass burning. In particular, it reveals what regions of the hemisphere were burnt which can lead to clues to how the relationship between people and the Earth system changed over time.

There should also be a detailed investigation into other mechanisms of CO concentration change over time. For example, could changes in atmospheric circulation or long term variations in OH concentrations be responsible for the structure we observe in the record? To investigate possible changes in OH concentrations via ice you could measure $\Delta^{17}O$ (^{17}O excess) of CO. $\Delta^{17}O$ can be used because it doesn't follow a common pattern during the CO + OH removal reaction, it follows a mass independent fractionation (Chapter 2) and should be observable in the isotope record (Röckmann et al., 1998). Overall, there is plenty of work that can be conducted in the field. Specifically, CO is an excellent tracer for biomass burning so any future studies that are interested in biomass burning will greatly benefit from having an accurate record of CO. Therefore, the concentration record of CO should be extended as far back in time as the ice

permits.

References

Alley R.B., Marotzke J., Nordhaus W.D., Overpeck J.T., Peteet D.M., Pielke R.A. Jr, Pierrehumbert R.T., Rhines P.B., Stocker T.F., Talley L.D., Wallace J.M. (2009), Abrupt climate change. Science 292:2005–2010. doi:10.1126/science.1081056

Ahn, J. et al. (2012), Atmospheric CO_2 over the last 1000 years: a high-resolution record from the West Antarctic Ice Sheet (WAIS) divide ice core. Glob. Biogeochem. Cycles 26, GB2027.

Andreae, M., and Merlet, P. (2001), Emission of trace gases and aerosols from biomass burning, Biogeo Cycles, 15, 4, 955–966.

Assonov, S. S., Brenninkmeijer, C.A.M., Jockel, P.J., Mulvaney, R., Bernard,S., and Chappellaz, J. (2007), Evidence for a CO increase in the SH during the 20th century based on firn air samples from Berkner Island, Antarctica, Atmospheric Chemistry and Physics, 7, 295-308.

Atkinsion, R. (2003), Kinetics of the gas-phase reactions of OH radicals with alkanes and cycloalkanes Atmos. Chem. Phys., 3, 2233 –2307.

Aydin, M., J. E. Campbell, T. J. Fudge, K. M. Cuffey, M. R. Nicewonger, K. R. Verhulst, and E. S. Saltzman (2016), Changes in atmospheric carbonyl sulfide over the last 54,000 years inferred from measurements in Antarctic ice cores, J. Geophys. Res. Atmos., 121, 1943–1954, doi:10.1002/2015JD024235.

Aydin, M., Montzka, S.A., Battle, M.O., Williams, M.B., De Bruyn4, W.J., Butler J.H., Verhulst, K.R., Tatum, C., Gun, B.K., Plotkin, D.A., Hall B.D. and Saltzman E.S. (2010), Post-coring entrapment of modern air in some shallow ice cores collected near the firn-ice transition: evidence from CFC-12 measurements in Antarctic firn air and ice cores. Atmos. Chem. Phys., 10, 5135–5144.

Aydin, M., Williams, M. B., Tatum, C., and Saltzman, E. S. (2008), Carbonyl sulfide in air extracted from a South Pole ice core: a 2000 year record, Atmos. Chem. Phys., 8, 7533–7542, doi:10.5194/acp-8-7533-2008.

Ayers et al., (1992), Evidence for photochemical control of ozone concentrations in unpolluted marine air. Nature 360, 446 - 449.

Battle, M.O., Severinghaus, J.P., Sofen E.D., Plotkin, D, Orsi, A.J., Aydin, M., Montzka, S.A., Sowers, T., and Tans, P.P. (2011), Controls on the movement and composition of firn air at the West Antarctic Ice Sheet Divide Atmos. Chem. Phys., 11, 11007–11021.

Bauer, K., Conrad, R. and Seiler, W. (1980), Photo-oxidative production of carbon monoxide by phototropic mocroorganisms, Biochimica Et Biophysica Acta, 589(1), 46-55.

Bergamaschi, P., Hein, R., Brenninkmeijer, C. A. M. and Crutzen, P. J. (2000), Inverse modeling of the global CO cycle: 2. Inversion of $^{13}C/^{12}C$ and $^{18}O/^{16}O$ isotope ratios. Journal of Geophysical Research 105.

Bisiaux, M. M., McConnell, J. R., Pasteris, D. R., Taylor, K. C., Edwards, R., Penner, J. E., Curran, M., Van Ommen, T., Smith, A., Neumann (2012), Changes in black carbon deposition to Antarctica from two high-resolution ice core records, 1850-2000 AD, Atmospheric Chemistry and Physics, 12, (9), 4107-4115.

Bowman, D., et al., (2009), Fire in the Earth System, Science, 324, 5926, 481-484.

Brenninkmeijer, C.A.M. (1993), Measurement of the abundance of 14CO in the atmosphere and the 13C/12C and 18O/16O ratio of atmospheric co with applications in new zealand and Antarctica. J. Geophys. Res., 98, 10595–10614.

Brenninkmeijer, C.A.M., Röckmann, T. Principal factors determining the 18O/16O ratio of atmospheric CO as derived from observations in the southern hemispheric troposphere and lowermost stratosphere (1997), J. Geophys. Res. Atmos.,102, 25477–25485.

Brenninkmeijer, C.A.M., Röckmann, T., Bräunlich, M., Jöckel, P.; Bergamaschi, P. (1999) Review of progress in isotope studies of atmospheric carbon monoxide. Chemosphere Glob. Chang. Science, 1, 33–52.

Brook, E. (2009), Atmospheric carbon footprints, Nature Geoscience, 2, 170-172. Brook, E. J., Harder, S., Severinghaus, J., Steig, E. J., and Sucher, C. M., On the origin and timing of rapid changes in atmospheric methane during the last glacial period, Global Biogeochemical Cycles, 14(2), 559-572, 2000.

Cantrell, C., et al., Carbon kinetic isotope effect in the oxidation of methane by the hydroxyl radical, J. Geophys Res., 95, D13, 22455-22459, 1990.

Carcaillet, C., et al., (2002), Holocene biomass burning and global dynamics of the carbon cycle, Chemosphere, 49, 845-863.

Chappellaz, J., Blunier, T., Kints, S., Dallenbach, A., Barnola, J.-M., Schwander, J.,Raynaud, D., Stauffer, B., Changes in the atmospheric CH gradient between Greenland and Antarctica during the Holocene. Journal of Geophysical Research 102, 15,987–15,998, 1997.

Conny, J.M. (1999), The isotopic characterization of carbon monoxide in the troposphere. Atmos. Environ. 32, 2669–2683.

Conny, J.M., Verkouteren, R.M., Currie, L.A. (1997), Carbon 13 composition of tropospheric CO in Brazil: A model scenario during the biomass burn season. J. Geophys. Res. Atmos.102, 10,638–10,693

Conrad, R. (1989), Control of methane production in terrestrial ecosystems in exchange of trace gases between terrestrial ecosystems and the atmosphere, 39-58.

Conrad, R., Seiler, W., Bunse, G., Giehl, H. (1982), Carbon monoxide in seawater (Atlantic Ocean). J. Geophys. Res. 87, 8839–8852.

Crutzen, P. and Zimmermann, P. (1991), The changing photochemistry of the troposphere, Tellus B, 43, 136–151.

Dlugokencky, E. J., R. C. Myers, P. M. Lang, K. A. Masarie, A. M. Crotwell, K. W. Thoning, B. D. Hall, J. W. Elkins, and L. P. Steele (2005), Conversion of NOAA atmospheric dry air CH_4 mole fractions to a gravimetrically prepared standard scale, Journal of Geophysical Research-Atmospheres, 110(D18).

Duncan, B. N., Logan, J. A., Bey, I., Megretskaia, I. A., Yantosca, R. M., Novelli, P. C., Jones, N. B., and Rinsland, C. P. (2007), Global budget of CO, 1988-1997: Source estimates and validation with a global model, J. Geophys. Res. - Atmos., 112, D22301, doi:10.1029/2007JD008459.

Emiliani, C. (1955), Pleistocene temperatures. Journal of Geology, 63, 538–578.

Emmons, L.K., Walters, S., Hess, P.G., Lamarque, J.F., Pfister, G.G., Fillmore, D., Granier, C., Guenther, A., Kinnison, D., Laepple, T., et al. Description and evaluation of the model for ozone and related chemical tracers, version 4 (mozart-4). Geosci. Model Dev. 2010, 3, 43–67.

EPICA community members (2004), Eight glacial cycles from an Antarctic ice core. Nature, 429, 623-628.

Epstein, S., Buchsbaum, H. A., Lowenstam, H. A., & Urey, H. C. (1953), Revised carbonate-water isotopic temperature scale. Geological Society of America Bulletin, 64, 1315–1326.

Etheridge, D. M., L. P. Steele, R. J. Francey, and R. L. Langenfelds (1998), Atmospheric methane between 1000 AD and present: Evidence of anthropogenic emissions and climatic variability, Journal of Geophysical Research-Atmospheres, 103(D13), 15979-15993.

Faïn, X., Chappellaz, J., Rhodes, R.H., Stowasser, C., Blunier, T., McConnell, J.R., Brook E. J., Preunkert, S., Legrand, M., Debois T., and Romanini, D., (2014), High resolution measurements of carbon monoxide along a late Holocene Greenland ice core: evidence for in situ production, Climate of the Past, 10, 987–1000.

Feilberg, K. L., S. R. Sellevag, C. J. Nielsen, D. W. T. Griffith, and M. S. Johnson (2002), CO+OH -> CO_2+H: The relative reaction rate of five CO isotopologues, Phys. Chem. Chem. Phys., 4(19), 4687-4693.

Ferretti, D. F., Miller, J. B., White, J. W., Etheridge, D. M., Lassey, K. R., Lowe, D. C., MacFarling, C. M., Meure, M. F., Dreier, C. M., Trudinger, T. D., van Ommen, R. Langenfelds, Unexpected changes in the global methane budget over the last 2000 years, Science, 309, 1714-1717, 2005.

Finlayon-Pitts, B.J., and Pitts, J.N. Tropospheric Air Pollution: Ozone, Airborne Toxics, Polycyclic Aromatic Hydrocarbons, and Particles (1997), 276, 5315, 1045-1051, DOI: 10.1126/science.276.5315.1045.

Fischer, H., et al. (2008), Changing boreal methane sources and constant biomass burning during the last termination, Nature, 452, 864-867.

Flückiger J. et al. (2002), Global Biogeochem. Cycles, 16, 1010.

GLOBALVIEW-CO (2009), Cooperative Atmospheric Data Integration Project - Carbon Monoxide. CD-ROM, NOAA ESRL, Boulder, Colorado [Also available on Internet via anonymous FTP to aftp.cmdl.noaa.gov, Path: products/globalview/co].

Goericke, R., and B. Fry (1994), Variations of Marine Plankton δ13C with Latitude, Temperature, and Dissolved CO_2 in the World Ocean, Global Biogeochemical Cycles, 8(1), 85-90.

Gow, A.J. (1968), Deep core studies of the accumulation and densification of snow at Byrd Station and Little America V, Antarctica. CRREL Res. Rep. 197.

Haan, D. And Raynaud, D., (1998), Ice core record of CO variations during the last two millennia: atmospheric implications and chemical interactions within the Greenland ice. Tellus B, 50, 253–262.

Guenther, A., Geron, C., Pierce, T., Lamb, B., Harley, P., Fall, R. (2000), Natural emissions of non-methane volatile organic compounds; carbon monoxide, and oxides of nitrogen from North America. Atmos. Environ., 34, 2205–2230.

Guenther, P. I. Palmer, and P. J. Lawrence (2008), Contribution of isoprene to chemical budgets: A model tracer study with the NCAR CTM MOZART-4, Journal of Geophysical Research-Atmospheres, 113(D5).

Haan, D., Martinerie, P. and Raynaud, D. (1996), Ice core data of atmospheric carbon monoxide over Antarctica and Greenland during the last 200 years., Geophys Res. Lett., 23, 2235–2238.

Haan, D., and D. Raynaud (1998), Ice core record of CO variations during the last two millennia: atmospheric implications and chemical interactions within the Greenland ice, Tellus Series B-Chemical and Physical Meteorology, 50(3), 253-262.

Hallquist, M., Wenger, J.C., Baltensperger, U., Rudich, Y., Simpson,D., Claeys, M., Dommen, J., Donahue, N.M., George, C., Goldstein, A.H., Hamilton, J.F., Herrmann, H., Homann, T., Iinuma, Y., Jang, M., Jenkin, M.E., Jimenes, J.L, Kiendler-Scharr, A., Maenhaut, W., McFiggans, G., Mentel, T.F., Monod, A., Prevot, A. S. H., Seinfeld, J.H., Surratt, J.D., Szmigielski, R. and Wildt, J., (2009) Atmos. Chem. Phys., 9, 5155-5236.

Harrison, S. P., Marlon, J. R., Bartlein, P. J., (2010) Fire in the Earth system. In: Dodson, J. (Ed.), Changing Climates, Earth Systems and Society. Springer, Dordrecht, The Netherlands, pp. 21 e48.

Holloway, T., H. Levy II, and P. Kasibhatla (2000), Global distribution of carbon monoxide, J. Geophys. Res., 105, 12,123– 12,147.

Huang Y., et al. (2001), Climate change as the dominant control on glacial-interglacial variations in C3 and C4 plant abundance. Science, 293, 1647.

IPCC (2007), Climate Change 2007: The Physical Science Basis. Contribution of Working Group I to the Fourth Assessment Report of the Intergovernmental Panel on Climate Change [Solomon, S., D. Qin, M. Manning, Z. Chen, M. Marquis, K.B. Averyt, M.Tignor and H.L. Miller (eds.)], Cambridge University Press, Cambridge, United Kingdom and New York, NY, USA.

IPCC-SAR (1996), Climate Change 1995: The Science of Climate Change. Contribution of Working Group I to the Second Assessment Report of the Intergovernmental Panel on Climate Change, Cambridge University Press, Cambridge, UK.

Kaspers, K. A., et al. (2004), Model calculations of the age of firn air across the Antarctic continent, Atmos. Chem. Phys., 4, 1365-1380.

Kato, S., Akimoto, H., Röckmann, T., Bräunlich, M., Brenninkmeijer, C.A.M. (1999), Stable isotopic compositions of carbon monoxide from biomass burning experiments. Atmos. Environ. 1999, 33, 4357–4362.

Keeling, C. D. (1960), The Concentration and Isotopic Abundances of Carbon Dioxide in the Atmosphere, Tellus, XII(2), 200-203.

Khalil, M. A. K. (1993), Atmospheric Methane: Sources, Sinks, and Role in Global Change, Springer-Verlag, Berlin.

Khalil, M. A. K., and R. A. Rasmussen (1984), Carbon monoxide in the earth's atmosphere: increased trend, Science, 224(4644), 54-56.

Khalil, M. A. K., and R. A. Rasmussen (1990), Atmospheric carbon monoxide: latitudinal distribution of sources, Geophysical Research Letters, 17(11), 1913-1916.

Khalil, M. A. K., and R. A. Rasmussen (1994), Global decrease in atmospheric carbon monoxide concentration, Nature, 370(6491), 639-641.

Kitzberger, T., Brown, P. M., Heyerdahl, E. K., Swetnam, T. W., Veblen, T. T., (2007), Contingent Pacific-Atlantic influence on multicentury wildfire synchrony over western North America, Proc. Nat. Acad. Sci., 104, 543-548.

Kitzberger,T., Swetnam, T. W., Veblen, T. T., (2001), Inter-hemispheric synchrony of forest fires and the El Niño-Southern Oscillation, Glob. Ecol. Bio., 10, 315-326.

Kremer, M. (1993), Population growth and technological change: one million BC to 1990. The Quarterly Journal of Economics, Vol 108, Number 3, 681-716.

Lamarque, J.-F., Emmons, L. K., Hess, P. G., Kinnison, D. E., Tilmes, S., Vitt, F., Heald, C. L., Holland, E. A., Lauritzen, P. H., Neu, J., Orlando, J. J. (2010), Rasch, P. J., and Tyndall, G.K.: CAM-chem: description and evaluation of interactive atmospheric chemistry in the Community Earth System Model, Geosci. Model Dev., 5, 369–411, doi:10.5194/gmd-5-369-2012.

Lelieveld, J., Brenninkmeijer, C. A. M., Joeckel, P., Isaksen, I. S. A., Krol, M. C., Mak, J. E., Dlugokencky, E., Montzka, S. A., Novelli, P. C., Peters, W., and Tans, P. P., (2006), New Directions: Watching over tropospheric hydroxyl (OH), Atmospheric Environment, 40(29), 5741-5743.

Levine, J. G., Wolff, E. W., Jones, A. E., Sime, L. C., Valdes, P. J., Archibald, A. T., Carver, G. D., Warwick, N. J., and Pyle, J. A., (2011), Reconciling the changes in atmospheric methane sources and sinks between the Last Glacial Maximum and the pre-industrial era, Geophys. Res. Lett., 38.

Lobert, J. M., D. H. Scharffe, W.-H. Hao, T. A. Kuhlbush, R. Seuwen, P. Warneck, and P. J. Crutzen (1992), Experimental evaluation of biomass burning emissions Nitrogen and carbon containing compounds in Global Biomass Burning Atmospheric Climatic and Biospheric Implications, edited by J. S. Levine, pp. 289-304, MIT Press, Cambridge, Mass.

Logan, J. A., M. J. Prather, S. C. Wofsy, and M. B. McElroy (1981), Tropospheric chemistry: A global perspective, J. Geophys. Res., 86, 7210– 7254.

Loulergue, L., A. Schilt, R. Spahni, V. Masson-Delmotte, T. Blunier, B. Lemieux, J. M. Barnola, D. Raynaud, T. F. Stocker, and J. Chappellaz (2008), Orbital and millennial-scale features of atmospheric CH4 over the past 800,000 years, Nature, 453(7193), 383-386.

Lowe, D. C., C. A. M. Brenninkmeijer, S. C. Tyler, and E. J. Dlugkencky (1991), Determination of the Isotopic Composition of Atmospheric Methane and Its Application in the Antarctic, Journal of Geophysical Research-Atmospheres, 96(D8), 15455-15467.

Lowe, D. C., M. R. Manning, G. W. Brailsford, and A. M. Bromley (1997), The 1991-1992 atmospheric methane anomaly: Southern Hemisphere 13C decrease and growth rate fluctuations, Geophysical Research Letters, 24(8), 857-860.

Luthi, D., et al. (2008), High-resolution carbon dioxide concentration record 650,000-800,000 years before present, Nature, 453(7193), 379-382.

MacFarling Meure, C. (2004), The Variation of Atmospheric Carbon Dioxide, Methane and Nitrous Oxide During the Holocene from Ice Core Analysis, Ph.D. thesis, The University of Melbourne.

Mak, J. E., and C. A. M. Brenninkmeijer (1994), Compressed-Air Sample Technology for Isotopic Analysis of Atmospheric Carbon-Monoxide, Journal of Atmospheric and Oceanic Technology, 11(2), 425-431.

Mak, J. E., and Brenninkmeijer, C. A. M., (1998), Measurement of ^{13}CO and $C^{18}O$ in the Free Troposphere, J. Geophys. Res., 103, D15, 19347-19358.

Mak, J. E. and Kra, G., (1999), The isotopic composition of carbon monoxide at Montauk Point, Long Island, Chemosphere-Global Change Science, 1, 205-218.

Mak, J. E., and Yang, W. B., (1998), Technique for analysis of air samples for ^{13}C and ^{18}O in carbon monoxide via continuous-flow isotope ratio mass spectrometry, Anal. Chem., 70(24),5159-5161.

Mak, J. E., M. R. Manning, and D. C. Lowe (2000), Aircraft observations of δ13C of atmospheric methane over the Pacific in August 1991 and 1993: Evidence of an enrichment in 13CH4 in the Southern Hemisphere, Journal of Geophysical Research-Atmospheres, 105(D1), 1329-1335.

Manning, M. R., C. A. M. Brenninkmeijer, and W. Allan (1997), Atmospheric carbon monoxide budget of the southern hemisphere: Implications of 13C/12C measurements, Journal of Geophysical Research-Atmospheres, 102(D9), 10673-10682.

Marcott, S.A., Bauska, T.K., Buizert, C., Steig, E.J., Rosen, J.L., Cuffey, K.M., Fudge, T.J., Severinghaus, J.P., Ahn, J., Kalk, M., McConnell, J.R., Sowers, T., Taylor, K.C., White, J.W.C. and Brook, E.J. (2014), Centennial-scale changes in the global carbon cycle during the last deglaciation Nature, 514, 616 - 619, doi: 10.1038/nature13799.

Marlon, J. R., et al., (2013), Global Biomass burning: A synthesis and review of Holocene paleo fire records and their controls, Quat. Sci. Rev., 65, 5-25.

Marlon, J. R., Bartlein, P., Carcaillet, C., Gavin, D., Harrison, S., Higuera, P., Joos, F., Power, M., Prentice, C., (2008), Climate and Human Influences on global biomass burning over the past two millenia, Nature Geo., 1, 697-701.

McGlone, M. S., Kershaw, A. P., Markgraf, V., (1992), El Nino/Southern oscillation climatic variability in Australasian and south American paleoenvironmental records. In: Diaz, H.F., Markgraf, V. (Eds.), El Nino: Historical and Paleoclimatic Aspects of the Southern Oscillation. Cambridge University Press, Cambridge, pp. 435.

Mischler, J. A. et al. (2009), Carbon and hydrogen isotopic composition of methane over the last 1000 years. Glob. Biogeochem. Cycles 23.

Mitchell, L., Brook, E., Lee, J. E., Buizert, C., Sowers, T. (2013), Constraints on the Late Holocene Anthropogenic Contribution to the Atmospheric Methane Budget, Science, 342, 964-967.

Mitchell, L. E., Brook, E. J., Sowers, T., McConnell, J. R., and Taylor, K., (2011), Methane Concentration and Chronology from the WAIS Divide Ice Core (WDC05A). Boulder, Colorado USA: National Snow and Ice Data Center. http://dx.doi.org/10.7265/N5319SV3.

Mitchell, L. E., Brook, E. J., Sowers, T., McConnell, J. R., and Taylor K., (2011), Multidecadal variability of atmospheric methane, 1000-1800 C.E., J. Geophys. Res.,116.

Monnin, E., Indermuhle, A., Dallenbach, J., Fluckiger, J., Stauffer, T. F., Raynaud, D., and Barnola, J. M., (2001) Atmospheric CO_2 Concentrations over the Last Glacial Termination Science 291 (5501), 112-114.

Montzka, S. M., Krol, M., Dlugokencky, E., Hall, B., Jockel, P., Lelieveld, J., (2011), Small Interannual Variability of Global Atmospheric Hydroxyl, Science, 331, 67-69.

Montzka, S. A., P. Calvert, B. D. Hall, J. W. Elkins, T. J. Conway, P. P. Tans, and C. Sweeney (2007), On the global distribution, seasonality, and
budget of atmospheric carbonyl sulfide (COS) and some similarities to CO2, J. Geophys. Res., 112, D09302, doi:10.1029/2006JD007665.

Nakagawa, F., Tsunogai, U., Gamo, T. and Yoshida, N. (2004), Stable isotopic compositions and fractionations of carbon monoxide at coastal and open ocean stations in the Pacific. J. Geophys. Res. Oceans, 109, doi:10.1029/2001JC001108.

NGRIP Project members (2004), High-resolution record of Northern Hemisphere climate extending into the last interglacial period. Nature 431:147–151

Novelli, P.C., et al., (1998), An internally consistent set of globally distributed Atmospheric carbon monoxide mixing ratios developed using results from an inter comparison of measurements. Geophys. Res., 103, 19,285-19,293.

Novelli, P.C., Masarie, K.A. and Lang, P.M. (1998), Distribution and recent Trends of carbon monoxide in the lower troposphere, Geo phys Res., 103, 19,015-19,033.

Novelli, P.C., Masarie, K.A., Tans, P.P. and Lang, P.M. (1994), Recent changes in atmospheric carbon monoxide, Science 2, 63, 1587-1590, 1994.

Park, K., Emmons, L.K., Wang, Z., Mak, J.E. (2013), Large interannual variations in nonmethane volatile organic compound emissions based on measurements of carbon monoxide. Geophys. Res. Lett., 40, 221–226.

Park, K., Emmons, L.K., Wang, Z and Mak, J. E. (2015), Joint Application of Concentration and $\delta^{18}O$ to Investigate theGlobal Atmospheric CO Budget, Atmosphere, 6, 547-578; doi:10.3390/atmos6050547.

Park, K., Wang, Z., Emmons, L.K., Mak, J.M. (2015), Variation of atmospheric CO, $\delta^{13}C$ and $\delta^{18}O$ at high northern latitude during 2004-2009: observations and model simulations, J. Geophys.Res. 120, 11,024–11,036, doi:10.1002/2015JD023191

Petrenko, V. V., Martinerie, P., Novelli, P., Etheridge, D. M., Levin, I., Wang, Z., Blunier, T., Chappellaz, J., Kaiser, J., Lang, P., Steele, L. P., Hammer, S., Mak, J., Langenfelds, R. L., Schwander, J., Severinghaus, J. P., Witrant, E., Petron, G., Battle, M. O., Forster, G., Sturges, W. T., Lamarque, J.-F., Steffen, K., and White, J. W. C. (2013), A 60 yr record of atmospheric carbon monoxide reconstructed from Greenland firn air, Atmos. Chem. Phys., 13, 7567–7585, doi:10.5194/acp-13-7567-2013.

Power, M. J., Marlon, J., Ortiz, N. (2008), Changes in fire regime since the Last Glacial Maximum: An assessment based on a global synthesis and analysis of charcoal data, Climate Dynamics, 30, 887-907.

Power, M. J., et al., (2012), Climatic control of the biomass burning decline in the Americas after AD 1500, Holocene, 23.

Quay, P.D., King, S.L., Stutsman, J., Wilbur, D.O., Steele, L.P., Fung, I.; Gammon, R.H., Brown, T.A., Farwell, G.W., Grootes, P.M., Schmidt, F.H. (1991), Carbon isotopic composition of atmospheric CH4: Fossil and biomass burning source strengths. Glob. Biogeochem. Cycles, 5, 25–47.

Raynaud, D., et al., (1993) The Ice Record of Greenhouse Gases, Science, 259, 926-934.

Reeburgh, W. S. (2004), Global methane biogeochemistry, Treat. Geochem., 4, 65– 89.

Rinsland, C. P., and J. S. Levine (1985), Free tropspheric carbon monoxide concentrations in 1950 and 1951 deduced from infrared total column amount measurements, Nature, 318(6043), 250-254.

Röckmann, T., and Brenninkmeijer, C.A.M., (1997), CO and CO2 isotopic composition in Spitsbergen during the 1995 ARCTOC campaign, Tellus Series B-Chemical and Physical Meteorology, 49(5), 455-465.

Röckmann, T. and Brenninkmeijer, C. A. M., (1998), The error in conventionally reported ^{13}C ^{12}C ratio of atmospheric CO due to the presence of mass independent oxygen isotope enrichment, Geophys. Res. Lett., 25, 3163–3166.

Röckmann, T., Brenninkmeijer, C.A.M., Saueressig, G., Bergamaschi, P., Crowley, J.N., Fischer, H., Crutzen, P.J. (1998), Mass-independent oxygen isotope fractionation in atmospheric CO as a result of the reaction CO + OH. Science, 281, 544–546.

Röckmann, T., Kaiser, J., and C. A. M. Brenninkmeijer (2003), The isotopic fingerprint of the pre-industrial and the anthropogenic N2O source, Atmospheric Chemistry and Physics, 3, 315-323.

Röckmann, T., Kaiser, J., C. A. M. Brenninkmeijer, and W. A. Brand (2003), Gas chromatography/isotope-ratio mass spectrometry method for high-precision position-dependent 15N and 18O measurements of atmospheric nitrous oxide, Rapid Communications in Mass Spectrometry, 17(16), 1897-1908.

Röckmann, T., Jockel, P., Gros, V., Braunlich, M., Possnert, G and Brenninkmeijer, C.A.M., (2002), Using ^{14}C, ^{13}C, ^{18}O and ^{17}O isotopic variations to provide insights into the high northern latitude surface CO inventory, Atmospheric Chemistry and Physics, 2, 147-159.

Ruddiman, W., et al., (2008), Early rice farming and methane emissions, Quat. Sci. Rev. 27, 1291-1295.

Ruddiman, W., (2003), The Anthropogenic Greenhouse Era began thousands of Years Ago, Climatic Change, 61, 261-293.

Rudolph, J., R. S. Anderson, K. V. Czapiewski, E. Czuba, D. Ernst, T. Gillespie, L. Huang, C. Rigby, and A. E. Thompson (2003), The stable carbon isotope ratio of biogenicemissions of isoprene and the potential use of stable isotope ratio measurements to study photochemical processing of isoprene in the atmosphere, Journal of Atmospheric Chemistry, 44(1), 39-55.

Sanhueza, E., Y. Dong, D. Scharffe, J. M. Lobert, and P. J. Crutzen (1998), Carbon monoxide uptake by temperate forest soils: the effects of leaves and humus layers, Tellus Series B-Chemical and Physical Meteorology, 50(1), 51-58.

Saueressig, G., J. N. Crowley, P. Bergamaschi, C. Bruhl, C. A. M. Brenninkmeijer, and H. Fischer (2001), 13C and D kinetic isotope effects in the reactions of CH4 with O(1D) and OH: New laboratory measurements and their implications for the isotopic composition of stratospheric methane, Journal of Geophysical Research-Atmospheres, 106(D19), 23127-23138.

Schaefer, H., and M. J. Whiticar (2008), Potential glacial-interglacial changes in stable carbon isotope ratios of methane sources and sink fractionation, Global Biogeochemical Cycles, 22(1).

Schwander, J., Barnola, J., Andrie, C., Leuenberger, M., Ludin, A., Raynaud, D., and Stauffer, B. (1993) The age of the air in the firn and the ice at Summit, Greenland, J. Geophys. Res., 98D, 2831–2838.

Schütze, M. (1949), Ein neues Oxidationsmittel für die quantitative Überführung von Kohlenmonoxyd in Kohlendioxyd, Ein Beitrag zur Chemie des Jodpentoxids, Ber. Dtsch. Chem. Ges, 77b, 484–487.

Seiler, W. and Crutzen, P. J., (1980), Estimates of gross and net fluxes of carbon between the biosphere and atmosphere from biomass burning, Clim. Change, 2, 207–247.

Severinghaus J.P., Brook E.J. (1999), Abrupt climate change at the end of the last glacial period inferred from trapped air in polar ice. Science 286:930–934.

Siegenthaler, U., E. Monnin, K. Kawamura, R. Spahni, J. Schwander, B. Stauffer, T. F. 184 Stocker, J. M. Barnola, and H. Fischer (2005), Supporting evidence from the EPICA Dronning Maud Land ice core for atmospheric CO_2 changes during the past millennium, Tellus Series B-Chemical and Physical Meteorology, 57(1), 51-57.

Singarayer, J. S., Valdes, P. J., Friedlingstein, P, Nelson, S., and Beerling, D. J., (2011), Late Holocene methane rise caused by orbitally controlled increase in tropical sources. Nature, 470, 82-86.

Sigl, M., Winstrup, M., McConnell, J.R., Welten, K.C., Plunkett, G., Ludlow, F., Buntgen, U., Caffee, M., Chellman, N., Dahl-Jensen, D., Fischer, H., Kipfstuhl, S., Kostick, C., Maselli, O.J., Mekhaldi, F., Mulvaney, R., Muscheler, R., Pasteris, D.R., Pilcher, J.R., Salzer, M., Schupbach, S., Steffensen, J.P., Vinther, B.M. and Woodruff, T.E. (2015), Timing and climate forcing of volcanic eruptions for the past 2,500 years Nature, p. 543 - 549doi: 10.1038/nature14565

Smiley, W. G. (1965), Note on a reagent for oxidation of carbon monoxide, Nucl. Sci. Abstr, 3, 391.

Sowers, T., (2010), Atmospheric methane isotope records covering the Holocene period, Quat. Sci. Rev., 29, 213-221.

Sowers, T., et al., (1992), The $\delta^{15}N$ of N_2 in air trapped in polar ice: a tracer of gas transport in the firn and a possible constraint on ice age-gas age differences, J. Geophys Res, 97, 15683-15697.

Spahni, R., Chappellaz, J., Stocker, T. F., Loulergue, L., Hausammann, G., Kawamura, K., Fluckiger, J., Schwander, J., Raynaud, D., Masson-Delmotte, V., Jouzel, (2005)J., Atmospheric Methane and Nitrous Oxide of the Late Pleistocene from Antarctic Ice Cores, Science, 310, 1317-1320.

Stevens, C. M. (1993), New isotopic perspectives on atmospheric CO sources, Eos Transactions, AGU, 74(43), Fall meeting suppliment F179.

Stevens C.M., and Engelkemeir A., (1988), J. Geophys. Res. 93, 725.

Stevens, C. and Krout, L. (1972), Method for the determination of the concentration and of the carbon and oxygen isotopic composition of atmosspheric carbon monoxide, Int. J. Mass Spectrom. Ion Phys., 60453, 265–275.

Stevens, C.M. and Wagner, A.F. (1989), The role of isotope fractionation effects in atmospheric chemistry.Z. Naturforschung, 44, 376–384.

Stevens, C.M., Walling, D., Venters, A., Ross, L.E., Engelkem, A, Krout, L. (1972), Isotopic composition of atmospheric carbon-monoxide. Earth Planet. Sci. Lett. 16, 147–165.

Stubbins, A.; Uher, G.; Kitidis, V.; Law, C.S.; Upstill-Goddard, R.C.; Woodward, E.M.S. (2006), The open-ocean source of atmospheric carbon monoxide. Deep Sea Res. Part II Top. Stud. Oceanogr, 53, 1685–1694.

Swetnam, T. W., (1993), Fire history and climate change in giant sequoia groves, Science, 262, 885–889.

Takai, Y., (1970), The mechanism of methane fermentation in flooded paddy soil. Soil Sci Plant Nutr, 16, 238-244.

Tarr, M.A., Miller, W.L., Zepp, R.G. (1995), Direct carbon monoxide photoproduction from plant matter. J. Geophys. Res., 100, 11403–11413.

Trudinger, C. M., Enting, I.G., Etheridge, D.M., Francey, R.J., Levchenko, V.A., Steele, L.P., Raynaud, D. and Arnaud, L. (2004), Modeling air movement and bubble trapping in firn, Journal of Geophysical Research-Atmospheres, 102(D6), 6747-6763.

Trudinger, C., Etheridge, D., Rayner, P., Enting, I., Sturrock, G., and Langenfelds, R. (2002), Reconstructing atmospheric histories from measurements of air composition in firn, J. Geophys. Res., 107, 4780, doi:10.1029/2002JD002545.

Tsunogai, U., Nakagawa, F., Komatsu, D.D., Gamo, T. (2002), Stable carbon and oxygen isotopic analysis of atmospheric carbon monoxide using continuous-flow isotope ratio ms by isotope ratio monitoring of CO. Anal. Chem., 74, 5695–5700.

Urey, H. C. (1947), The thermodynamic properties of isotopic substances. Journal of the Chemical Society, 562–581.

van der Werf, G. R., Peters, W, van Leeuwen, T. T., Giglio, L., (2013), What could have caused pre-industrial biomass burning emissions to exceed current rates? Climate of The Past, 9.

van der Werf, G. R., Randerson, J. T., Giglio, L., Collatz, G. J., Mu, M., Kasibhatla, P. S., Morton, D. C., DeFries, R. S., Jin, Y., and van Leeuwen, T. T., (2010), Global fire emissions and the contribution of deforestation, savanna, forest, agricultural, and peat fires (1997-2009), Atmos Chem Phys, 10, 11707-11735.

Wang, Z., Chappellaz, J., Martinerie, Park, K., Petrenko, V., Mak, J. E. (2012), The isotopic record of Northern Hemisphere atmospheric carbon monoxide since 1950, implications for the CO budget. Atmospheric Chemistry and Physics, European Geosciences Union (EGU),12, pp.4365-4377.

Wang, Z., Chappellaz, J., Park, K.H., and Mak J.E. (2010), Large Variations in Southern Hemisphere Biomass Burning during the last 650 years, Science, 30, 1663-1666.

Wang, Z. and Mak, J.E. (2010), A new CF-IRMS system for the quantification of the stable isotopes of carbon monoxide from ice cores and small air samples, Atmos. Meas. Tech., 3, 1307-1317.

Westerling, A. L., Hidalgo, H. G., Cayan, D. R., Swetnam, T. W. (2006), Warming and earlier spring increase western US forest wildfire activity, Science, 313, 940-943.

Witrant, E., Martinerie, P., Hogan, C., Laube, J. C., Kawamura, K., Capron, E. and Montzka, S. A., (2012), A new multi-gas constrained model of trace gas non-homogeneous transport in firn: evaluation and behaviour at eleven polar sites, Atmospheric Chemistry and Physics, 12, 11465–11483.

Zimmerman, P, Chatfield, R.B., Fishman, J., Crutzen, P.J. and Hanst, P.L. (1978), Estimates of CO and H2 from the oxidation of hydrocarbon emissions from vegetation. Geophys. Res. Letter, 5, 679-682.

Appendix - WAIS Divide Ice Core Measurements

Depth (m)	Gas Age* (AD)	[CO] ppbv[+]	$\delta^{13}C$ (‰, VPDB)[++]	$\delta^{18}O$ (‰, VSMOW)[§]	Process Date
71	1974	105.2	-34.83	3.85	7/30/15
72	1969	100.0	-32.23	5.27	7/28/15
73	1960	99.1	-32.00	5.80	7/20/15
74	1958	78.3	-30.32	4.07	6/9/15
75	1954	107.4	-31.75	4.25	6/11/15
76	1949	64.2	-32.48	3.37	7/29/15
77	1945	61.9	-33.20	4.50	7/29/15
78	1940	67.3	-33.56	-0.60	2/11/16
79	1937	63.9	-36.05	0.33	2/26/16
80	1933	56.8	-32.11	2.03	7/28/15
81	1929	55.8	-32.90	1.40	8/5/15
82	1924	66.7	-34.33	-0.96	10/31/15
83	1920	52.7	-33.78	-4.44	11/1/15
84	1915	63.2	-30.87	4.04	7/23/15
85	1911	67.0	-32.11	3.24	3/17/16
86	1908	66.5	-32.71	1.89	7/16/15
88	1899	72.7	-31.34	6.37	3/8/16
89	1895	73.8	-34.04	6.44	3/10/16
91	1887	45.7	-32.73	3.69	3/25/16
92	1883	58.9	-32.28	-	8/24/15
93	1878	56.7	-31.17	5.84	4/1/16
94	1871	46.2	-33.39	5.16	3/19/16
95	1869	52.7	-33.53	-1.23	8/6/15
96	1865	59.5	-31.57	2.41	7/22/15
97	1860	50.4	-31.67	5.28	8/5/15
98	1856	59.5	-30.92	6.21	2/13/16
99	1851	47.9	-33.25	0.15	2/12/16
100	1847	54.4	-35.12	1.60	7/30/15
101	1842	51.7	-31.59	2.10	7/22/15
102	1839	48.6	-32.04	4.47	7/21/15
103	1833	55.9	-32.76	5.23	5/26/16

104	1828	52.9	-31.65	6.06	5/26/16
107	1816	64.6	-31.39	4.93	3/11/16
108	1811	48.5	-31.58	-0.02	7/23/15
112	1795	44.4	-31.35	5.00	6/2/16
115	1780	48.5	-31.17	5.43	5/28/16
116	1777	60.8	-30.69	6.92	6/1/16
119	1763	44.8	-32.15	2.85	6/2/16
120	1759	48.1	-30.48	3.62	6/1/16
122	1751	45.9	-30.10	6.72	5/28/16
126	1734	45.7	-29.74	4.33	6/3/16
130	1713	49.3	-29.04	7.26	6/3/16

* Uncertainty ± 10 years; $^{+}$ ± 5 ppbv; $^{++}$ ± .4 ‰; § ± .7 ‰.